A Search for Very High Energy Gamma-rays From Hercules X-1 Using the Pulse Profile Technique

A Thesis Submitted to the
Department of Physics
and
Mathematical Physics
University of Adelaide

for the degree of Doctor of Philosophy

by

Michael Damien Roberts B.Sc (Hons.)

December 1993

Contents

Summary

This thesis contains work done by the author on the Woomera air Čerenkov telescope, and background information relating to that work.

Chapter 1 provides an introduction to the field of gamma-ray astronomy. It includes an introduction to ground based gamma-ray astronomy and recent satellite observations. Gamma-ray production mechanisms and some environments where gamma-ray production could occur are discussed. The recent history of ground based gamma-ray observations is reviewed, including a source list and a brief description of two important sources. The last part of this chapter is a review of the source Hercules X-1, including ground based observations of Her X-1 at gamma-ray energies and proposed models for some of the features of the gamma-ray emission from this object.

Chapter 2 is a discussion of the formation of extensive air showers (EAS), with emphasis on the differences between gamma-ray and cosmic ray induced EAS.

In Chapter 3 the atmospheric Čerenkov technique is discussed. This chapter describes the nature of Čerenkov emission from EAS and how this affects the design of air Čerenkov telescopes. The two telescopes located at Woomera, BIGRAT and CANGAROO, are described in this chapter. The Sommers-Elbert technique for large zenith angle observation is described. This work includes Monte Carlo simulations performed by the author which show how the collecting area and threshold energy of BIGRAT vary with the zenith angle of observation.

Gamma-ray observations made with the atmospheric Čerenkov technique must contend with a large background signal due to EAS initiated by cosmic rays. Chapter 4 contains a discussion of techniques for enhancing the sensitivity of air Čerenkov telescopes by rejecting this cosmic ray background. Camera systems are discussed, including experimental details of a camera system recently installed on BIGRAT.

Chapters 5 and 6 contain most of the work done by the author for this thesis. Chapter 5 describes a method for rejecting the cosmic ray background by measuring the temporal distribution of Čerenkov photons from EAS. The formation of pulse

profiles is discussed, including detailed Monte Carlo simulations performed by the author. These simulations show that the pulse profile measurement technique can be used to differentiate between gamma-ray and cosmic ray induced EAS. Pulse profile parameters are described as well as a method for applying cuts on data to increase the gamma-ray sensitivity of observations. This chapter also contains a description of a pulse profile measurement system built by the author and installed on the BIGRAT telescope. At the end of this chapter is a short discussion about combining pulse profile cuts with camera image cuts to further increase the sensitivity of the atmospheric Čerenkov technique to gamma-rays.

The first section of Chapter 6 contains a discussion of time series analysis techniques used in the search for pulsed gamma-ray emission. The rest of Chapter 6 describes the search, performed by the author, for pulsed gamma-ray emission from the x-ray binary Hercules X-1. Observations of Her X-1 were made with the pulse profile measurement system on BIGRAT during 1992 and 1993. Analysis of these data has shown that gamma-ray emission was possibly detected from Her X-1 during 1992. A signal, pulsed at a period blue shifted from the x-ray period of Her X-1 by 0.05%, was seen in all three files taken around eclipse ingress. The flux above 27TeV in these files was calculated to be around 4×10^{-12} photons s^{-1} cm^{-2}, corresponding to a source luminosity of $\sim 10^{36}$ erg/s. When the chance probabilities for all three ingress files were combined the final significance was found to be 1.34×10^{-4}.

Chapter 7 contains a brief conclusion and suggestions for further work.

Statement of Originality

This work contains no material which has been accepted for the award of any other degree or diploma in any university or other tertiary institution and, to the best of my knowledge and belief, contains no material previously published or written by another person, except where due reference has been made in the text.

I give consent to this copy of my thesis, when deposited in the University Library, being available for loan and photocopying.

SIGNED: .. DATE: 21/12/93

Acknowledgments

A few words of thanks at the beginning of my thesis is poor payment for the help I have received during the past four years (although I dare say it will cost me a few beers as well).

Firstly I would like to thank my supervisor Dr. John Patterson. I would also like to thank the other senior members of the Woomera group, Dr. Greg Thornton and Dr. Phil Edwards, for their help over the years and for the proof reading of this document. Dr. Roger Clay is also thanked for his help in preparing this thesis. I am especially indebted to Neville Wild, the technician for the High Energy Astrophysics group. Without his patient assistance this project could never have been realized. I am also grateful to the other members of the group who have all helped me at one time or another. I acknowledge the assistance of Mark Ferraretto, the departmental computing officer, and other members of the general staff.

During my time in the Physics Department I have shared many good times, plenty of drinks and a lot of laughs with many students and staff. Particularly I would like to thank Rishi, Petar, Gary, Gavin, Paul, Bruce, Janice, Terry, Syd, Anthony S, Anthony L, Chris, Andrew and Paddy.

Finally I would like to thank Gail, who endured my many trips to Woomera cheerfully (mostly), and provided friendship and support during my studies.

Chapter 1

Introduction to Gamma-ray Astronomy

1.1 Introduction

In 1912 experiments conducted by Victor Hess (Hess 1912) led to the realization that the earth is being bombarded by high energy radiation. These "cosmic rays" were found to consist mainly of energetic charged particles whose energies extended beyond 10^{20} eV, well above energies attainable by today's man made particle accelerators. As the charged cosmic rays traverse the magnetic fields of interstellar space, they are scattered away from their original trajectory. If a cosmic ray travels a sufficient distance all information about its original direction is thus lost. As a result, measurements of cosmic rays at earth show almost isotropic arrival distributions at most energies and, consequently, sources of cosmic rays cannot be identified by measurement of arrival directions at earth.

Any discreet source capable of accelerating cosmic rays to the enormous energies seen could also be a source of other energetic radiation, such as gamma-rays and neutrinos. Both of these types of particles, being electrically neutral, would travel undeflected from their source. While neutrinos are produced in large numbers in high energy interactions, and travel easily from production region to observer, they are difficult to detect. Gamma-rays on the other hand, are easily detected, and still travel relatively unimpeded through space. Gamma-rays can be defined as photons with energy greater than 0.51MeV (the rest mass of the electron). Gamma-ray astronomy is divided into broad energy domains, determined by the detection technique used to observe them.

Gamma-rays entering the earth's atmosphere will interact via pair production. From the top of the atmosphere to sea level is more than 30 interaction lengths for pair production. Direct observation of gamma-rays must be made above the bulk of the atmosphere, with either balloon or satellite experiments. These experiments operate in the range $\sim$ 30MeV to several tens of GeV, and this region is known as the high energy (HE) region. Satellite and balloon experiments usually rely on a spark chamber as the central detector. They have excellent signal to noise, good angular resolution and a wide field of view. The collecting area of these detectors is limited by the size and weight that can be launched by rocket or carried by balloon. Typically an experiment of this type will have a collecting area of around 1000 square centimeters.

Above the HE region the low flux of gamma-rays necessitates the use of techniques with larger collecting areas than are available with direct detection methods. An energetic gamma-ray entering the earth's atmosphere will produce a cascade of secondary particles known as an extensive air shower (EAS). If the secondary particles are sufficiently energetic then they will cause the emission of Čerenkov radiation. The development of EAS and subsequent Čerenkov emission is described in detail in chapters 2 and 3. An EAS initiated by a primary with energy greater than $\sim$ 100GeV will produce enough Čerenkov radiation to be detected at ground level. The atmospheric Čerenkov technique is generally used to detect primary gamma-rays in the energy range 100GeV to 100TeV, and this range is known as the very high energy (VHE) region. The atmospheric Čerenkov technique has the advantage of very large collecting areas ($\sim 10^5\mathrm{m}^2$). Disadvantages of the atmospheric Čerenkov technique include lack of control over the detection medium (the atmosphere) and difficulty in interpreting results because of the complexity of the development of EAS. The duty cycle of VHE observations is also small ($\sim$ 10%) because the low numbers of Čerenkov photons limits observations to cloudless, moonless nights. Air Čerenkov experiments can have good angular resolution but generally only have a small field of view.

Above a primary particle energy of around 100TeV the secondary particles of the EAS arrive in detectable numbers at ground level. These ultra high energy (UHE) gamma-rays can be detected by arrays of particle detectors. Particle arrays have the advantage of wide field of view and they can be designed to give excellent angular resolution. Unlike air Čerenkov telescopes, arrays can be run continuously, although the analysis of data is still complicated by the development of the EAS that they detect.

The remainder of this chapter will discuss the production of VHE and UHE gamma-rays, and the development of ground based gamma-ray astronomy.

1.2 Brief History of Ground Based Gamma-ray Astronomy

For reasons of brevity a complete review of the field is not possible here. Instead, this section will contain a list of sources reported to be emitters of VHE and UHE gamma-rays, and a brief summary of observations on a few important sources. For more detailed reviews the reader is referred to articles by Weekes (1988,1992), Protheroe (1993) and Nagle et al. (1988).

During the 1960's and 1970's a number of groups searched for point sources of VHE and UHE gamma-rays. Observations were made with air Čerenkov telescopes and array experiments covering an energy range from 0.2 TeV to 100PeV. The majority of the early observations resulted in upper limits only, and those sources that were seen (Crab, Cygnus X-3, Cen A) showed no consistency in observed flux levels.

The launch of gamma-ray satellite experiments during the 1970's caused renewed interest in TeV and PeV gamma-ray astronomy. From this time on, dozens of new experiments were built and the number of reported sources has increased from a few to more than twenty. Table 1.1 shows a list of reported gamma-ray

Source	Period	Distance (kpc)	Discovered by
Radio Pulsars			
1937 +21	1.6ms	5	Durham
1957 +20	1.6ms	1.0	Durham
1855 +09	5.4ms	0.35	Durham
1953 +29	6.1ms	0.8	Durham
0531 +21	33ms	2.0	SAO
0833 -45	89ms	0.5	Tata
0355 +54	156ms	?	Tata
1706 -44	102ms	?	CANGAROO (1)
X-ray Binaries			
Cyg X-3	(4.8h/12.6ms)	>10	Crimea
Her X-1	(1.7d/1.24s)	5.8	Durham
Cas Gam-1	3.61s	5	Crimea
Vela X-1	(8.96d/283s)	1.9	Potchefstroom
Cen X-3	(2.09d/4.823s)	10	Durham
1E2259 +58	3.49s	3.6	Durham
Sco X-1	0.797d	1	Potchefstroom
LMC X-4	(1.41d/13.49s)	50	Durham
SMC X-1	710.5ms	?	Durham
AE-Aqr	(9.88h/33s)	0.053	Potchefstroom (2)
AGN			
Cen A	-	4400	SAO
Mrk 421	-	z=0.031	Whipple (3)

Table 1.1: List of reported VHE and UHE gamma-ray sources. Where both the orbital period and pulsar period are listed the format (orbital/pulsar) is used. The data are from Weekes 1992 with more recently claimed sources that are numbered. The references for these are (1) Ogio et al. (1993) (2) Brink et al. 1990 (3) Punch et al. (1992). It should be noted that for some radio pulsars, such as the Crab (0531 +21), the gamma-ray emission is actually thought to come from the nebula rather than the pulsar itself.

sources. The information is from Weekes (1992), modified by the inclusion of some more recent data.

One of the great difficulties in ground based gamma-ray astronomy is to assess the significance of an observation. Many reported detections have relied on signals with only small significance, and some researchers have expressed concerns about how the significance of results are determined. While some of the sources listed in table 1.1 may be dubious, there is strong evidence for the ground based detection of at least a few sources (Crab, Her X-1 and Cyg X-3). A brief discussion of observations of the Crab and Cyg X-3 will follow. Her X-1 is discussed in more detail at the end of this chapter.

Crab Pulsar (Psr 0531 +21)/Crab nebula

The Crab pulsar was created as the result of a supernova explosion approximately 940 years ago. The pulsar has a period of 33ms and is still within its supernova remnant (Crab nebula). The Crab has been studied intensely from radio to gamma-ray wavelengths. It has been detected as a source of 100MeV gamma-rays by balloon experiments and is seen as a strong source by satellite experiments. The Crab is an ideal target for VHE observation because it is believed that radiation from the radio to x-ray is powered by synchrotron emission from electrons with energies up to several TeV.

The Crab pulsar has been observed extensively by air Čerenkov experiments since the 1960's. Reported detections show a pattern typical of claimed VHE and UHE sources. Most of the claimed detections were of low significance, with lack of consistency between detections in the type and strength of emission. There were reports of DC emission, pulsed emission and bursts on $\sim$ 15 minute timescales (see Weekes 1988 for details). The pulsed emission showed variability not only in the flux but also in the nature of the light curve.

The installation of a camera system on the Whipple 10m telescope (see section 4.2.2) has provided conclusive proof that the Crab is a source of VHE gamma-rays. This camera, and later cameras, provided unparalleled sensitivity for gamma-ray observations by providing a method of identifying gamma-ray initiated EAS against the background of cosmic ray events. The Whipple observations have shown that the Crab is a steady DC source of VHE gamma-rays. These observations of the Crab are significant at a level above 30σ, and show a flux above 0.4TeV of 7×10^{-11} photons $\mathrm{cm}^{-2}\mathrm{s}^{-1}$ (Reynolds et al. 1993). The Whipple data show no evidence of pulsed emission or bursting on a timescale of around half an hour. This is disturbing given the nature of the earlier reports of emission from the Crab, which were made with experiments of lesser sensitivity.

Cygnus X-3

Cygnus X-3 is an x-ray binary with an orbital period of 4.8 hours. It shows high variability at all frequencies at which it is observed. During radio bursts the radio flux can vary by a factor of 10^3 over its quiescent value.

Numerous ground based gamma-ray detections of Cyg X-3 have been claimed for energies from 0.3TeV to 10PeV. As with the early reported emission from the Crab, claimed detections of Cyg X-3 are often of low significance and show inconsistency in the flux and the shape of the 4.8 hour light curve (see Weekes 1988,1992). The Durham and Adelaide groups have also reported 12.59ms pulsations from Cyg X-3 (Chadwick et al. 1985, Gregory et al. 1990). Pulsations have also been reported at 9.22ms (Zyskin et al. 1987). Other experiments running during the same period have failed to confirm pulsations at these periods. Cygnus X-3 has provided further mystery with the detection of EAS, apparently from Cygnus X-3, with a muon content much higher than that expected from gamma-ray EAS (Samorski and Stamm 1983, Marshak 1985a,b and Battistoni et al. 1985).

Since 1985 there have been fewer reports of emission from Cyg X-3. The consensus seems to be that if Cyg X-3 was a source of VHE and UHE gamma-rays, it has decreased in intensity in recent times.

While high energy astrophysical phenomena are often highly time variable, the inconsistent nature of many reported VHE and UHE detections has cast doubt on many of the claimed sources. These doubts have been amplified by the failure of new, more sensitive experiments to detect previously reported sources.

At TeV energies, the new Whipple high resolution camera is an order of magnitude more sensitive than previous air Čerenkov detectors. In a recent paper (Reynolds et al. 1993), the Whipple group have reported on the search for DC emission from a total of 27 sources. Except for the Crab, it was found that none of the observations provided statistically significant evidence for DC emission of VHE gamma-rays. From more recent observations, the Whipple group have claimed evidence for steady emission from the BL-Lacertae object Markarian 421 at a significance of 6σ (Punch et al. 1992).

At UHE energies the CASA-MIA and CYGNUS arrays have also shown disappointing results. Recent source searches (Alexandreas et al. 1993, Cronin et al. 1992) show no evidence for emission from a large number of possible UHE gamma-ray sources. These included many sources claimed previously with less sensitive experiments. The results of the more recent experiments would seem to indicate that sources of VHE and UHE gamma-rays are fewer in number and less intense than previous observations would have predicted.

1.3 Satellite Experiments

The shielding of the earth's atmosphere means that direct observation of gamma-rays is only possible through high altitude balloon or satellite experiments. Since the early 1970's gamma-ray telescopes aboard satellites have yielded a wealth of information about cosmic gamma-rays in the MeV to tens of GeV energy range. This information is important to air Čerenkov experiments because it provides information about sources at energies just below those attainable through the study of EAS.

SAS-2

The second NASA Small Astronomical Satellite (SAS-2) was launched on 15 November, 1972. The principal detector consisted of a 32 level spark chamber with an active area of approximately 640cm^2. The energy threshold of the telescope was 30MeV, with energy determination possible for gamma-rays of energy less than 200MeV. The field of view of the telescope was 35° with angular resolution for individual gamma-rays of typically a few degrees. Absolute arrival times were determined to a precision of 1ms. For further experimental details see Fichtel et al. (1975) and references therein.

The observations of SAS-2 were terminated after only seven months because of a system failure. During this time 60% of the celestial sky was observed. The spectrum of the diffuse gamma-ray background was found to be represented by a power law of the form

$$\frac{dN}{dE} = \mathrm{AE}^{-\alpha} \tag{1.1}$$

where α was found to be 2.4 ± 0.2 over the range 35 to 200 MeV. The integral flux above 100MeV was found to be $1.93 \pm 0.26 \times 10^{-5}$ photons $\mathrm{cm}^{-2}\ \mathrm{s}^{-1}\ \mathrm{sr}^{-1}$.

Dominating the diffuse gamma-ray emission was the gamma-ray emission from the galactic plane. The galactic component was found to have a flatter spectrum than the diffuse background with

$$\frac{dN}{dE} = \mathrm{AE}^{-2.0} \tag{1.2}$$

The correlation between gamma-ray emission and structural features in the galaxy led to the conclusion that the galactic emission was probably due to the interaction of cosmic rays with the interstellar matter of the galaxy.

The SAS-2 data base was also searched for discrete sources of gamma-ray emission. Kniffen et al. (1977) found four such sources, the Crab and Vela pulsars, Cygnus X-3 and Geminga (γ195+5). Thompson et al. (1983) also searched for emission from known radio pulsars. The search involved a total of 43 pulsars, none of which yielded positive results.

COS B

The COS B satellite was launched in August 1975, and remained operational for almost seven years. The main instrument was a wire grid spark chamber with a sensitive area of $576\mathrm{cm}^2$. The energy threshold of COS B was 30MeV, with energy resolution available up to about 2GeV. The telescope could detect gamma-rays up to 30° off-axis with an angular resolution that varied from 10° at 30MeV to 2° at 1GeV. Arrival times were measured to less than 1ms.

The COS B data base covering the period August 1975 to December 1978 has

Source Name	No. of Observations	Position		Error Radius (degrees)	Flux[a] $E>100$ MeV (10^{-6} photons cm^{-2} s^{-1})	Spectral[b] Parameter	Comments	CG Source (Hermsen *et al.* 1977)	Identification
		l (degrees)	*b*						
2CG 006−00.....	3	6.7	−0.5	1.0	2.4	0.39±0.08		...	...
2CG 010−31.....	1	10.5	−31.5	1.5	1.2	...		...	...
2CG 013+00.....	4	13.7	+0.6	1.0	1.0	0.68±0.14		...	...
2CG 036+01.....	3	36.5	+1.5	1.0	1.9	0.27±0.07		...	...
2CG 054+01.....	3	54.2	+1.7	1.0	1.3	0.20±0.09		...	...
2CG 065+00.....	4	65.7	0.0	0.8	1.2	0.24±0.09		CG 64+0	...
2CG 075+00.....	5	75.0	0.0	1.0	1.3	...	could be an extended feature	CG 75−0	...
2CG 078+01.....	5	78.0	+1.5	1.0	2.5	...		CG 78+1	...
2CG 095+04.....	3	95.5	+4.2	1.5	1.1	...		...	...
2CG 121+04.....	3	121.0	+4.0	1.0	1.0	0.43±0.12		CG 121+3	
2CG 135+01.....	3	135.0	+1.5	1.0	1.0	0.31±0.10		CG 135+1	...
2CG 184−05.....	4	184.5	−5.8	0.4	3.7	0.18±0.04		CG 185−5	PSR 0531+21
2CG 195+04.....	3	195.1	+4.5	0.4	4.8	0.33+0.04	γ195+5	CG 195−4	...
2CG 218−00.....	3	218.5	−0.5	1.3	1.0	0.20±0.08		...	...
2CG 235−01.....	2	235.5	−1.0	1.5	1.0	...		...	...
2CG 263−02.....	4	263.6	−2.5	0.3	13.2	0.36±0.02		CG 263−2	PSR 0833−45
2CG 284−00.....	1	284.3	−0.5	1.0	2.7	...	could be an extended feature	...	...
2CG 288−00.....	1	288.3	−0.7	1.3	1.6	...		...	...
2CG 289+64.....	2	289.3	+64.6	0.8	0.6	0.15±0.07		CG 291+65	3C 273
2CG 311−01.....	2	311.5	−1.3	1.0	2.1	...		CG 312−1	...
2CG 333+01.....	3	333.5	+1.0	1.0	3.8	...		CG 333+0	...
2CG 342−02.....	5	342.9	−2.5	1.0	2.0	0.36±0.09		...	...
2CG 353+16.....	4	353.3	+16.0	1.5	1.1	0.24±0.09		...	ρ Oph
2CG 356+00.....	1	356.5	+0.3	1.0	2.6	0.46±0.12	prob. variable	...	...
2CG 359−00.....	3	359.5	−0.7	1.0	1.8	...		...	...

[a] Assuming E^{-2} spectra.

[b] Intensity ($E > 300$ MeV)/Intensity ($E > 100$ MeV), assuming E^{-2} spectra calculating both intensities.

Figure 1.1: The second COS-B catalogue. (from Swanenberg et al. 1981)

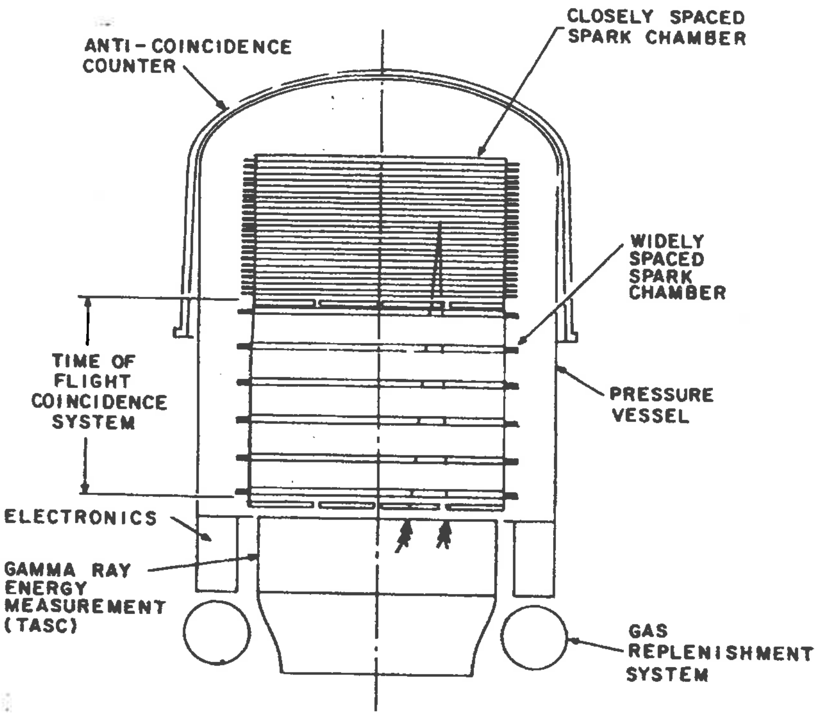

Figure 1.2: Schematic diagram of the EGRET HE gamma-ray telescope (from Kanbach et al. 1988).

been searched for sources of high energy gamma-rays (Swanenberg et al. 1981). A total of 25 sources were found and published as the second COS B catalogue (see figure 1.1). Both the Crab and Vela pulsars were seen, identified by their characteristic periods. Surprisingly, Cygnus X-3 which was seen by SAS-2, was not detected by COS B.

GRO

The Gamma-Ray Observatory (GRO) was launched on April 5, 1991, and if all goes well it should remain operational until the mid 1990's. GRO has four instruments (BATSE, OSSE, COMPTEL, EGRET) for studying gamma-rays over the energy range of less than 100keV to greater than 10GeV. Of the four instruments, EGRET (Energetic Gamma-Ray Experiment Telescope) is studying the highest energy gamma-rays. EGRET, a spark chamber telescope (see figure 1.2), has an energy threshold of 30MeV and will detect gamma-rays with energy as high as 30GeV. The effective collecting area of EGRET is approximately 2000cm^2. For gamma-rays in the middle range of EGRET's sensitivity (100MeV to several GeV) the energy resolution is about 15%. EGRET has a field of view of 40° (FWHM), with angular resolution in the range 0.1° to 0.4°.

Early analysis of GRO EGRET data has identified 17 point sources with significance greater than 7σ. A total of 60 sources have been seen above 4σ, although some of these will almost certainly be due to statistical fluctuation (Hunter 1993a). Figure 1.3 shows a gamma-ray sky map from early EGRET data.

1.4 UHE and VHE Gamma-ray Production

1.4.1 Production Mechanisms

Above 100 GeV there are only a small number of viable mechanisms for producing gamma-rays. The most important of these are

- Meson Decay - When an energetic nucleon interacts with other nuclei it is raised to an energetic state. When the nucleon decays to a lower energy state it emits π and k mesons (π^o,$\pi^{\pm}$,$k^{\pm}$). The most important of these is the π^o which decays to two high energy photons. This mechanism allows an accelerated beam of nucleons to be efficiently converted into high energy gamma-rays.

- Synchrotron emission - A relativistic electron moving through a transverse magnetic field will emit radiation via the synchrotron process. This process is relatively inefficient, as the energy of the electron is several orders of magnitude above the energy of the gamma-ray produced.

- Inverse Compton Effect - High energy gamma-rays may be produced by the interaction of low energy photons with relativistic electrons via the inverse Compton process.

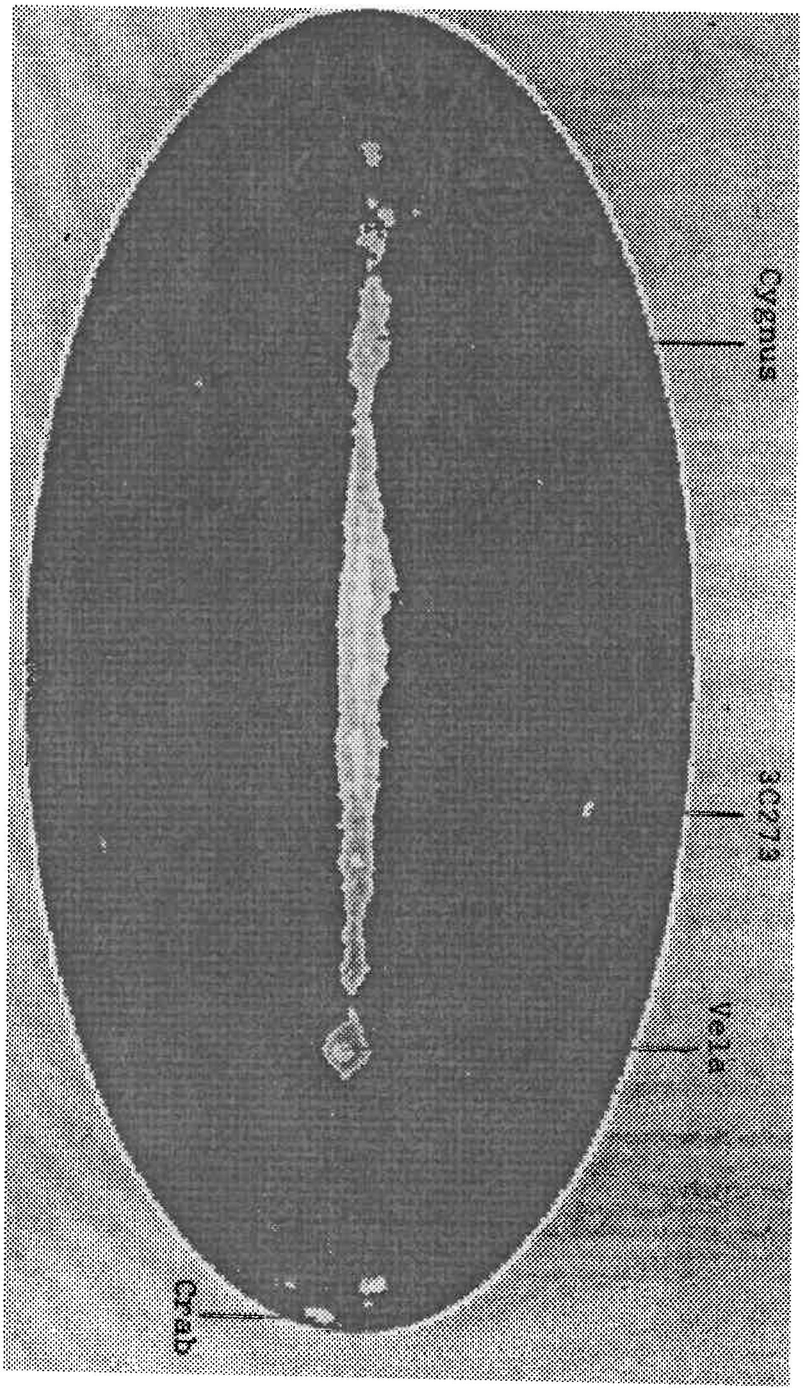

Figure 1.3: EGRET skymap (Hunter 1993b).

1.4.2 Photon-Electron Cascading Through the Cosmic Microwave Background

One of the advantages of using gamma-rays to study high energy environments is that they are able to travel relatively unimpeded through space. In 1965 Penzias and Wilson discovered the cosmic microwave background. The microwave background is believed to be the remnant of photons produced during the "big bang" at the beginning of the universe. The subsequent expansion of the universe has cooled these photons which now exhibit the characteristics of black body emission at 2.7 K. The energy density of the microwave background is 1 eV cm^{-3} which translates to a photon density of 10^3 photons cm^{-3}.

Shortly after its discovery it was realized that the microwave background would severely attenuate UHE gamma-rays traveling large distances (Jelley 1966, Gould and Schreder 1966). Photon-photon pair production ($\gamma + \gamma(3K) \Rightarrow e^+e^-$) becomes important for gamma-rays of energy above 10^{14}eV, with attenuation peaking at 2PeV (see figure 1.4).

The interaction length for photon-photon pair production for a photon of energy 10^{15} eV is of the order of 10 kpc. This would suggest that extra galactic sources of UHE gamma-radiation should not be observable. This is in contradiction to reported observations of neutral radiation (presumably gamma-rays) from Cen A (Clay et al. 1984) and LMC X-4 (Protheroe and Clay 1985). Cen A, at a distance of

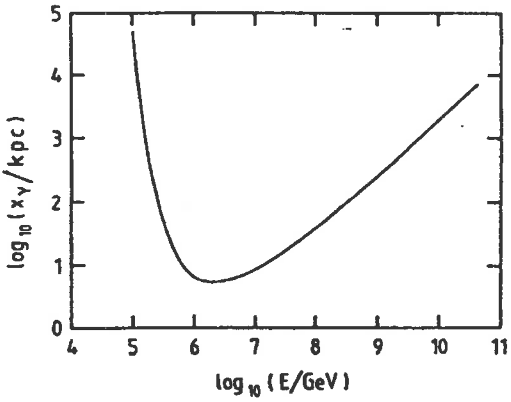

Figure 1.4: The mean interaction length of photons for photon-photon pair production in the microwave background (from Protheroe 1986).

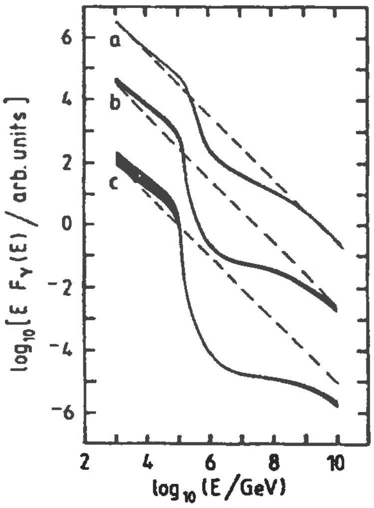

Figure 1.5: Differential energy spectrum of gamma-rays at distances of (a)50kpc, (b)500kpc and (c) 5Mpc (from Protheroe 1986).

6Mpc, is more than 600 interaction lengths from the earth for gamma-rays of energy 10^{15} eV. LMC X-4, at 50kpc, is still more than five interaction lengths from us at an energy of 10^{16} eV. Even Cygnus X-3 (Samorski and Stamm 1983) is greater than one interaction length from earth at 10^{15} eV, which should cause severe attenuation of gamma-rays from this source.

One possible explanation of these observations is that the gamma-rays are partially replenished by inverse Compton scattering of the pair produced electrons in the cosmic microwave background. Typically, in pair production, one of the electrons retains a large fraction of the energy of the initial gamma-ray. Subsequent inverse Compton scattering gives most of the energy of the electron to the gamma-ray that is produced. For this process to work efficiently the intergalactic magnetic fields must be weak enough ($< 10^{-7}$ gauss) that the synchrotron losses of the electron do not dominate the inverse Compton process. If the electrons are to retain the original direction of the initial gamma-ray then further restrictions must be placed on the value of the inter-galactic magnetic fields ($B< 10^{-10}$ G).

Protheroe (1986) has performed detailed Monte Carlo simulations of the photon-electron cascading through the microwave background. He concludes that for a local galaxy, such as the LMC, the observed gamma-ray spectrum would have a dip at $10^{14} - 10^{16}$ eV and a small peak just below 10^{14} eV (see figure 1.5). For Cen A the

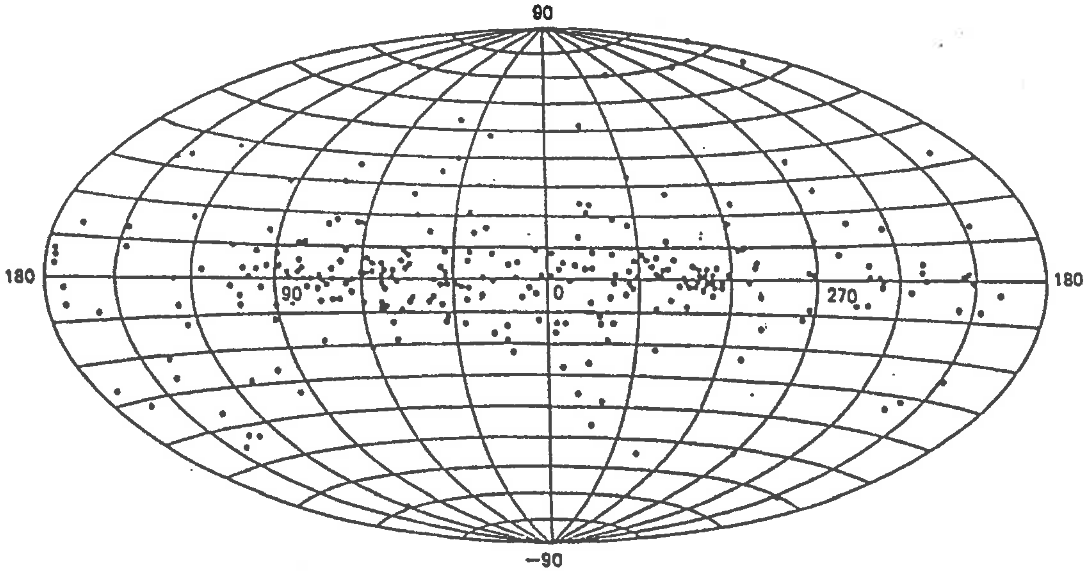

Figure 1.6: Distribution of radio pulsars in galactic coordinates (from Shapiro and Teukolsky 1983).

10^{15} eV gamma-ray flux would be attenuated to 10^{-3} of its original level. Cascading of $10^{18} - 10^{19}$ eV photons through the microwave background could produce observable $10^{15} - 10^{16}$ eV photons at earth but this would require enormous luminosity above 10^{18} eV.

1.4.3 Gamma-ray Production Environments

The following section will give a brief description of some possible environments for the production of VHE and UHE gamma-rays.

1.4.3.1 Radio Pulsars

Pulsars are believed to be highly magnetized rapidly rotating neutron stars. They are characterized by highly polarized bursts of broadband radio emission seen at very regular time intervals. Since the first reported observation of a pulsar (Hewish et al. 1968) hundreds of pulsars have been detected. The spatial distribution of detected pulsars indicates that they lie within the galaxy (see figure 1.6). The pulsar rotational periods vary from just over a milli-second to several seconds, although the vast majority lie in the range 0.1s to 2.5s.

If pulsars are neutron stars then they must be created mainly as a result of supernova explosions where the outer layers of the progenitor star are blown off, leaving a supernova remnant (SNR) around a neutron star. Typically the radio pulsars that are observed are no longer associated with their SNR. Two notable exceptions to this are the young radio pulsars in the Crab and Vela SNR.

A "canonical" neutron star has a radius of 10km and a mass of around $1.4\mathrm{M}_\odot$. If the progenitor star is a good conductor then the conservation of the magnetic field during the collapse of the core leaves the neutron star with a large magnetic field ($\sim 10^{12}$G). The conservation of the angular momentum of the original star will also lead to the rapid rotation of the neutron star. The rotation will be limited to periods above a level where the neutron star would be torn apart by centrifugal forces. For a neutron star of mass M and radius R the maximum angular speed will be given by

$$\Omega^2_{max} = \frac{GM}{R^3} \tag{1.3}$$

where G is the gravitational constant. If the average density of the neutron star is $\overline{\rho}$ then the minimum period will be

$$\mathrm{P}_{min} = \frac{\sqrt{3\pi}}{\mathrm{G}\overline{\rho}}\ \mathrm{s} \tag{1.4}$$

For a neutron star of radius 10km and mass $1\mathrm{M}_\odot$ equation 1.4 gives a period of roughly 1ms.

The magnetic field of a neutron star will co-rotate with the star out to a distance where the tangential velocity of the field is equal to the speed of light. This distance defines the radius, R, of the "light cylinder", where

$$\mathrm{R} = \frac{\mathrm{c}}{\Omega_{NS}} \tag{1.5}$$

Beyond the light cylinder the field lines emanating from the neutron star are swept back (see figure 1.7), applying a retarding torque on the star. Assuming that the moment of inertia of the star remains constant, the change in period due to this torque is given by Paccini (1968) :

$$P^2 = P_0^2 + A^2 B_0^2 t \tag{1.6}$$

where

P = period at time t

P_0 = period at time 0

$A^2 \simeq 2 \times 10^{-39} G^{-2} s$

B_0 = pulsars surface magnetic field

(1.7)

Measured values of P and $\dot{P}$ show that pulsars have an average magnetic field of around 10^{12} G. Paccini (1968) has derived the rate of energy loss of a pulsar through dipole radiation

$$\dot{E} \simeq -\frac{B^2 R^6 \Omega^4}{6c^3} \text{ erg s}^{-1} \tag{1.8}$$

At the present time there is no self consistent model that can explain all of the observed features of pulsars. There are models, however, which can explain the basic features of radiation emission from pulsars.

Standard Model

Goldreich and Julian (1969) have shown that a rotating neutron star with a strong magnetic field will produce a large electric field with a component parallel to the magnetic field. The strength of the electric field is such that charged particles are removed from the surface of the star creating a plasma filled magnetosphere. The positive and negative charges are separated around the null surface, where $\vec{\Omega}.\vec{B} = 0$ (see figure 1.7). The strength of the magnetic field around the star constrains particles to move along the field lines. The particles that are attached to the field lines within the light cylinder will co-rotate with the neutron star. Particles which are attached to the open field lines are accelerated out beyond the light cylinder into space. The potential drop along the field lines is capable of accelerating charged

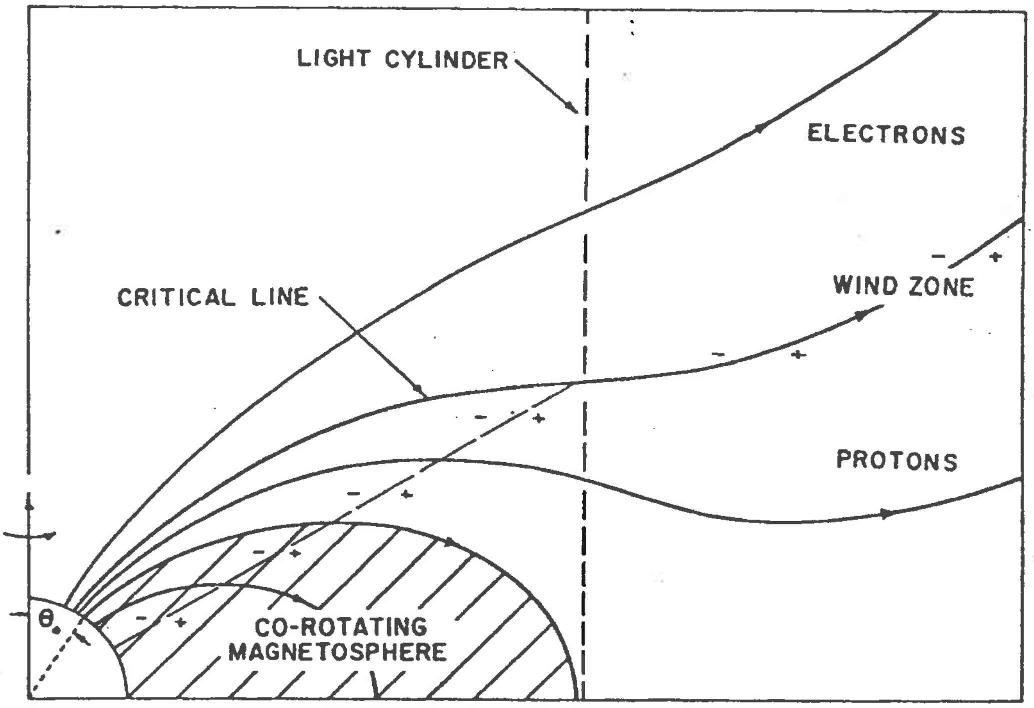

Figure 1.7: Goldreich and Julian Magnetosphere (from Curtis Michel 1982).

particles to very high energies. The maximum energies that particles can attain is given by

$$E_{max} = 3 \times 10^{12} \frac{ZR_6^3 B_{12}}{P^2} \text{ eV} \qquad (1.9)$$

where Z is the atomic charge and R_6, B_{12} and P are in units of 10^6cm, 10^{12}G and seconds respectively. For the Crab pulsar this would accelerate protons to 2×10^{16}eV (Goldreich and Julian 1969). For electrons, which would suffer synchrotron losses, the maximum attainable energy would be somewhat less.

The original model of Goldreich and Julian considered the case where the magnetic and spin axes were aligned. In order to produce pulsed radiation the model would need to be altered so that the magnetic axis is tilted away from the spin axis.

The Outer Gap Model

The outer gap model (Cheng et al. 1986a,b) has provided a mechanism for pulsed emission from infra-red to GeV gamma-ray photons in the Crab and Vela pulsars. It also provides a mechanism for producing unpulsed VHE gamma-rays.

The outer gap model predicts the formation of a region of charge depletion in the magnetosphere of a pulsar.The gap is bounded by the last closed field lines from below, by the null surface from inside, by the light cylinder from the outside and by a boundary charge layer from the top. In general, pair production in the magnetosphere of a pulsar prevents the formation of electric field potentials parallel to the magnetic field. In the gap, however, $E.B \neq 0$ leading to a large potential drop across the gap ($\sim 10^{15}$ eV). The potential accelerates electron positron pairs which emit curvature radiation as they move along the curved magnetic field lines. The photons always move away from the gap because the field lines are convex. These photons will cascade through photon-photon pair production (with radiation emitted further up the gap) and synchrotron emission to produce gamma-rays with energies as high as a few GeV. The electron-positron pairs that leave the gap through the light cylinder can produce VHE gamma-rays by inverse Compton scattering with the infra-red photons filling the magnetosphere of the pulsar. The directions of the electrons leaving the gap become randomized as the open field lines become tangled, and eventually merge with the magnetic field of the interstellar medium. If the electron trajectories become sufficiently randomized the pulsed emission becomes smeared out giving a DC signal at these energies.

1.4.3.2 Binary X-ray Sources

Binary x-ray systems consist of a star and a compact object (neutron star, black hole or white dwarf) orbiting around a common center of mass. X-ray satellites, launched since the 1970's, have found that galactic x-ray emission is dominated by these sources. Figure 1.8 shows the celestial distribution of x-ray sources.

X-ray binary systems are divided roughly into two classes on the basis of the mass of the companion star, M_{opt}. If the companion star has mass $M_{opt} > 1M_{\odot}$ then the binary is classed as a "massive" system. Examples of massive x-ray binary systems are Cyg X-1 and Cen X-3. When the companion has a mass of around $1M_{\odot}$ or less, the binary is classed as a "low mass" system. Her X-1 and Cyg X-2 are examples of low mass x-ray binaries.

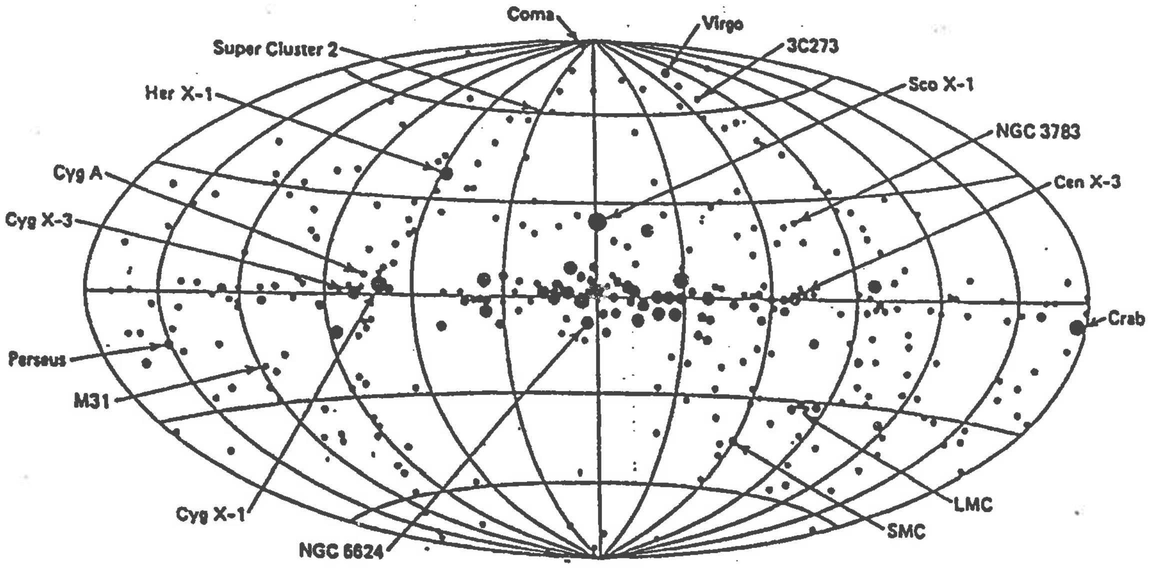

Figure 1.8: Distribution of x-ray sources in galactic coordinates (from Forman et al. 1978).

The evolution of an x-ray binary is more complex than that of an isolated radio pulsar because of the mass transfer between the two stars. A typical binary system, of interest to gamma-ray astronomers, would comprise a main sequence or post main sequence star and a pulsar. The pulsar would most often be a highly magnetized rotating neutron star, formed as the result of a supernova explosion. More than 50 binary pulsars have been observed with x-ray periods from ~ 50ms to ~ 1000s.

The emission of radiation from these systems is assumed to be powered by the accretion of material onto the neutron star. The accreting material may be from the stellar wind of the companion or because of the Roche lobe overflow of the companion. In the case of Roche lobe overflow the companion fills its Roche lobe causing material to flow through the inner Lagrange point. The large angular momentum of the accreting material causes an accretion disk to form around the neutron star. In the case of stellar wind accretion, the gravitational field of the neutron star captures matter from the stellar wind of the companion. The accreting material may not have sufficient angular momentum to form an accretion disk. This may lead to spherical accretion, although the exact nature of the accretion will depend upon the flow of the stellar wind and the magnetic field of the neutron star.

The magnetic field of the neutron star will funnel accreting material onto the poles of the star. As the material decelerates it is heated producing thermal x-rays. The large gravitational potentials associated with neutron stars produce accretional luminosities that are typically in the range 10^{36} to 10^{38} ergs/s. To a good approximation the x-ray luminosity, L_x, of an accreting binary system will be given by the rate at which accreting material is losing gravitational potential energy :

$$L_x \simeq \frac{G\dot{M}M_x}{R_x} \text{ erg s}^{-1} \tag{1.10}$$

where M_x and R_x are the mass and radius of the neutron star and $\dot{M}$ is the rate of mass transfer from the accretion flow. The maximum luminosity available from accretion is given by the "Eddington luminosity", L_{Ed}. The Eddington luminosity occurs when the gravitational force on the accreting material is balanced by the outward radiation pressure. For spherically symmetric accretion

$$L_{Ed} = 1.3 \times 10^{38} \frac{M_x}{M_\odot} \text{erg s}^{-1} \tag{1.11}$$

VHE Gamma-ray Production in Binary X-ray Systems

Several models have been proposed to explain the production of gamma-rays with energy greater than 1TeV in x-ray binary systems. All models rely on the production of energetic particles which then radiate or interact with other matter to produce gamma-rays. Here the models will be discussed in two broad classes, dynamo models and shock acceleration models.

Dynamo Models

Section 1.4.3.1 described a mechanism for accelerating particles to high energies in isolated pulsars (Cheng et al. 1986a). Cheng and Ruderman (1989) have suggested that this model may be extended to pulsars in accreting binary systems. It is not clear, however, if the ambient gas in the environment of a binary system would quench the gaps in the pulsar magnetosphere where particle acceleration occurs.

Chanmugam and Brecher (1985) have suggested a "disk dynamo" model for particle acceleration based on a model for accreting black holes by Lovelace (1976).

Acceleration is due to a potential set up across the accretion disk by the interaction of the magnetic field of the neutron star and the magnetic field of the accretion disk. The maximum energy that a particle will attain is given by

$$E \simeq 3.5 \times 10^{14} B_{12}^{-\frac{3}{7}} L_{38}^{\frac{5}{7}} \text{ eV} \tag{1.12}$$

Gaisser (1990)

where B_{12} is the surface field of the neutron star in units of 10^{12}G and L_{38} is the luminosity in units of 10^{38} erg/s. This model would only provide large potentials for low magnetic fields, and so would not appear to work for systems such as Her X-1.

Shock Acceleration Models

During shock acceleration kinetic energy is transferred from a moving magnetized plasma to an individual particle. The particle suffers a series of collisionless scatterings, gaining energy as it crosses back and forth across the shock. Shock acceleration is known to be an efficient method of accelerating particles to high energies. A number of models have been proposed that involve shock acceleration in different regions of accreting binary systems.

Eichler and Vestrand (1985) have proposed that shock acceleration could take place where matter accretes onto the neutron star surface. A collisionless shock is expected to form above the surface, and could provide an environment for accelerating particles up to PeV energies. Charged particles are assumed to scatter back and forth across the shock, gaining energy with each crossing. One problem with this model is that charged particles ejected from the acceleration region would be drawn to the surface of the neutron star by the strong magnetic fields of the star. Kazanas and Ellison (1986) have suggested that the accelerated particles would interact with the dense plasma in the shock, producing neutrons which could then escape the acceleration region. This accretion shock mechanism appears to be feasible only if the magnetic field of the neutron star is not too high (Nagle et al. 1988).

Quenby and Lieu (1987) and Kiraly and Meszaros (1988) have proposed a "jet termination shock" model. Here a jet of near relativistic particles generated at the pulsar produces a shock as the jet collides with accreting matter further out from the pulsar. Depending on the geometry of the beam and the strength of the magnetic fields, particles accelerated in this shock could reach PeV energies.

Another possible source of acceleration is in a "pulsar wind shock" (Gaisser et al. 1987). The shock forms at the interface of a relativistic wind of particles, driven by the pulsar, and the inside of the supernova remnant. In a binary system the shock would occur with the interaction of the pulsar wind and the wind of the companion, or with the atmosphere of the companion itself (Harding and Gaisser 1989). Bignami et al. (1977) originally suggested this mechanism as an alternative to accretion for producing x-ray emission in binary systems. The pulsar wind shock model would appear to be viable for only those systems containing a neutron star that was rotating sufficiently rapidly. If the claims of a 12ms pulsar in Cyg X-3 are correct (Chadwick et al. 1985), then this mechanism could be possible in the Cyg X-3 binary system.

1.4.3.3 Active Galactic Nuclei

Active galactic nuclei (AGN) are galaxies whose radiation is dominated by a bright central nucleus. AGN comprise about 2% of all observed galaxies. Depending upon their emission characteristics, AGN are classified into groups which include sources such as quasars, Fanaroff-Riley radio galaxies, BL-Lacertae objects and optically violent variables (OVV).

It is believed that AGN are powered by accretion of matter onto a massive black hole ($M > 10^8 M_\odot$) (Rees 1984). Radio observations of some AGN show that jets of energetic electrons are emitted from the central regions of these galaxies. It is now believed that many classes of AGN are the same type of source, but viewed at different angles with respect to these jets (Dermer and Schlickeiser 1992).

Of most interest to gamma-ray astronomers are AGN classed as blazars, which include BL-Lacertae objects and OVV. Blazars are characterized by strong optical polarization, rapid optical variability and flat spectrum radio emission. It is believed that blazars are AGN whose jets are aligned toward us. Of the 14 extra-galactic sources of gamma radiation seen in early EGRET data, all show evidence of blazar

Name	Galactic location*	Type†	z	S(2.7 GHz) (Jy)	α(2.7 to 5 GHz)
Mkn 421	1101 + 384	BL Lac	0.031	0.57	−0.32
3C 273	1226 + 02	SL	0.158	38.9	−0.05
3C 279	1253 − 05	OVV/SL	0.538	11.2	−0.59
3C 454.3	2251 + 158	SL	0.86	10.0	−1.37
PKS 0537 − 441	0537 − 441	BL Lac	0.894	3.84	0.02
PKS 0420 − 014	0420 − 014		0.915	2.15	0.01
PKS 0235 + 164	0235 + 164	BL Lac/SL	0.94	1.94	−0.59
PKS 0208 − 512	0208 − 512		1.003	3.56	0.17
CTA 102	2230 + 11	SL	1.037	5.3	0.67
4C 15.05	0202 + 149		1.202‡	3.0	0.43
4C 38.41	1633 + 38		1.814	2.53	−0.78
OG 147	0528 + 134		1.928‡	2.97	−0.43
0836 + 710	0836 + 710	SL	2.16	3.15	0.39
0716 + 714	0716 + 714	BL Lac/SL(?)	?	0.98	−0.22

Figure 1.9: AGN detected above 100MeV by EGRET (adapted from Dermer and Schlickeiser 1992).

properties at other wavelengths (see figure 1.9) (a more complete AGN source list will be available in Fichtel (1994) containing 21 definite and 10 possible AGN seen by EGRET). Of the 14 EGRET sources in table 1.9 only one, Markarian 421, has been seen at VHE energies (Punch et al. 1992). The interaction of VHE gamma-rays with the cosmic microwave background limits those sources that can be seen at these energies to only the closest AGN.

A number of models have been proposed to explain the production of gamma-rays from AGN. It is generally believed that gamma-ray production occurs in the radio jets of AGN (Dermer and Schlickeiser 1993). Energetic electrons in the jets produce gamma-rays by Compton scattering with either photons emitted from the accretion disk (Dermer et al. 1992) or from scattered UV photons (Sikora et al. 1993). The predicted angular distributions of gamma-rays produced in the jets suggests that AGN whose jets point directly toward us would be weaker sources than those viewed at a slight angle (Dermer et al. 1993).

1.5 Hercules X-1

Hercules X-1 was first seen in 1938 (Hoffmeister 1941) as an irregular variable optical star. Studies of archival plates indicate that optical activity switches between high and low activity roughly every 10 years (Jones et al. 1973). Her X-1 lies 5.8 kpc from Earth and about 1kpc above the galactic plane. Being unobscured by the dust of the galactic plane it has been studied over a large range of wavelengths, from infra-red, optical, ultra-violet and x-ray to VHE and UHE gamma-ray.

Hercules X-1 is thought to be a close, low mass X-ray binary. The system comprises a 1.3 $M_\odot$ neutron star and a 2.18 $M_\odot$ companion orbiting at a distance of approximately 9 $R_\odot$. The low inclination of the orbit causes the neutron star to be completely eclipsed by its companion once each orbit.

The Hercules X-1 system is a strong x-ray source, with most of the energy (bolometric luminosity=2×10^{30} W) emitted as x-rays. X-rays from Her X-1 were first seen more than 20 years ago and it is now the best studied of all x-ray binaries.

Hercules X-1 has not been seen at high energies by SAS-2 or COS-B satellites, and so far it has not been seen by the EGRET detector aboard the GRO.

1.5.1 X-ray Observations of Hercules X-1

The x-rays from Her X-1 are due to thermal emission powered by the accretion of matter from the companion onto the neutron star. At x-ray wavelengths Her X-1 displays three distinct periodicities

- a 1.24s periodicity associated with the rotation of the neutron star.
- a 1.7 day binary orbital period.
- a less well defined 35 day period.

The 35 day period is characterized by three different states of x-ray emission. During the first 11 days of the 35 day cycle the x-ray emission is in a “high on” state, there is also a “low on” state lasting for several days in the middle of the 35 day phase. For the rest of the 35 day cycle the x-ray emission is turned off.

During the high on state the 1.24s period shows a strong main pulse and a much weaker interpulse 180° from the main peak. During the low on state the main peak and the interpulse are of similar intensity (see figure 1.10).

There have been a number of models proposed to explain the 35 day cycle of Her X-1. Trümper et al. (1986) have proposed the precession of the neutron star

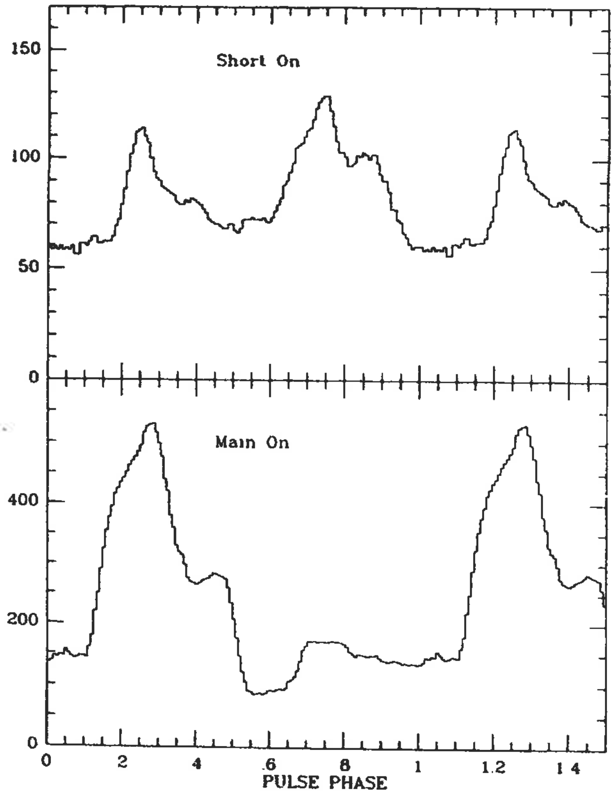

Figure 1.10: X-ray light curves for Her X-1 during low on state (top) and high on state (bottom) (from Petterson et al. 1991).

with a period of 35 days. More recently Petterson et al. (1991) have explained the 35 day cycle in terms of the precession of a twisted tilted accretion disk.

1.5.2 VHE and UHE Gamma-ray Observations of Hercules X-1

Hercules X-1 was first seen at VHE energies by the Durham group in April 1983 (Dowthwaite et al. 1984). The observation was made using four air Čerenkov telescopes (threshold energy $\sim$ 1 TeV) located at Dugway, Utah. During a series of 40 minute drift scans they found a 33% counting rate increase that lasted for three minutes. A period analysis indicated a strong modulation at the known X-ray pulsar period. The overall statistical significance of the pulsed detection was estimated to be 7×10^{-5} and the time of the excess corresponded to an orbital phase of 0.76. X-ray data taken shortly after this indicated that Her X-1 may have been at the beginning of its 35 day cycle. The peak gamma-ray flux of this observation was 1.2×10^{-9} photons $cm^{-2}s^{-1}$ corresponding to a gamma-ray luminosity above 1TeV of 8×10^{36} erg s^{-1}. Further observations of Her X-1 by the Durham group in July and October of 1983 did not show any significant emission.

During the same observing season Her X-1 was observed above 500 TeV by the Fly's Eye detector (Baltrusaitis et al. 1985). A period analysis was performed on 5 nights of data (July 10-14) that showed only a small signal. Only one of the nights, July 11, showed a significant signal at the X-ray period. This observation, lasting 40 minutes, was at orbital phase 0.66 and 35 day phase 0.63 and had a statistical significance of 2×10^{-4}. A simultaneous observation of Her X-1 at lower energies by the Durham group did not confirm this result.

Hercules X-1 was observed extensively by the Whipple air Čerenkov telescope from 1984 onwards. Between 1984 and 1988 observations were made with the medium resolution camera, and with the high resolution camera from May 1988 (see section 4.2.2). An early analysis of this data indicated pulsed emission from Her X-1 in about 10% of observations. Included in these data were three apparently very significant results confirming the emission of VHE gamma-rays from Her X-1. On April 4, 1984 both Whipple and Durham saw emission at the X-ray period lasting about 30 minutes (Chadwick et al. 1987, Gorham et al. 1986a). Her X-1 was in its high on state (phase 0.2) and at orbital phase 0.4. The Durham group estimated the statistical significance to be 3×10^{-3}, and 8×10^{-4} for the Whipple group. On June 16, 1985 a pulsed signal with a period blue-shifted from the X-ray period was seen after the eclipse of the X-ray source (orbital phase 0.914-0.962)(Gorham et al. 1986b). The 35 day phase was 0.36 and the statistical significance was estimated to be 4×10^{-5}. During the period May-July 1986 there were three independent detections of the blue-shifted emission from Her X-1. Haleakala (Resvanis et al. 1988), Whipple (Lamb et al. 1988) and Los Alamos (Dingus et al. 1988) all reported emission blue-shifted by 0.16% from the known x-ray period. The statistical significances of these observations were respectively 7×10^{-3}, 3×10^{-3} and 2×10^{-4}. The energy threshold of the Los Alamos array was 50TeV, while the thresholds of Haleakala and Whipple were less than 1TeV.

Despite the availability of camera data for the Whipple group, no image analysis was used in the original reports of emission from Her X-1. Reynolds et al. (1991) have more carefully analyzed the Whipple data set, including the effect of image cuts on the signals already reported. The results of this work have cast doubt on some of the earlier claims of positive signals from Her X-1. Reynolds et al. split the data set into non-overlapping 30 minute intervals. A Fourier analysis was performed on these segments at the expected x-ray period and the distribution of Rayleigh powers was compared to the calculated background distribution. For the medium resolution camera data a Fisher test yielded a chance probability of 5×10^{-3} that the two distributions came from the same parent distribution. When image analysis was performed on this data, the distribution of Rayleigh powers showed no significant difference between the signal and background regions. The failure of the image cuts to enhance any signal in the uncut data led to the conclusion that no gamma-rays were emitted from Her X-1 at the X-ray period. An *a posteriori* test for emission blue-shifted from the X-ray period yielded a nominal statistical significance of 2.0×10^{-5}. Once again image analysis of this data failed to increase the significance of this result. The data base for the high resolution camera was analyzed in a similar fashion. There was no statistically significant signal either before or after image cuts were applied.

As mentioned previously, the Whipple data set contained two examples of apparent periodic signals that were also seen by other groups. Reynolds et al. have examined these episodes in detail. The data of April 4 1984 has been re-examined, and the results cast some doubt on the presence of a genuine signal. The actual significance of the result before image analysis was increased by combining the measured DC excess (2.0σ) and the Rayleigh power at the X-ray period. It was found, however, that an image analysis reduced the significance of both the DC and pulsed excesses.

The Whipple data from the detection of the blue-shifted emission reported by Haleakala, Whipple and Los Alamos was also examined. The overall significance of the three detections may be as low as 8×10^{-7}, but the two experiments capable of identifying gamma-ray showers did not see gamma-ray like events in their data. For the Whipple group these events did not produce gamma-ray like images, and for the Los Alamos group the muon content of the events was far larger than expected for gamma-ray induced EAS. This has led to some speculation about the existence of a new low mass, long lived neutral particle. In the most recent observations of Her X-1 (Reynolds et al. 1993) the Whipple group used an enhanced image analysis ("supercuts") to search for gamma-ray emission. No evidence for steady emission from Her X-1 was seen with an upper limit on the flux of 3.3×10^{-12} $\mathrm{cm^{-2}s^{-1}}$.

There have been a number of reported episodes of low significance emission from Her X-1. At air Čerenkov energies ($E \geq 1$TeV), both the Haleakala (Austin et al. 1990) and Babha (Rawat et al. 1990) groups have reported bursts containing events pulsed at or near the X-ray period. A long term flux of 1.8×10^{-13} $\mathrm{cm^{-2}s^{-1}}$ above 200 TeV has been reported by the Baksan group (Alexeenko et al. 1990). The Leeds group report a 1.7σ DC excess over three years at a median energy of 1.2 PeV corresponding to a flux of 1.3×10^{-13} $\mathrm{cm^{-2}s^{-1}}$ (Bloomer et al. 1990). The observations of the Leeds group also shows some evidence for sporadic emission. The largest daily excess corresponded to a significance of 5×10^{-5}.

Reports from some more recent array experiments suggest that Her X-1 has turned off at UHE energies. The CASA-MIA detector, with a median energy of 140 TEV, has been collecting data since April 1991. An analysis of a data set containing over 400 million events shows no evidence for steady emission or bursts on timescales of 1 transit for those events from the direction of Her X-1 (Borione et al. 1993). Data from the CYGNUS array, taken from April 1986 to January 1993, have been analyzed. Searches for enhanced emission were made on a large number of timescales from 3.3 minutes to 1458 days. No significant excess was found. A variety of period tests were performed around the X-ray period for each time interval but no significant episodes were seen (Alexandreas et al. 1993).

In summary, there are a large number of reported detections of neutral radiation from Her X-1 at both VHE and UHE energies. The failure of events apparently from Her X-1 to appear "gamma-ray" like has cast doubt on some of these claims. Despite the increasing sensitivity of detectors, recent observations do not confirm earlier reports of emission from Her X-1.

1.5.3 Period Shifted Emission from Hercules X-1

In the previous section there was a reference to blue-shifted emission seen by three independent observatories (Haleakala, Whipple and Los Alamos). Each group reported pulsed emission at a period blue-shifted by 0.16% from the X-ray period of Her X-1. The amount of blue-shifting is significantly different from the X-ray period, which is known very accurately. It is assumed, therefore, that the period shifting does not reflect the true spin rate of the pulsar, but rather is associated with the gamma-ray production mechanism. There have been a number of other reports of period shifted emission from Her X-1 (Weeks 1989). The majority of these observations report emission that is blue-shifted from the x-ray period.

In this section I will discuss three models that have been proposed to explain period shifted gamma-ray emission from Her X-1.

Aharonian and Atoyan (1991)

In the model of Aharonian and Atoyan the period shifted emission is caused by clouds of matter ejected by the companion star HZ-Her. These clouds, of mass 10^{22}g to 10^{23}g are ejected from the surface of the star with initial velocities of $\sim 3 \times 10^{7}$cm s^{-1} by some unknown mechanism. It is supposed that these clouds provide a target for particles accelerated at the neutron star. These particles are scattered by the tangled magnetic fields of the cloud and interact with the matter in the cloud to produce gamma-rays. The relative motion between the cloud, the source of accelerated particles and the observer causes the period shifting of the gamma-ray signal (double doppler shift). Depending upon the motion of the cloud the gamma-ray signal could be either red or blue-shifted. A gamma-ray signal could be seen at any orbital phase, including when the pulsar is eclipsed by its companion. Aharonian and Atoyan predict that this mechanism could produce period shifts of the order of 0.1%. The duration of emission would be limited to the lifetime of the cloud under intense heating by the particle beam. The typical lifetime of such a cloud would be of the order of one hour.

While this model does predict many of the features of the observed period

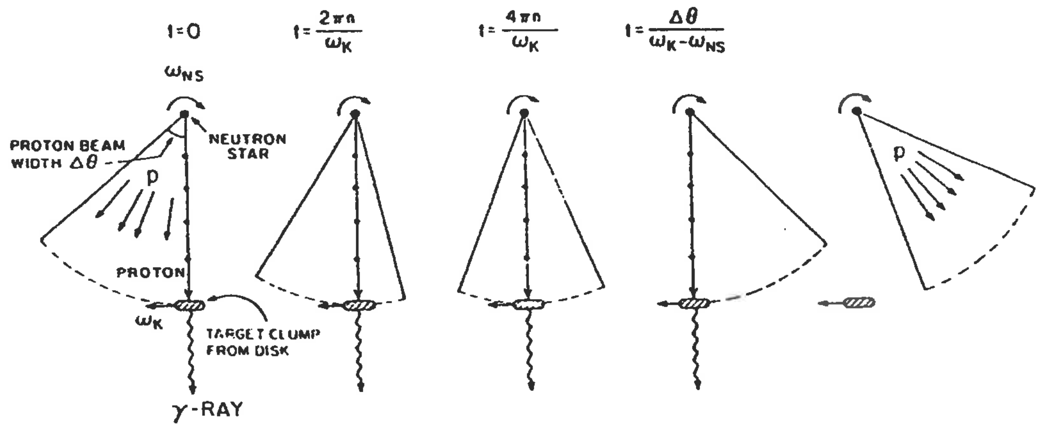

Figure 1.11: Schematic diagram for the production of period shifted emission from Her X-1. The diagram shows the successive illumination of a small chunk of matter, with time increasing from left to right (from Slane and Fry 1989)

shifted emission it does seem to fail in one respect. If the clouds are ejected randomly we would expect a different period shift from each cloud. This is in contradiction to the observations of Haleakala, Whipple and Los Alamos, who saw emission at the same blue-shift over a period of several months.

Slane and Fry (1989)

Slane and Fry suppose that turbulence near the inner edge of the accretion disk ejects chunks of matter from the accretion disk. This matter sits above the accretion disk in an orbit of period $\mathrm{P_k}$ around the neutron star. In general $\mathrm{P_k}$ will be different from the rotational period of the neutron star $\mathrm{P_{ns}}$. These clouds of matter then act as targets for a wide fan beam of particles accelerated at the neutron star. The observed period of gamma-ray emission is then the rotational period of the rotating matter rather than the rotational period of the neutron star (see figure 1.11). If the target material remains in a stable orbit for a large number of rotations then the length of the emission time will be given by

$$\tau = \frac{\Delta\theta}{2\pi}\left(\frac{1}{\mathrm{P_k}} - \frac{1}{\mathrm{P_{ns}}}\right)^{-1} \tag{1.13}$$

where $\Delta\theta$ is the angular width of the fan beam of particles. Typically τ would have a value of 10^3 seconds.

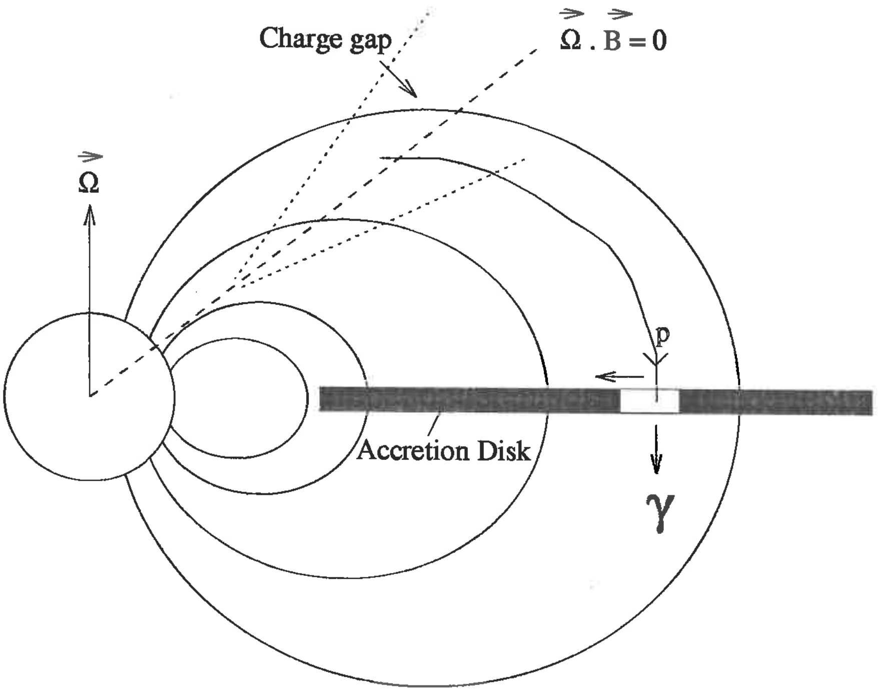

Figure 1.12: Protons accelerated in the gap are directed by the magnetic field onto the accretion disk. Those protons striking the low density bubble will produce observable gamma-rays. The movement of the window will cause the gamma-rays to be blue-shifted from the period of the protons.

The rotating chunks of matter will eventually become trapped in the magnetic field lines of the neutron star, and will co-rotate before being accreted onto the neutron star. Slane and Fry estimate that their model could produce period shifts of the order of 0.1%.

As with the model of Aharonian and Atoyan, this model would seem to have difficulty in producing period shifted emission at the same period over large timescales.

Cheng and Ruderman (1989)

The model of Cheng and Ruderman assumes that the accretion disk itself acts as a gamma-ray production target. A beam of accelerated particles is bent by the magnetic field of the neutron star onto the accretion disk (see figure 1.12). Normally the accretion disk would be too thick for the gamma-rays produced to escape. If a low density "bubble" were to travel down the accretion disk this would provide a window from which gamma-rays could be observed. Blue-shifting of the signal would be due to the movement of the bubble toward the neutron star and the changing geometry of the particle beam needed to illuminate the target. The speed of the window would be determined by the radial inflow rate of the accretion disk. The duration of gamma-ray emission would be given by the traversal time of the window through the inner disk region. Such a model could provide blue-shifted emission up to 0.1% for periods of the order of 10^3 seconds.

It is not clear if the same blue-shifted period could be sustained for a sequence of such windows. Presumably if the accretion flow rate were constant, windows traversing the disk at different times would show the same blue-shifted gamma-ray emission.

1.5.4 Gamma-ray Emission from Her X-1 During Eclipse

In section 1.5.2 it was mentioned that the Whipple group had reported pulsed emission from Her X-1 during eclipse (Gorham et al. 1986b). This claim was made from a two hour observation on June 16, 1985. Period analysis showed pulsed emission for about 4300 seconds only after the eclipse of Her X-1 by its companion HZ-Her. The pulsed signal was blue-shifted from the X-ray period by 0.075%.

Gorham et al. conclude that line of sight emission from Her X-1 could not explain this observation. Using a reasonable model for the atmosphere of HZ-Her predicts that a primary proton beam could produce observable gamma-rays through the limb of the companion for only 7 minutes after the onset of eclipse.

Gorham and Learned (1986) have proposed a “beam steering” model to explain the observation of June 16. They argue that a proton beam accelerated at the neutron star could be bent onto the limb of HZ-Her by the stellar magnetic field. Protons entering the outer limb of the star with trajectories pointing toward earth would encounter favorable conditions for producing observable gamma-rays (see figure 1.13). As Her X-1 goes deeper into eclipse the energy of protons that could produce observable emission decreases. The secondary particle multiplicity requires protons of energy greater than 10TeV to produce gamma-rays of the energy of 1TeV. This mechanism will also produce gamma-rays on eclipse egress, although for a

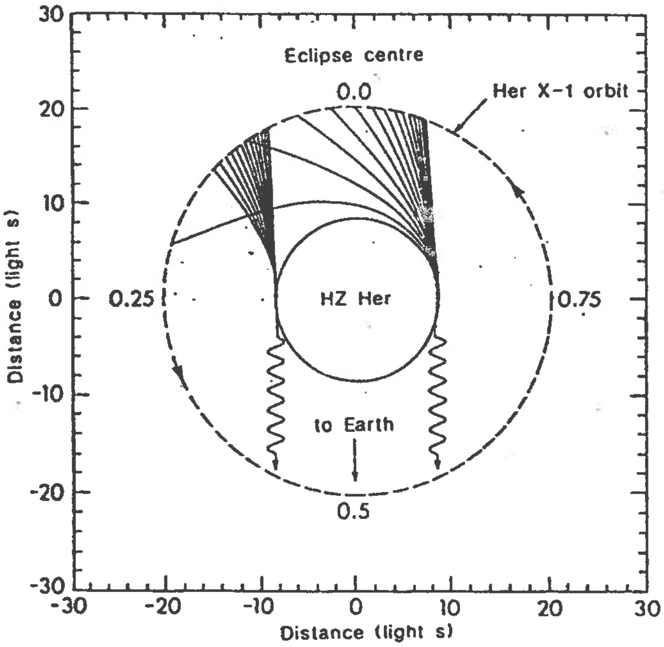

Figure 1.13: The trajectories of protons emitted from Her X-1 that are capable of producing gamma-rays observable at earth. The protons have logarithmically varying energy from 4TeV (most deflected) to 140TeV (least deflected). The surface field of HZ-Her is assumed to be 0.1 G (from Gorham and Learned 1986).

shorter period of time.

This model does not predict that the gamma-ray signal will be blue-shifted from the period of the primary proton signal. In fact the increasing path lengths of the protons as Her X-1 goes deeper into eclipse will give rise to a small red shift in the gamma-ray signal.

Chapter 2

Extensive Air Showers

2.1 Introduction

Observations of primary gamma-rays and cosmic rays at VHE energies are only practical through the study of extensive air showers (EAS) generated as the primary particles interact with the Earth's atmosphere. The dissipation of the energy of the primary into less energetic secondaries with a broad lateral spread increases the effective collecting area of a ground based detector. The penalty for this increase in collecting area is the loss of direct information about the properties of the primary particle. The complexity of the development of EAS means that properties such as primary energy and composition are difficult or impossible to determine with certainty from any ground based detection.
This chapter will include a basic discussion of gamma-ray and cosmic ray initiated EAS.

2.2 Cosmic Ray Initiated EAS

A primary cosmic ray entering the atmosphere will interact with an air molecule well before sea level. The interaction length for a primary containing N nucleons is given by

$$\lambda_N = \frac{Am_p}{\sigma_{N-air}} \tag{2.1}$$

where A=14.5 is the average atomic mass number of an air molecule and m_p is the proton mass. σ_{N-air} is the primary cross section in air and can be parameterized by

$$\sigma_{N-air} = \pi R_0^2(14.5^{\frac{1}{3}} + N^{\frac{1}{3}} - \delta) \tag{2.2}$$

where $\delta = 1.12$ and $R_0 = 1.47$ fm (Westfall et al. 1979).
If the primary is a proton the interaction length is energy dependent and can be described by

$$\lambda_p = 67.2 \left(\frac{E(\mathrm{TeV})}{100}\right)^{-0.065} \mathrm{gcm}^{-2} \tag{2.3}$$

(Dawson 1985).

If the primary is an iron nucleus the interaction is essentially independent of energy, with $\lambda_{Fe} = 13\mathrm{gcm}^{-2}$.

The EAS generated by a cosmic ray will be discussed in terms of the three major components of the shower, namely the nuclear component, the muon component and the electromagnetic component.

2.2.1 Nuclear Component

A cosmic ray proton at air shower energies is considered to interact with an individual nucleon in an air nucleus. The energy lost in this collision goes mainly into the production of pions and some kaons. This process, known as pionization, creates the particles that will feed the muonic and electromagnetic components of the shower. The fraction of energy, K , expended by the incoming particle in a collision is termed the inelasticity, and the number of new particles created is the multiplicity. The incident proton, and perhaps some energetic nucleons from the target nucleus, constitute the fragmentation region of the nucleonic cascade. The particles of the fragmentation region will continue to interact with air nuclei until their energy drops beneath the level needed to generate multiple pions. Once beneath this energy the fragmentation particles will be rapidly attenuated by ionization.

The three types of pion , π^0,π^+,π^-, are produced in roughly equal numbers. The π^0s, with a half-life of 7.6 $\times 10^{-17}$ s, decay almost immediately via

$$\pi^0 \rightarrow \gamma + \gamma$$

The photons produced by this decay go on to initiate the majority of the electromagnetic cascade. The π^+ and π^- have a half-life of 2.6 $\times 10^{-8}$ s and may either decay via

$$\pi^+ \rightarrow \mu^+ + \nu_\mu$$

$$\pi^- \rightarrow \mu^- + \overline{\nu}_\mu$$

or interact further with air nuclei. If a pion interacts it will lose all of its energy in the collision (inelasticity=1). The interaction length of a pion in air is about 120gcm^{-2} at 0.1 TeV, decreasing for increasing energy. The balance between the interaction or decay of a pion is governed mainly by its depth in the atmosphere. The interaction cross section of the neutrinos produced is extremely small, and they are assumed to play no further part in the development of the shower.

Kaons are produced in the nuclear interactions at around one tenth the rate of pions, with all four species of kaon being present: K^+,K^-,K^0 ,$\overline{K}^0$. The two neutral kaon species are differentiated in terms of their decay mode. As with the pions, kaons may either interact or decay through a number of channels, producing pions, muons and electrons.

For a cosmic ray that is a nucleus the simplest treatment of the nuclear interaction is the superposition model (de Beer et al. 1966). In this model a nucleus of mass number A and energy E is assumed to interact as A separate protons of energy E/A. A nucleus interacting in this way will generate an extensive air shower that develops much more rapidly than that of a proton of energy E. The superposition model predicts that the averaging of the showers produced by each nucleon in a nuclear primary will lead to smaller fluctuations in shower development than for a similar proton primary. The superposition model (which does not include nucleon shielding in the nucleus) overestimates the rate of development and underestimates the fluctuations in the cascade .

2.2.2 Muon Component

The muon component of an EAS is due mainly to the decay of charged pions generated by the nuclear interactions at the core of the shower. Small numbers of muons may also be produced by photopion production and by pair production ($\gamma \rightarrow \mu^+\mu^-$).

Muons lose their energy mainly through ionization and decay. For muons at air shower energies the rate of loss of energy through ionization is about $2M$eV/gcm^{-2}, and is approximately constant with energy. Muons may also decay with a half-life of 2.2 $\times 10^{-6}$ s through

$$\mu^+ \rightarrow e^+ + \nu_e + \overline{\nu}_\mu$$

$$\mu^- \rightarrow e^- + \overline{\nu}_e + \nu_\mu$$

A muon incident vertically at the top of the atmosphere with a Lorentz factor greater than 20 will have sufficient time dilation to reach the surface of the earth. Muons of lesser energy will decay, and the electrons produced from this will contribute in a minor way to the electromagnetic component of the cascade. Muons may also generate gamma-rays through bremsstrahlung, but the cross section for this is much smaller than that for the electron, and so can be ignored in the overall development of the shower.

For EAS generated by primaries of energy 10^{11} to 10^{14} eV, muons are the only particles that will survive to sea level in detectable numbers. As the primary energy increases, the particles in the electromagnetic component become relatively more abundant at sea level than the muons. Even at these higher energies the total energy carried by the muons is still comparable to that of the electromagnetic component because of the larger average energy of the muons.

The lateral distribution of the muons in an air shower is much broader than that of the electromagnetic component. This is due to the height of production of the muons and also the transverse momentum of their parent particles. The pions generated in an shower have typical transverse momenta of several hundred MeV/c. Muons at large core distances can survive to ground level because of their lack of catastrophic interaction. Coulomb scattering, which dominates the lateral spreading of the electromagnetic component, is not significant for the muon, which is about 200 times heavier than the electron. For muons (E>1GeV) the lateral distribution is of the form

$$\rho_\mu(\mathrm{r}) \propto r^{-0.75}\left(1+\frac{r}{k(s,\theta)}\right)^{-2.5} \tag{2.4}$$

(Greisen 1960)

where k is a function of zenith angle (θ) and shower age (s) (see section 2.2.3 for a description of shower age). For a typical shower above 10^{14} eV at sea level, electrons will dominate near the core, but at larger core distances the relative muon abundance will increase. Beyond 1 kilometer from the core muons will be the dominant particles.

2.2.3 Electromagnetic Component

The majority of the electromagnetic component comes from the decay of neutral pions generated in the nuclear interactions near the core of the shower. In addition to this there is some contribution from the decay of muons and kaons.

The main processes that drive the electromagnetic cascade are pair production

$$\gamma \rightarrow e^+e^-$$

and bremsstrahlung from the acceleration of electrons and positrons in the nuclear field of atmospheric atoms (from now on "electrons"will refer to both electrons and positrons).

For bremsstrahlung the energy losses are of the form

$$\frac{-dE}{dX} = \frac{E}{X_o} \tag{2.5}$$

where X_0 is called the radiation length and is 37.15 gcm^{-2} in air. The interaction length for pair production is $(9/7)X_0$.

Through a succession of these two interactions a high energy gamma-ray or electron produces a cascade of lower energy photons and electrons. This process will continue until the energy of the secondaries drops beneath a critical value (E_c) when

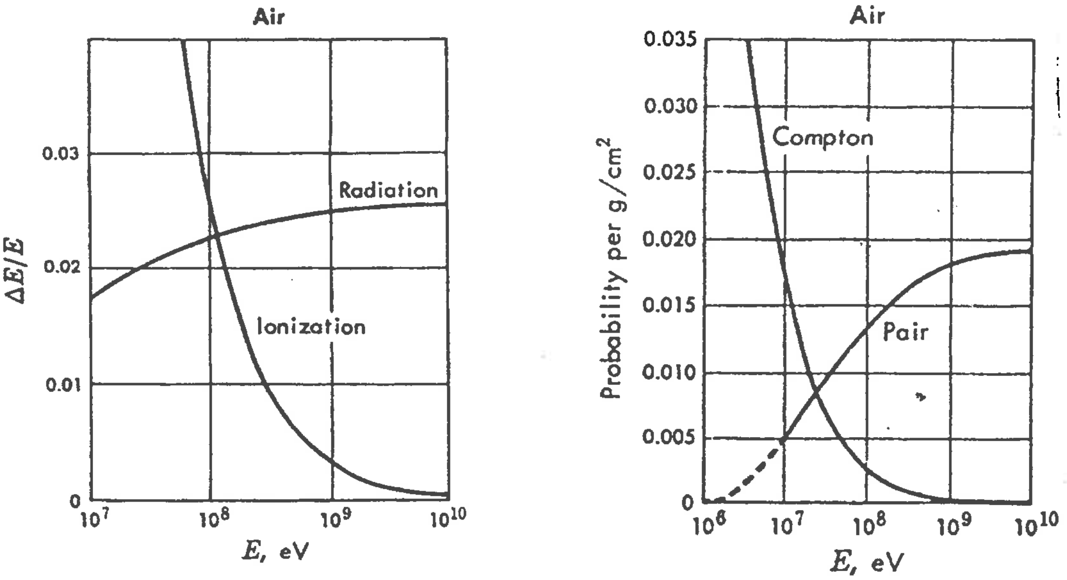

Figure 2.1: The energy loss of electrons through ionization or radiation in air as a function of energy (left). Also shown is the probability per gcm^{-2} of a photon undergoing Compton scattering or pair production in air as a function of photon energy (from Rossi 1964).

other energy loss mechanisms will begin to dominate. For electrons E_c is defined as the energy lost through ionization and excitation while traversing one radiation length. Below E_c ionization energy loss begins to rapidly dominate bremsstrahlung energy loss (fig. 2.1). In air E_c is around 85 MeV. As the energy of the photons of the electromagnetic cascade decreases, energy loss through Compton scattering and the photoelectric effect begins to dominate pair production. Figure 2.1 shows the photon energy loss rate for these processes as a function of photon energy.

The lateral distribution of an electromagnetic cascade is dominated by the Coulomb scattering of the electrons. For multiple Coulomb scattering of an electron of energy E moving a distance δt

$$\langle \delta\theta^2 \rangle = \left(\frac{E_s}{E} \right)^2 \delta t \tag{2.6}$$

(see e.g Gaisser 1990)

where δt is in gcm^{-2} and $E_s \simeq 21$MeV. The natural unit of lateral spread due to coulomb scattering is the Molière unit r_0, which is characteristic of the spread of low energy electrons in a shower. The Molière unit is given by

$$r_0 = \frac{E_s}{E_c} X_0 \tag{2.7}$$

which is 9.3 gcm^{-2} (about 80m) at sea level.

The lateral distribution of the electromagnetic component can be described by the NKG function.

$$f_{NKG}\left(\frac{r}{r_0}\right) = C(s)\left(\frac{r}{r_0}\right)^{s-2}\left(\frac{r}{r_0}+1\right)^{s-4.5} \tag{2.8}$$

where

$$C(s) = \frac{\Gamma(4.5-s)}{2\pi\Gamma(s)\Gamma(4.5-2s)}$$

The NKG function is a theoretical expression for the lateral distribution of a purely electromagnetic cascade (Nishimura and Kamata 1951) modified by Greisen (1956) to fit the observed lateral distribution for cosmic ray showers.

The shower age, (s), is a useful parameterization of the cascade development. It is zero at the start of the shower, 1 at shower maximum and 2 when the shower has decayed to a single particle.

Measurements of the variation in energy of the particles of a shower with core distance show that the average energy of the particles decreases with increasing distance to the core. This is consistent with high energy photons being generated at the core, these initiate cascades producing lower energy electrons which are Coulomb scattered away from the core. The presence of an energy source feeding the electromagnetic component is also indicated by the lack of very high energy gamma-rays or electrons near the core (Greisen 1960). If no such energy source were available then a purely electromagnetic cascade with such a soft spectrum would quickly attenuate.

2.3 Gamma-ray Initiated EAS

2.3.1 Electromagnetic Cascade Theory

A primary gamma-ray entering the Earth's atmosphere will generate an extensive air shower much as for a primary cosmic ray. As the photonuclear cross section is very small, however, it is expected that the number of mesons and nucleons produced will be much smaller than for a cosmic ray EAS. The energy of the primary photon will be rapidly degraded through pair production and bremsstrahlung, producing a cascade that is mostly electromagnetic in character. The initial interaction length for the primary will be that of pair production in air. The basic processes for the propagation of an electromagnetic shower have been discussed earlier in this chapter.

The derivation of an analytical function for the development of an electromagnetic cascade that included all relevant processes would be extremely complex. Using a series of approximations, however, it is possible to explain the basic features of the cascade development. The simplest treatment is called Approximation A (Rossi and Greisen 1941). Under this approximation only pair production and bremsstrahlung are considered. Both processes have an approximately equal interaction length $\sim x_0$. Following Allan(1971), we define x_r as the as the distance in which half the electrons radiate or half the photons pair produce

$$\exp\left(\frac{-x_r}{x_0}\right) = 0.5 \tag{2.9}$$

which gives $x_r = x_0 \ln 2$. After n interactions the total number of secondary particles would be 2^n with an average energy of $E_0/2^n$, where E_0 is the primary energy. The number of particles will grow until the average particle energy drops below the critical energy E_c. Below this energy ionization losses for the electrons begin to dominate bremsstrahlung losses causing a rapid attenuation in the particle flux. Using $E_c = E_0/2^n$ it is possible to define the depth of shower maximum $x_{max} = nx_r$ in terms of the primary energy and the critical energy :

$$x_{max} = x_0 \ln\left(\frac{E_0}{E_c}\right) \tag{2.10}$$

Despite the simple nature of this approximation it does correctly predict several important features of the cascade: the initial exponential growth of the cascade, the relationship between E_0 and the height of maximum, and the relationship between E_0 and the number of particles at shower maximum. More accurate models of the cascade development (Allan 1971) show that the estimate of the total particle number at X_{max}

$$N_{max} = \frac{E_0}{E_c} \tag{2.11}$$

is quite accurate. A more detailed analysis for lower (0.1-1.0TeV) primary energies shows that equation 2.11 overestimates the total particle number by about a factor of 10. A more realistic estimate of N_{max} at these energies is given by

$$N_{max} \simeq E_0(TeV) \times 10^3 \tag{2.12}$$

Despite its ability to predict basic cascade development, approximation A is clearly limited . It gives no account of the distribution of particle energies with depth or of the fluctuations in particle number. A more accurate analysis of cascade development, known as approximation B (Rossi 1952), includes an ionization loss of about 80MeV per radiation length. This leads to a more accurate description of longitudinal development (Greisen 1956) where the particle number N_e is expressed as a function of primary energy E_0 and depth of observation, t

$$N_e\left(E_0, t\right) = \frac{0.31}{\sqrt{t_{max}}} \exp\left(t\left(1 - 1.5 \ln s\right)\right) \tag{2.13}$$

where

$$t_{max} = \ln\left(\frac{E_0}{E_c}\right) = \text{(depth of maximum)}$$

$$s = \frac{3t}{t + 2t_{max}} = \text{(shower age)}$$

and the depths are expressed in terms of radiation lengths. Once past shower maximum an electromagnetic cascade will attenuate rapidly with an attenuation length $\lambda_{em} \sim 130\mathrm{gcm}^{-2}$. For cosmic ray showers the attenuation length has been measured to be slightly longer than this with $\lambda_{cr} \sim 200\mathrm{gcm}^{-2}$ (Bird and Clay 1990).

2.4 Gamma-ray EAS vs. Cosmic Ray EAS

The differences between the development of gamma-ray and cosmic ray EAS are of great interest to observers of gamma-ray sources. The cosmic ray showers form an unwanted background to observations and any method that can reject them is useful.

2.4.1 Muons

It has been mentioned already that a purely electromagnetic cascade is expected to be poor in muons. The major process for the production of muons from electromagnetic cascades is photoproduction

$$\gamma + nucleus \rightarrow hadrons$$

This interaction is similar to a pion-nucleus interaction, with the resulting hadronic interactions generating pions and kaons which decay to produce muons. The relative probability of this compared to electron pair production is $R \sim 2.8 \times 10^{-3}$. Another source of muons from electromagnetic cascades is pair production

$$\gamma \rightarrow \mu^+ \mu^-$$

but the relative probability of this is $R \sim 2 \times 10^{-5}$ that of electron pair production.

Following Gaisser (1990) it is possible to use simple cascade theory to estimate the number of 1GeV muons generated by an electromagnetic shower. For a primary of energy E_0 the average energy per particle will be 1GeV after $n \sim \ln(E_0/1\mathrm{GeV})$ interaction lengths. If a photoproduction does occur in the cascade then the resulting interactions will be hadronic-like, with the energy split equally between hadronic and electromagnetic particles. The probability that any branch of the cascade will be hadronic at the GeV level is $R \times \ln E_0/2$ (for n$R \ll 1$) so that the number of GeV muons in an electromagnetic cascade will be approximately

$$N_\mu^\gamma \sim 0.5 R \ln E_0 \times N_{\mathrm{1GeV}} \tag{2.14}$$

where N_{1GeV} is the number of branches in the shower at 1 GeV. Using this simple model for hadronic showers gives the number of muons at the 1GeV level as

$$N_\mu^p \sim \frac{N_{\mathrm{1GeV}}}{2} \tag{2.15}$$

which gives the ratio of muons expected in gamma-ray showers to cosmic ray showers as

$$\frac{N_\mu^\gamma}{N_\mu^p} \sim R \ln E_0 \tag{2.16}$$

For a shower of energy 10^{15} eV equation 2.16 predicts that a gamma-ray primary will produce about 10% the number of muons of an equivalent cosmic ray primary. One of the major limitations of this model is that the cross section for photoproduction is assumed to be independent of energy. Despite the simplicity of this model it does give a reasonable estimate of the number of muons expected in an electromagnetic cascade.

Given the expectation of muon-poor showers from gamma-ray primaries it has been traditional to make muon cuts when looking at gamma-ray sources. There have been reports, though, of apparently muon rich on-source events. Dingus et al. (1988) reported two significant bursts at energies above 50TeV from the compact binary system Hercules X-1. The observations (made with the CYGNUS air shower array) showed that the events in these bursts were modulated by a period blue shifted from the X-ray period of Hercules X-1. An analysis of the events contributing to this signal showed that they had a larger muon content than background hadronic events. Observations of Cygnus X-3 above 10^{15} eV by the Kiel array (Samorski and Stamm 1983) have shown higher than expected muon densities for on-source events. Those events that were modulated by the 4.8 hour orbital period of Cyg X-3 were shown to have a muon content two thirds of that of the background hadron events. A similar muon density was found in a signal from the Crab nebula (Dzikowski et al. 1981) at an energy of around 10^{16} eV. In contrast to these results is the detection of Cygnus X-3 by the EAS array at Akeno (E> 6×10^{14} eV)(Kifune et al. (1986), where the 4.8 hour orbital period was found in only the muon poor events ($N_\mu/N_e \leq 0.001$). Other apparently high muon content on-source events have been seen from the SUGAR array . SUGAR was a muon sensitive air shower array, with a threshold energy of $\sim 10^{17}$eV. It is expected to have a poor response to muon-deficient showers, but there are indications of on-source excesses from two X-ray binaries, LMC X-4 and 2A 1822-37.1 (Meyhandan et al. 1992, Clay et al. 1992).

In the light of these detections more detailed work was done on the expected muon production from gamma-ray initiated EAS. Edwards et al. (1985) and others concluded that the original estimates of muon number were correct (assuming a logarithmic increase of both photon-nucleon and proton-nucleon cross sections). One way of enhancing the muon content is to assume that photon-nucleon cross section increases rapidly with energy. For primaries of relatively low energy (<PeV) this will not greatly enhance the muon content. The primary energy is rapidly degraded to a level where the $\sigma_{\gamma-air}$ is much smaller. The production of low energy muons is largely independent of any increase in $\sigma_{\gamma-air}$ (Châtelet et al. 1990) because the majority of these muons are produced deep in the atmosphere by low energy photons.
Using a $\sigma_{\gamma-air}$ due to Duke and Owens (1982) (fig. 2.2) Krys et al.(1991) showed that at >PeV energies gamma-rays can produce muons in similar quantities to protons. At lower energies the predicted muon number drops to that of the standard model discussed earlier. If the first interaction of a primary gamma-ray is photonuclear then the cascade that develops is indistinguishable from a hadronic cascade. The probability of this occurring is $\sigma_{\gamma-air}/\sigma_{pair\ production}$.

Experimental measurements seem to disagree with a rapidly increasing cross section. Dumora et al. (1992) showed that the muon to electron ratio predicted by such a cross section is incompatible with measurements made at sea level. Although some objections could be overcome by assuming a certain primary composition, Dumora et al. believe that a rapid increase in $\sigma_{\gamma-air}$ can be ruled out for energies up to 1-10 PeV. For extremely high energy showers $E > 10^{18}$ eV it is predicted that the

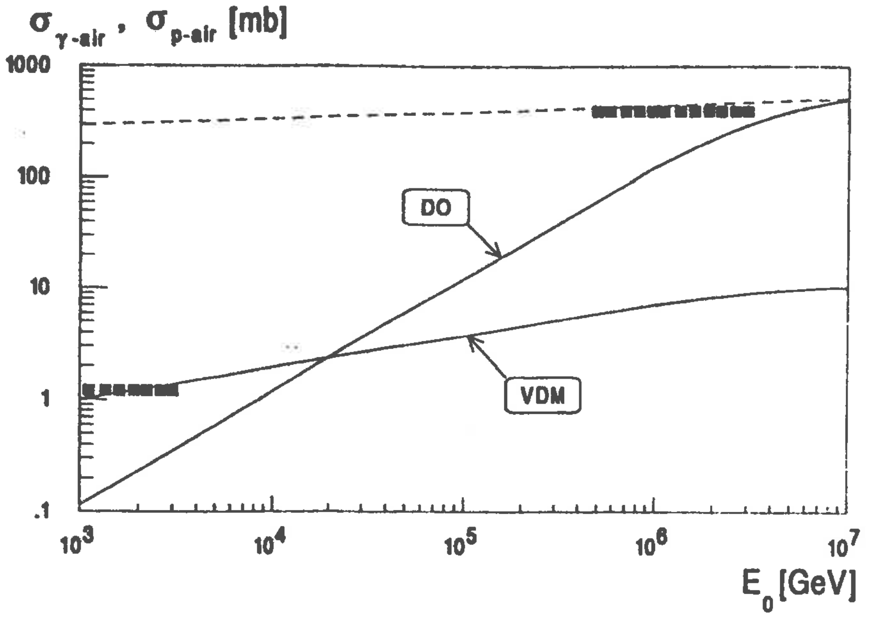

Figure 2.2: [DO] is the estimate of photonuclear cross section $\sigma_{\gamma-air}$ due to Duke and Owens (1982) as a function of interaction energy E. The dashed line is the proton air cross section σ_{p-air} (from Dumora et al. 1992).

numbers of muons generated by gamma and proton primaries will be approximately the same (Aharonian et al. 1991) even without a drastic increase in $\sigma_{\gamma-air}$. Although the numbers of muons are similar at this energy it is expected that the spectrum of muons produced by a gamma-ray primary will be much softer than for a proton primary.

2.4.2 Lateral distribution

In addition to muon cuts, shower age cuts have also been applied to enhance gamma-ray signals. A primary gamma-ray has a shorter interaction length in the atmosphere than a proton primary. A gamma-ray cascade will also develop more rapidly because the entire energy of the primary is fed into the electromagnetic cascade in the first interaction. For a cosmic ray primary the electromagnetic component is fed continually from pions generated by hadronic interactions. It is expected, therefore, that the shower age will be greater for gamma-ray induced EAS than for cosmic ray induced EAS of the same shower size.

Several groups have tried, with apparent success, to enrich the gamma ray signal of source detections . Some examples of an age cut apparently enhancing a signal are for Cygnus X-3 (Samorski and Stamm 1983 ,Tonwar et al. 1988) and Vela X-1 (Protheroe et al. 1984, van der Walt et al. 1987, Suga et al. 1985). Age cuts have also been used to enhance signals from Cygnus X-1 and the Crab at 100TeV (Khristiansen et al. 1990, Gupta et al. 1990) . In contradiction to these results are observations of Cyg X-3 (Lloyd-Evans et al. 1983) where no age cut was used and Kifune et al. (1986) which showed no signal enhancement with age cut.

Monte Carlo simulations of gamma-ray and proton induced cascades have cast some doubt on the use of the age parameter for selecting gamma-ray events. Studies by Fenyves (1985) conclude that shower age is not useful for identifying gamma-ray primaries of energy $10^{14} - 10^{16}$ eV. This work predicts that the shower age of gamma-rays is closer to that of cosmic rays than had been previously predicted and that the age varies greatly from shower to shower. Similar work by Hillas (1987) and Cheung and MacKeown (1988) with Monte Carlo simulations gave the same results. It should be noted however, that these Monte Carlo simulations do not accurately reproduce the observed shower age distribution for cosmic rays.

Chapter 3

The Atmospheric Čerenkov Technique

3.1 Čerenkov Emission Theory

Čerenkov radiation was first noticed by early workers in radioactivity, who found that transparent materials would emit bluish white light when placed near strong radioactive sources. It was Čerenkov in 1934 who began an extensive study of this light, and shortly after this Frank and Tamm (1937) provided the correct theoretical interpretation of Čerenkov light.

When a charged particle traverses matter it polarizes the atoms of the material (see figure 3.1). If the speed of the particle is low compared to the speed of light in the material then the induced field is symmetric and no radiation is emitted. When the speed of the particle is comparable to that of the speed of light in the medium the polarization field is no longer symmetric. As a result of this there will be a net dipole field set up along the axis of particle travel. At each track element along the path of the particle these accelerated dipoles will emit brief pulses of electromagnetic radiation. In most cases the radiation from the different track elements will interfere destructively producing no net radiation. If the velocity of the particle exceeds the phase velocity of light in the medium, however, it is possible for wavelets emitted from all elements of the particle track to interfere constructively. Figure 3.2 shows a

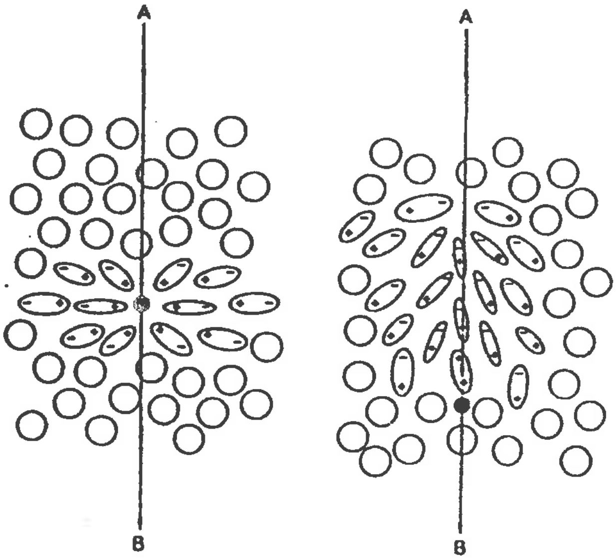

Figure 3.1: The local polarization induced in the molecules of a medium by the passage of a charged particle with low velocity (left) and high velocity (right) (from Jelley 1982).

Huygens construction of such wavelets emitted from a particle track. At a particular cone angle θ_c the wavelets from all parts of the track arrive at a distant point at the same time and traveling in the same direction to form a coherent plane wave front. From figure 3.2 it can be seen that the angle of emission of this radiation will be given by the "Čerenkov relation"

$$\cos\,\theta_c = \frac{1}{\beta \mathrm{n}} \tag{3.1}$$

where β is the particle velocity divided by the speed of light and n is the refractive index.

From equation 3.1 it is possible to deduce a number of important features of Čerenkov radiation:

- for a medium of refractive index n, no radiation takes place beneath an energy threshold for a particular particle :

$$\beta_{min} = \frac{1}{\mathrm{n}} \tag{3.2}$$

- as $\beta \rightarrow 1$ (ultra-relativistic limit), θ_c tends to a maximum value $\theta_{c_{max}}$ given by

$$\theta_{c_{max}} = \cos^{-1}\left(\frac{1}{\mathrm{n}}\right) \tag{3.3}$$

- for most media the dielectric constant will vary with frequency. Čerenkov radiation can only be produced for n>1. This limits the minimum wavelength of Čerenkov light to ultra-violet, with no x-rays or gamma rays being produced.

In order to produce Čerenkov radiation, the particle track length in the medium must be large compared to the wavelengths produced and the particle must maintain a constant velocity. The emission of Čerenkov radiation is a macroscopic process involving the medium as a whole, and it is the medium rather than the particle that emits the light.

The amount of energy E emitted per frequency ν for a particle of charge Ze is described by

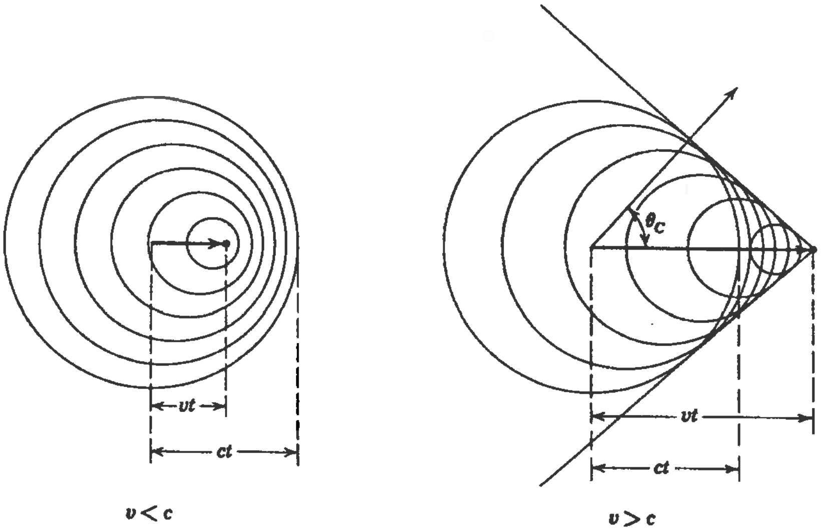

Figure 3.2: Huygens construction of radiation emitted from a particle with velocity less than (left) and greater than (right) the speed of light in the medium. Only if v>c can the wavelets interfere to produce Čerenkov light (from Jackson 1962).

$$\frac{d^2E}{dld\nu} = \frac{4\pi^2Z^2e^2\nu}{c^2}\left(1 - \frac{1}{\mathrm{n}^2\beta^2}\right) \qquad \text{Frank and Tamm (1937)} \tag{3.4}$$

where l is the path length of the particle in the medium. This can be written in terms of the number of photons N emitted per unit path length

$$\frac{dN}{dl} = \frac{2\pi Z^2}{137c}\int_{\beta n>1}\left(1 - \frac{1}{\mathrm{n}^2\beta^2}\right)d\nu \tag{3.5}$$

where $e^2/\hbar c \sim 1/137$ is the fine structure constant. So for a wavelength range $\lambda_1 \rightarrow \lambda_2$ the number of photons emitted in a track length l by a particle of unit charge is

$$N = \frac{2\pi l}{137}\left(\frac{1}{\lambda_2} - \frac{1}{\lambda_1}\right)\left(1 - \frac{1}{\beta^2\mathrm{n}^2}\right) \tag{3.6}$$

It can be seen that the spectral distribution of the Čerenkov light will peak at the smallest wavelengths that can be produced by the Čerenkov process (ultra-violet).

3.2 Čerenkov Characteristics of EAS

Blackett (1948) was the first to suggest that fast charged particles could produce Čerenkov radiation in a gas. This was confirmed, firstly in dense chloroform vapor and later in air. The small refractive index of air leads to a higher Čerenkov energy threshold and smaller emission angle than for water or glass. From equation 3.2 it can be seen that for a particle of rest mass m_0 the minimum energy for Čerenkov production is given by

$$E_{min} = \frac{m_0\mathrm{c}^2}{\sqrt{1 - \frac{1}{\mathrm{n}^2}}} \tag{3.7}$$

Following Jelley (1967) we define the refractive index as n=1+η, where η is small and is dependent upon altitude. If a simple isothermal atmosphere is assumed then η varies with altitude, z, as

$$\eta = 2.9 \times 10^{-4}\mathrm{exp}\left(-\frac{z}{z_0}\right) \tag{3.8}$$

where $z_0 \simeq 7.1$ km is the scale height of the atmosphere. From equations 3.7 and 3.8 it can be seen that at sea level (n=1.00029)

- E_{min} (electron) = 21 MeV
- E_{min} (muon) = 4.3 GeV
- E_{min} (proton) = 39 GeV

Using equation 3.3 we may estimate the dependence of the Čerenkov critical angle on η by

$$\theta_{C_{max}} \sim (2\eta)^{\frac{1}{2}} \tag{3.9}$$

which gives $\theta_{C_{max}} = 1.3°$ at sea level. Compare this to the expected angular deviation due to multiple Coulomb scattering over one radiation length of an electron in an air shower of energy, say, 100MeV (from equation 2.6)

$$\langle \delta\theta \rangle_{RMS} \sim 12° \tag{3.10}$$

This implies that the lateral spread of the Čerenkov light from the lower energy electrons in an extensive air shower will be dominated by the Coulomb scattering of the soft component and not by the Čerenkov emission angle.

The low refractive index of air leads to a much lower photon yield than for a more optically dense material. From equation 3.6 the number of visible photons emitted by a fast particle of unit charge can be estimated by

$$\frac{dN}{dl} \sim 780\eta \text{ photons per cm of particle track} \tag{3.11}$$

For an electron at sea level each meter of track will produce about 22 visible photons. Attenuation of Čerenkov photons in the atmosphere is due mainly to three processes : Rayleigh scattering, aerosol scattering and ozone absorption. None of these processes causes large transmission losses, making it possible to detect the Čerenkov photons from small EAS whose particle flux attenuated well above ground level. For a typical EAS, approximately 50% of the Čerenkov photons emitted will reach ground level.

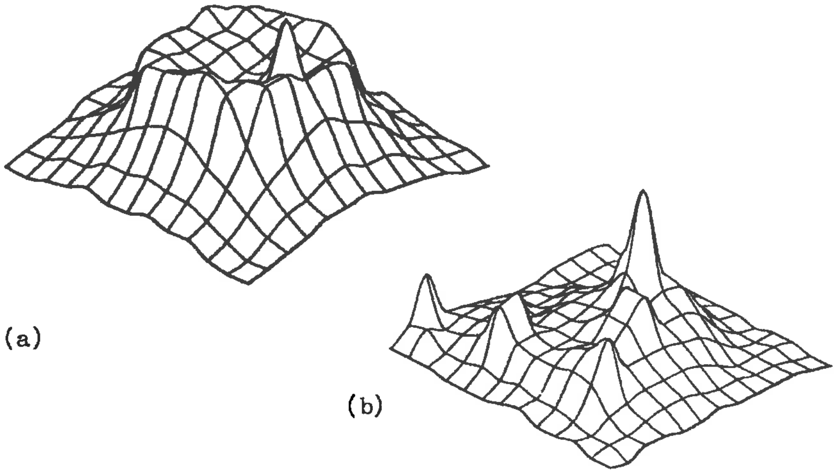

Figure 3.3: Typical Čerenkov photon densities on the ground from EAS initiated by (a) 320 GeV gamma-ray (b) 1TeV nucleon -both showers incident vertically at sea level. The shower axis is at the center of each figure and the grid spacing is 50m (from Hillas and Patterson 1987).

3.2.1 Lateral Distribution

The lateral distribution of Čerenkov light from EAS is of great interest to both VHE gamma-ray astronomers and cosmic ray physicists. For a VHE gamma-ray telescope the collecting area is defined by the lateral spread of the Čerenkov light rather than the physical size of the telescope. Figure 3.3 shows Monte Carlo simulations of the Čerenkov lateral distributions for typical gamma-ray and cosmic ray EAS at sea level.

For gamma-ray initiated EAS the Čerenkov lateral distribution is relatively flat out to distances of about 150m. After this the photon density falls away rapidly ($\propto 1/r^2$), forming a well defined pool of light on the ground. Aside from Poisson fluctuations the Čerenkov lateral distribution of gamma-ray induced EAS varies little from shower to shower. For cosmic ray induced EAS the Čerenkov photon density falls more rapidly with core distance than for a gamma-ray induced EAS. The shower to shower variations in lateral distribution are also much greater, with sharp peaks appearing due mainly to Čerenkov light from local penetrating muons.

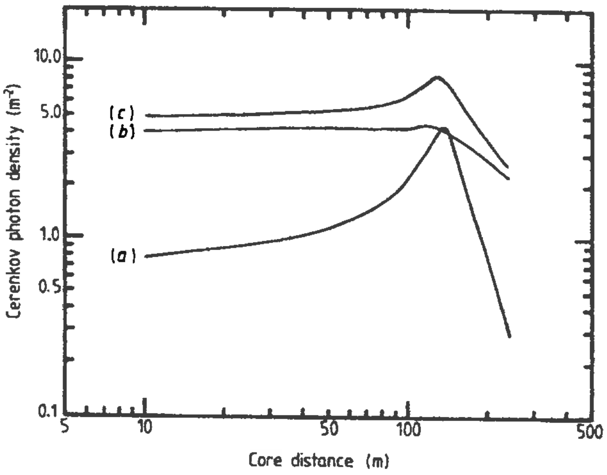

Figure 3.4: Contribution to the lateral distribution of Čerenkov light in gamma-ray induced cascades of energy 100 GeV from electrons of energy (a) $\geq$ 1GeV (b) $<$ 1GeV (c) all energies. These simulations are for a wide angle detector at sea level (from Rao and Sinha 1988).

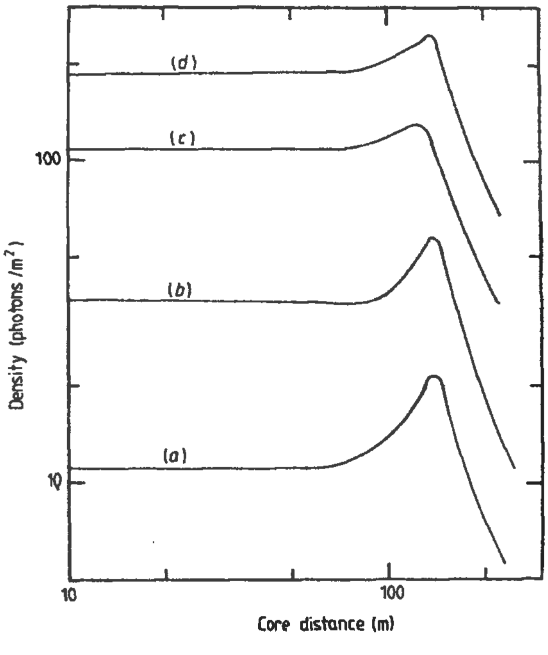

Figure 3.5: Čerenkov lateral distributions for gamma-ray initiated EAS seen by a wide angle detector at sea level for primary energies of (a) 200 GeV (b) 500 GeV (c) 1 TeV and (d) 2 TeV (from Rao and Sinha 1988).

An interesting feature in the lateral distribution of showers that develop early in the atmosphere is the Čerenkov "shoulder". The shoulder is a ring of increased photon density lying about 150m from the core of a vertical shower. Following Hillas (1982) we can explain the shoulder in terms of Čerenkov light emitted from energetic particles moving along the shower axis. These particles will emit Čerenkov light at the characteristic Čerenkov angle θ_c. As the particles penetrate deeper into the atmosphere the Čerenkov angle will increase, but this will be offset by the decreasing height of production of the light. The combination of these two effects leads to a focusing of the Čerenkov light. Light emitted between heights of 7 and 20 kilometers will fall within a ring of radius 110 to 145 meters on the ground.

In reality the focusing of Čerenkov light is dependent upon the particle energy (see figure 3.4) and depth of observation. Multiple Coulomb scattering of low energy electrons causes a blurring of the Čerenkov shoulder. Despite this, Monte Carlo studies indicate that the shoulder should be observable for showers that develop sufficiently early in the atmosphere. This is largely due to a sharp peak in the particle distribution parallel to the shower axis consisting of energetic electromagnetic particles. As the primary particle energy increases and the showers develop deeper in the atmosphere it is expected that the shoulder will be less discernible (see figure 3.5). Despite this, Dawson et al. (1989) have verified the presence of the Čerenkov shoulder at PeV energies.

3.2.2 Angular Distribution

The angular distribution describes the variation in Čerenkov photon density as a function of angular distance from the shower axis. The first detailed calculations of angular distribution were done by Zatsepin (1965). This work assumed that the electromagnetic particles of the cascade were distributed as a Gaussian around the shower axis. This was later shown to be incorrect, but despite this the basic analysis of the features of the angular distribution are still valid. For more recent Monte Carlo calculations of angular distribution see, for example, Fegan (1992). Figure 3.6 shows the Čerenkov photon angular distributions for vertical gamma-ray showers of energy 1TeV and 5PeV and proton showers of energy 1.5 TeV and 4.5 PeV with shower cores at 0, 100 and 400 meters.

For showers observed at the core, the angular distribution peaks at zero degrees, but for larger core distances the peak of emission lies away from the shower axis. The angular position of peak emission is seen to be strongly dependent on core location and weakly dependent upon primary energy. This can be understood by making the reasonable assumption that most of the Čerenkov emission takes place at shower maximum. We would then expect, from simple geometry, that the angle of peak emission would be the angle subtended by the shower axis and a line joining

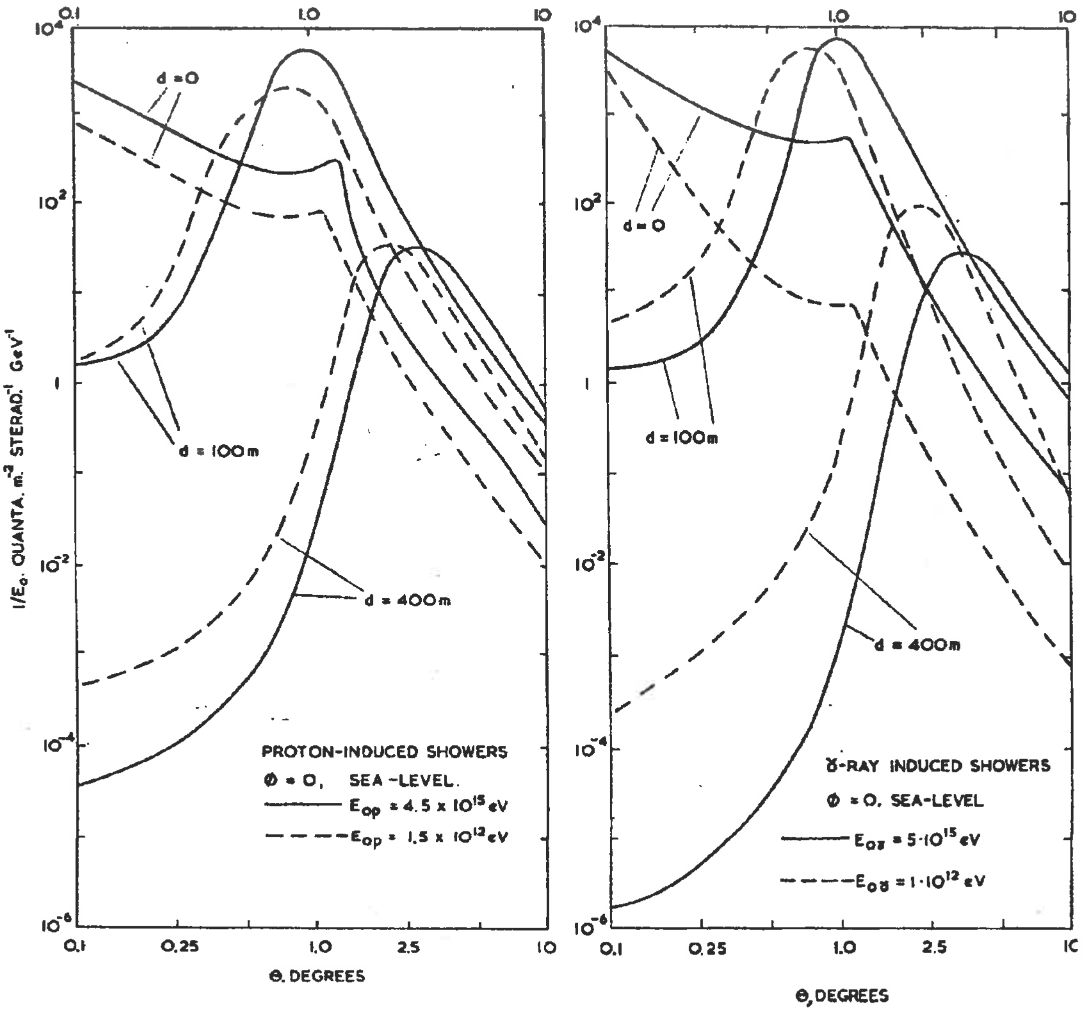

Figure 3.6: Angular distributions of Čerenkov light for proton induced EAS (left) and gamma-ray induced EAS (right) at sea level. The calculations were done by Zatsepin (1965). (From Jelley 1967).

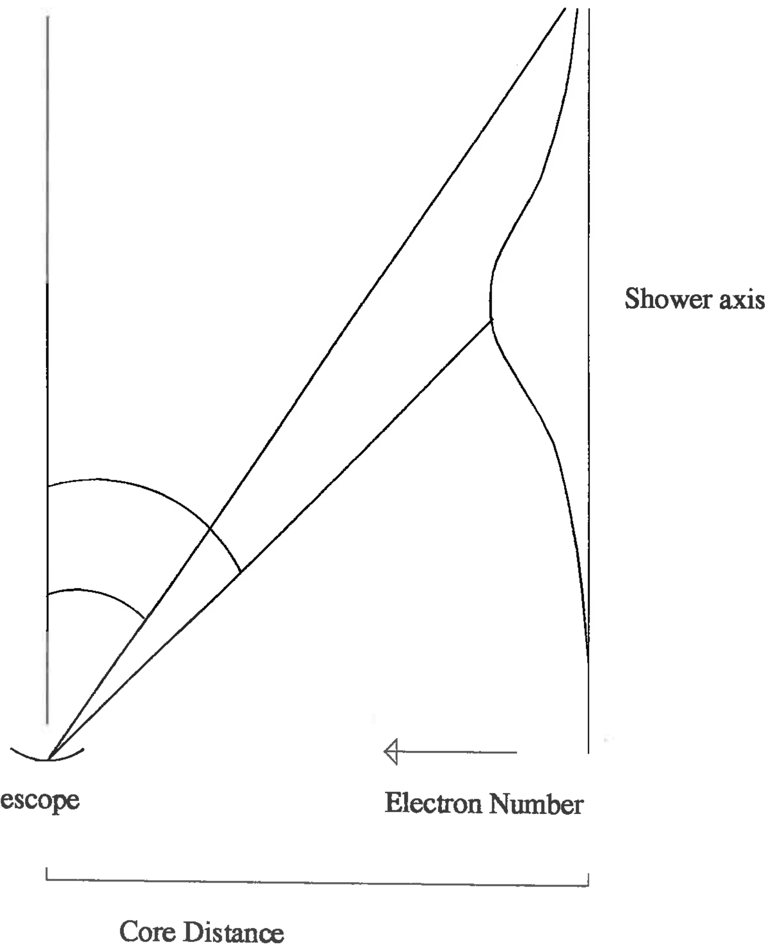

Figure 3.7: Schematic diagram of how various parts of an EAS will appear in the field of view of a telescope. The curve on the right describes the change in electron number with depth. It can be seen that the light emitted lower in the atmosphere will appear at larger angles.

the detector and shower maximum. By this analysis it is expected that showers of the same energy (same depth of maximum) will show an increasing angle of peak emission for increasing core distance. For two showers of different energy at the same core location (for cores distances >0), the shower produced by the more energetic primary will have a greater depth of maximum and therefore a larger peak emission angle.

If the Čerenkov light from the entire shower is considered, then the angular distribution of photons reflects the longitudinal and lateral development of the cascade. Figure 3.7 shows how the Čerenkov emission from various parts of the

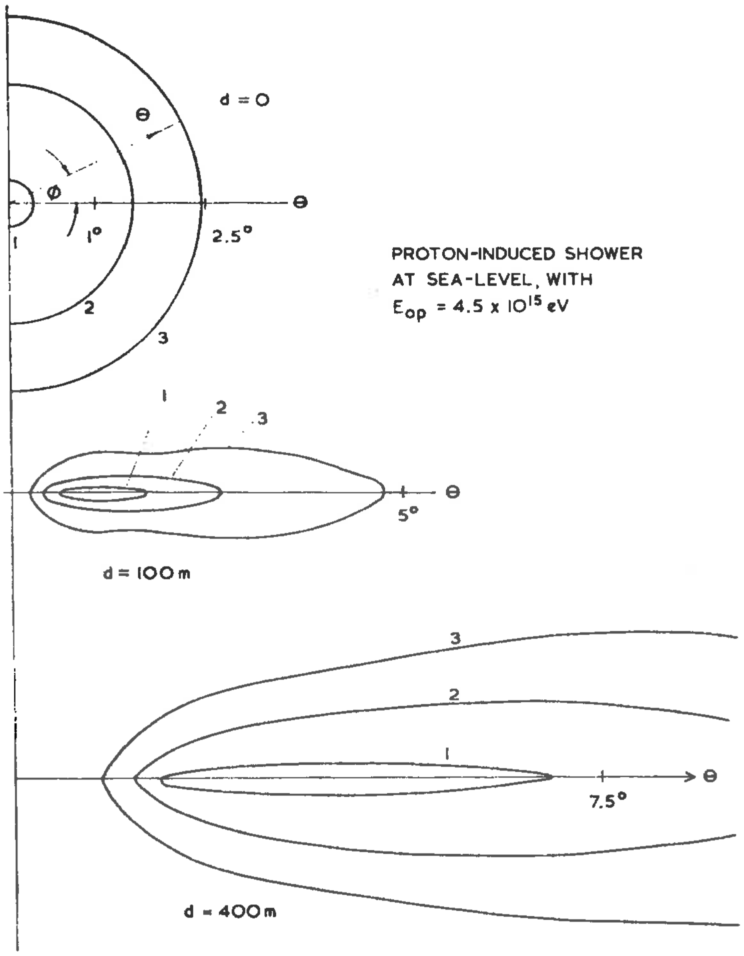

Figure 3.8: Isophote patterns for proton initiated EAS at sea level from Zatsepin 1965. The numbers on the isophotes indicate negative logarithmic intensity of light (from Jelley 1967).

cascade will translate into angular position in the field of view of a Čerenkov detector. Light from the top of the cascade will appear at small angles, light from further down the cascade will appear at increasingly larger angles. Zatsepin (1965) showed how this would lead to the development of images in the focal plane of a Čerenkov detector (fig 3.8).

It can be seen that an EAS with its core at the detector forms a circular image around the center of the field of view. At larger core distances the images are increasingly elliptical, with the length and width of the image being dependent upon the lateral and longitudinal position of the Čerenkov emission. Further consideration of figure 3.7 shows that the major axis of such an elliptical image will point toward the apparent source position of the primary particle. The shapes of Čerenkov images are in basic agreement with image intensifier photographs taken by Hill and Porter (1961).

It was first suggested by Porter and Long (1963) that it may be possible to distinguish between gamma-ray and cosmic ray initiated EAS on the basis of their Čerenkov images. The early work of Zatsepin seemed to show that this would not be possible (Jelley 1967). It was thought that at high energies ($E>10^{12}$) there would not be a large difference between the Čerenkov images of gamma-ray and cosmic ray initiated EAS, and that, at lower energies, fluctuations in cascade development would obscure any differences.

Later work on Čerenkov imaging (Hillas 1985) using more sophisticated Monte Carlo simulation of EAS has shown that differences between gamma-ray and cosmic ray images are large enough to be detected. This has led to a method of Čerenkov imaging that can significantly enhance the gamma-ray signal in VHE Čerenkov observations (see chapter 4).

3.2.3 Design of an Air Čerenkov Telescope

The main problem with observing Čerenkov light from EAS is to distinguish the faint Čerenkov pulses from the background light signal. If the observation site is well away from artificial light sources then the majority of the background is from starlight. The large number of starlight photons collected by a typical air Čerenkov telescope tends to swamp any noise contribution from the photo-tubes. A 1 TeV photon primary will produce about 50 Čerenkov photons per square meter within 100 meters of the core at sea level. The contribution from Čerenkov light due to EAS is about 10^{-4} of the total night sky background. Although the average light contribution from Čerenkov radiation is small, on very short time scales it can dominate the background light. The time spread of the Čerenkov light front is only a few nanoseconds, faster than any other astrophysical or atmospheric light variation. By taking advantage of the short duration of the Čerenkov flashes it is possible to resolve them against the sky background noise.

The simplest air Čerenkov telescope is a single large area mirror focusing light onto a photomultiplier tube. The solid angle subtended by the photo-tube is chosen to match the angular distribution of Čerenkov light produced by EAS. By coupling the photo-tube to fast electronics it is possible to exploit the speed of the Čerenkov flashes by triggering only from those pulses that have very short duration.

Due to the steepness of most gamma-ray source spectra it is optimal to run a Čerenkov telescope at the lowest possible energy threshold (see e.g. Patterson and Hillas 1989). The lower limit to the threshold will be determined by the night sky background (NSB). In most cases the photo-tubes of an air Čerenkov telescope will operate under photoelectron "pile-up" conditions, where single photoelectrons are not resolvable. If this is the case then the NSB will appear as a DC offset on which the air Čerenkov signals will sit. The fluctuations in the NSB will be governed by Poisson statistics, with additional small fluctuations introduced by the photo-tube. For a simple Čerenkov telescope consisting of a mirror of area A, focusing light onto a single photo-tube of quantum efficiency $\epsilon(\lambda)$, the the number of photoelectrons due to the NSB ($\bar{n}_{NSB}$) will be

$$\bar{n}_{NSB} = \mathrm{A}\tau\Omega \int \phi_{NSB}(\lambda)\mathrm{T}(\lambda)\epsilon(\lambda)d\lambda \tag{3.12}$$

where τ is the integration time, Ω is the solid angle subtended by the tube and T is the transmission factor (including mirror reflectivity). The function ϕ_{NSB} is the spectral distribution of NSB photons per unit time per unit solid angle. If we assume that the majority of transmission loss is due to mirror reflectivity (R), and take average values for ϕ and ϵ then

$$\bar{n}_{NSB} = A\tau\Omega R\epsilon\phi_{NSB} \tag{3.13}$$

The number of Čerenkov photoelectrons, n, collected by a photo-tube and mirror from an EAS will be given by

$$\mathrm{n} = \rho_c \mathrm{A}\epsilon R \tag{3.14}$$

where ρ_c is the Čerenkov photon density (this assumes that both Ω and τ are large enough to collect the entire Čerenkov signal). The signal to noise ratio will be given by the number of Čerenkov photons detected divided by the fluctuation in the NSB

$$\frac{\mathrm{S}}{\mathrm{N}} = \frac{\rho_c \mathrm{A}\epsilon \mathrm{R}}{\sqrt{\mathrm{A}\tau\Omega\mathrm{R}\epsilon\phi_{NSB}}} \tag{3.15}$$

Figure 3.9 shows a typical pulse height distribution for a simple air Čerenkov telescope. The line with the steeper slope is caused by triggers due to upward fluctuations in the NSB. The integral spectrum of NSB seen from a photo-tube is well described by a power law of the form

$$N_{NSB}(> h) = kh^{-\nu} \qquad \text{Jelley(1967)} \tag{3.16}$$

where $N_{NSB}(> h)$ is the frequency of recording of pulses of height greater than h and

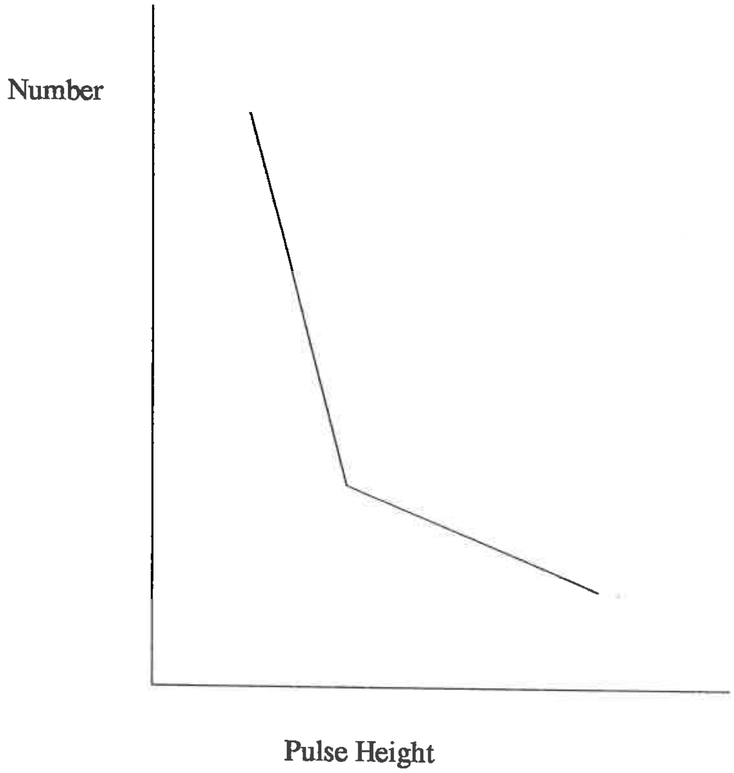

Figure 3.9: Typical pulse height distribution for events triggering a simple air Čerenkov telescope.

k and ν are constants. According to Patterson and Hillas (1989), ν lies typically in the range 8-16. The line with the shallower slope in figure 3.9 is due to the air Čerenkov signal. The slope of this line should reflect the energy spectrum of the primaries that generate the EAS Čerenkov signal. The energy threshold of such a telescope scales as N/S. From equation 3.15 it can be seen that the energy threshold may be decreased by increasing the mirror area A.

A widely employed technique to reduce the energy threshold of an air Čerenkov telescope is to use several photo-tubes in fast coincidence. This may be done using several mirrors, each being viewed by different photo-tubes, or by splitting the Čerenkov image from one mirror between several photo-tubes. The energy threshold of such systems will be determined by the rate of "accidentals" (events caused by chance coincidences in the NSB) that is acceptable for a particular observation. The rate of accidentals from n photo-tubes can be estimated by

$$R_{acc} = \mathrm{n}\tau^{n-1} \prod_{i=1}^{n} R_i \tag{3.17}$$

where R_i is the rate at which each tube exceeds its triggering threshold due to the NSB (singles rate) and τ is the coincidence time window. For the best signal to noise the coincidence time window should be adjusted to the expected length of an air Čerenkov signal .

3.3 The Bicentennial Gamma-ray Telescope

3.3.1 BIGRAT

The BIcentennial Gamma-RAy Telescope (BIGRAT) is located at Woomera in South Australia (longitude 136°47′ E, latitude 31°06′ S). This site is about 500km north of Adelaide and at an altitude of 160m above sea level. The Woomera telescope was first commissioned in November 1988 and has been described in detail elsewhere (Clay et al. 1989).

The original mirrors of the telescope consisted of 55 spherical glass mirrors of focal length 2.66m arranged in three groups of 10m^2. Since 1991 these spherical

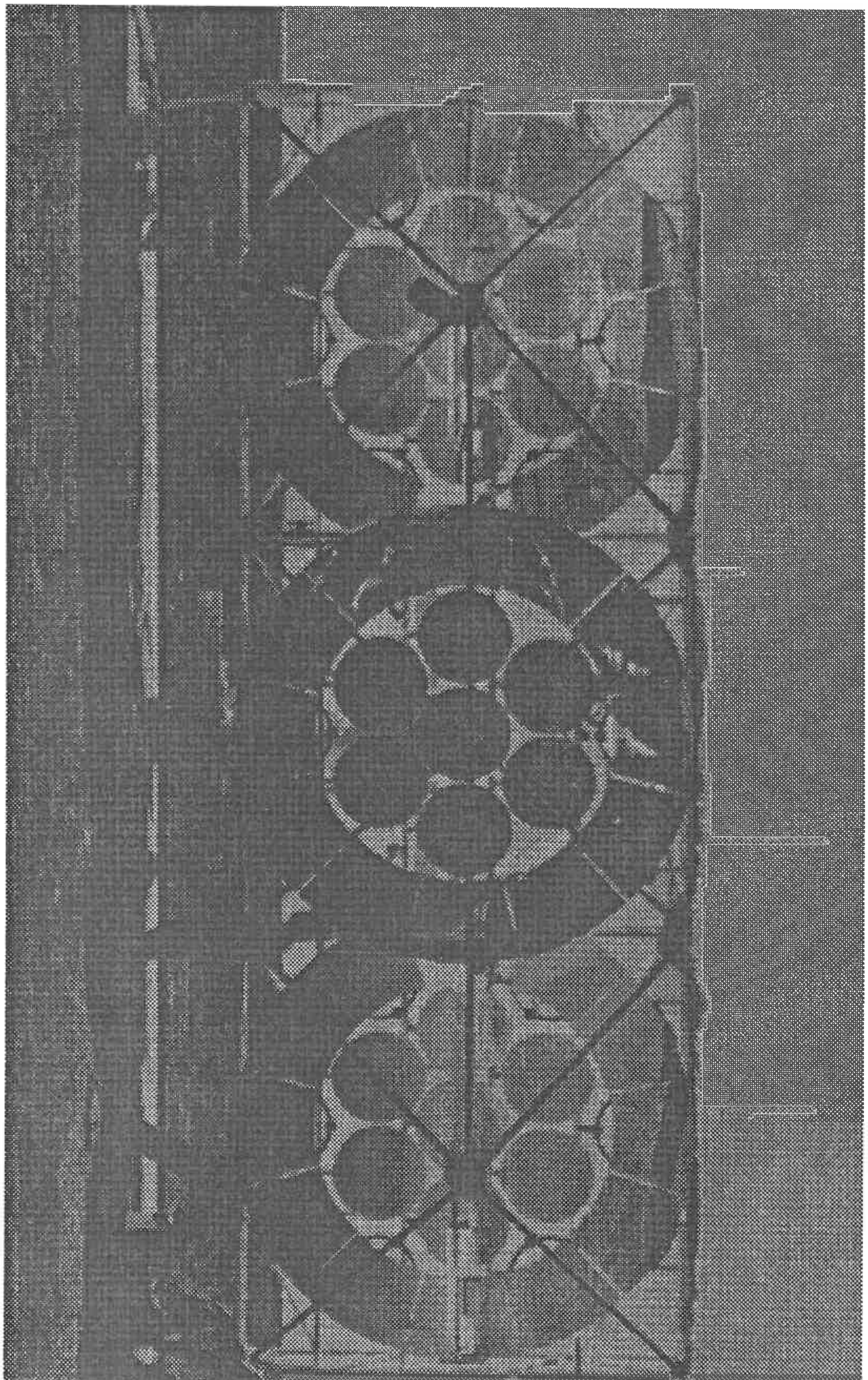

Figure 3.10: BIGRAT

mirrors have been gradually replaced by paraboloidal sections with better focus and greater collecting area. At the focus of each composite mirror is a detector pod of three 51mm RCA 8575 photomultiplier tubes. Each tube in the detector pod is in fast three fold coincidence with its corresponding tubes on the other mirrors (see figure 3.11). The gating time for the generation of a three fold coincidence is 8ns.

The 1.1° subtended by each of the photo-tubes optimizes the amount of Čerenkov light collected from an air shower compared to the background night sky (Patterson and Hillas 1989).

In September of 1992 a camera system was installed on the central mirror of the Woomera telescope. The camera consists of 37 pixels, each pixel being a 13mm by 13mm square Hamamatsu R4275 photomultiplier (see figure 3.12). The photocathodes of the camera tubes subtend 0.15° and the centers of the tubes are separated by 0.3° giving a total camera aperture of 2.5°. The camera is surrounded by a ring of eight 51mm diameter Hamamatsu R4275 photomultipliers on a ring of radius 2.2° centered on the middle of the camera.

In addition to the triplet detectors on the outer mirrors, the Woomera telescope can also be run with single three inch photomultipliers on these mirrors (see figure 3.11). In this mode the three inch tubes are run in fast triple coincidence with the inner 30 camera pixels. This detector configuration makes it possible to record the pulse profiles of events that trigger the system (see chapter 4).

The Woomera telescope is on an alt-azimuth mount and has a pointing accuracy of 0.1°. Event times are recorded from a rubidium clock with a relative precision of one micro-second and absolute accuracy of less than a milli-second.

3.3.2 Energy Threshold of BIGRAT

The estimation of energy threshold for an air Čerenkov telescope is notoriously difficult. In the case of BIGRAT the threshold is determined by the interaction of over 40 photo-tubes, and the characteristics of each tube are not known exactly.

By definition the energy threshold is the lowest energy primary capable of producing sufficient Čerenkov light to trigger the telescope. The energy threshold is

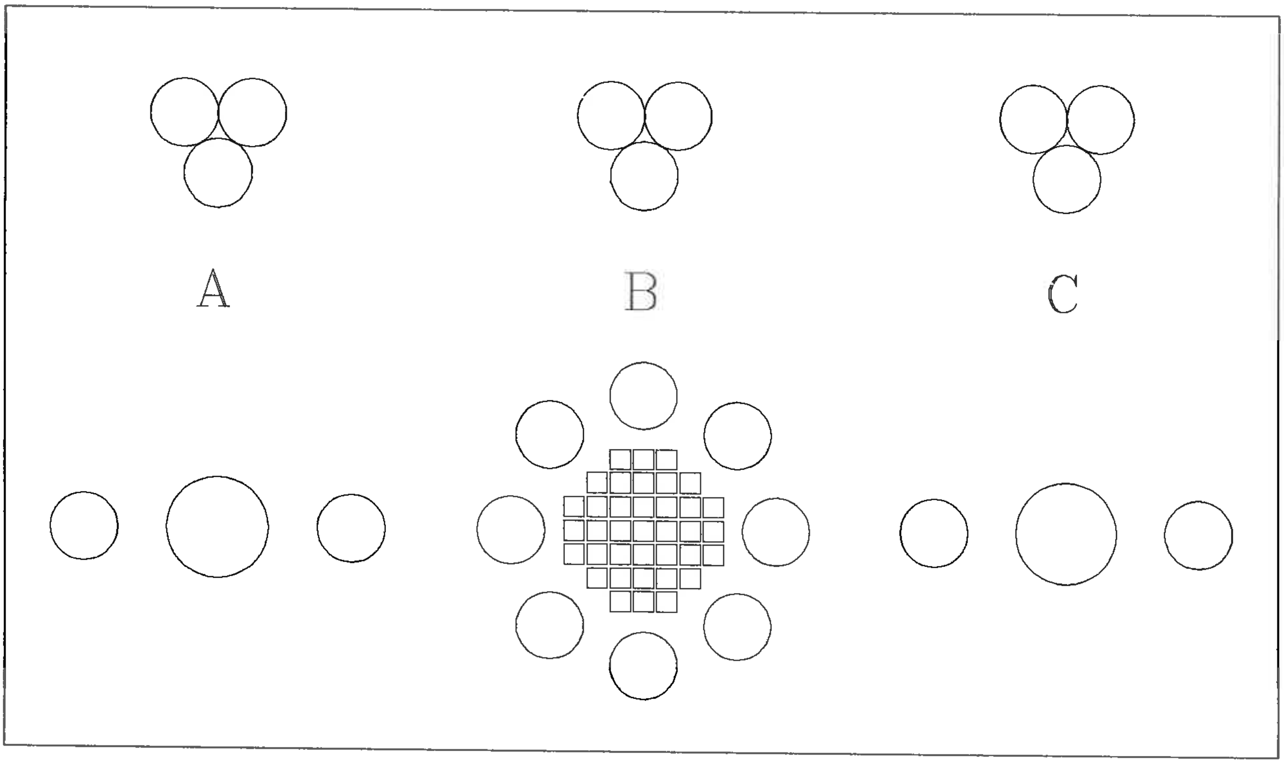

Figure 3.11: The two detector configurations for the Woomera telescope. The outer triggering detectors are either triplets of two inch photo-tubes (top), or single three inch tubes (bottom).

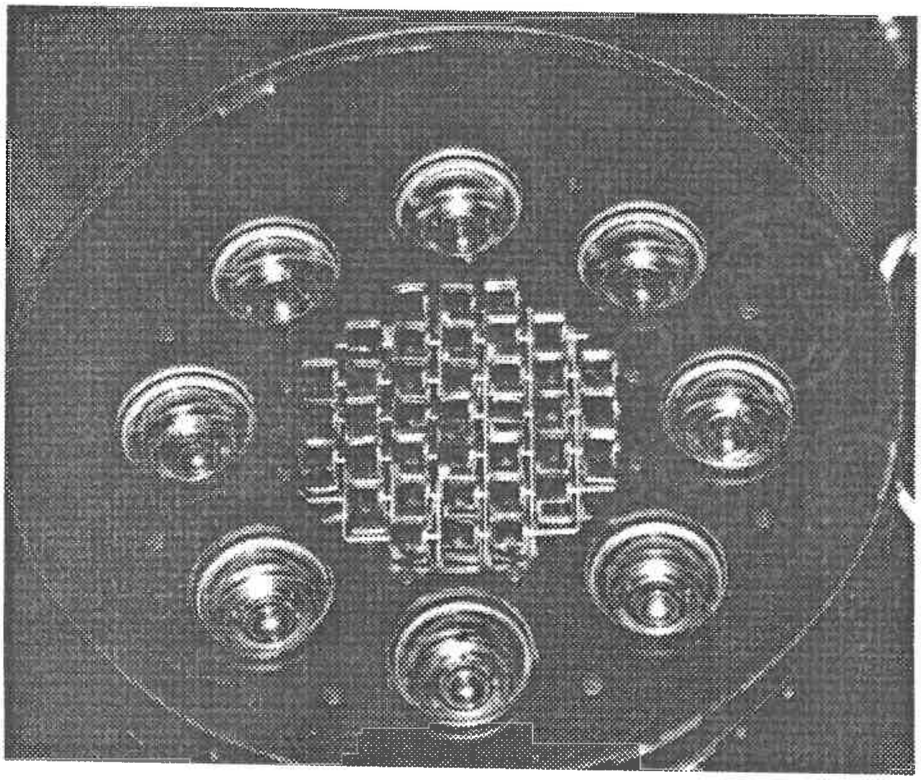

Figure 3.12: The camera system for the Woomera telescope

dependent upon the type of primary particle and the zenith angle of the observation. Following Weekes (1976) we define a quantity called the effective energy threshold. The effective threshold at a particular zenith angle for a given primary particle is the maximum of $\varepsilon(E)A(E)E^{-\gamma}$ where $\varepsilon(E)$ is the triggering efficiency, $A(E)$ is the energy dependent collecting area and $N(>E) \propto E^{-\gamma}$ is the source spectrum. The effective energy threshold is a convenient and easily identified quantity and is usually only a factor of two or three higher than the actual energy threshold.

For BIGRAT the energy threshold is calculated by comparing Monte Carlo models of the triggering rate of the telescope to the observed event rate. The Monte Carlo program used is MOCCA (MOnte Carlo CAscade), written by Michael Hillas (see e.g Hillas 1982). A complete description of the BIGRAT telescope is specified in the MOCCA program, including mirror setup and detector configuration. EAS are generated at core locations around the telescope out to a limiting radius R_{limit}, with this radius set just beyond the distance at which EAS will trigger the system. Gamma-ray primaries are assigned to come from the pointing direction of the telescope. The cosmic ray directions are assigned randomly within the field of view out to an angle θ_{limit}, such that beyond θ_{limit} no cosmic ray events trigger the system. The cosmic rays are selected from the known integral cosmic ray spectrum (power law exponent -1.65). The gamma-ray spectrum must be selected, and is usually set to the spectrum of a particular source that is of interest. The rate of cosmic ray primaries that will arrive in the solid angle Ω_{limit} defined by θ_{limit}, and area A_{limit} defined by R_{limit} is given by

$$R(>E) = 0.17 \left(\frac{E}{1\mathrm{TeV}}\right)^{-1.65} \mathrm{s}^{-1}\mathrm{m}^{-2}\mathrm{sr}^{-1} \tag{3.18}$$

where E is the minimum energy of primary particle generated by the Monte Carlo program, and is set below the expected threshold of the telescope. The simulated cosmic ray events will show the number of photoelectrons seen by the photo-tubes of the telescope. The coincidence conditions that exist between the tubes in the detector system must then be applied to each event to see if it will trigger the system. The photoelectron threshold of each photo-tube discriminator is adjusted until the rate of triggering of Monte Carlo events is equal to the measured triggering rate of the telescope. The same coincidence conditions and discrimination levels for the photo-tubes can then be applied to the gamma-ray Monte Carlo events to find the gamma-ray threshold of the telescope. The energy spectrum of Monte Carlo events that trigger the system, and therefore the effective energy threshold of the telescope, can then be found. Figure 3.13 shows the energy distribution of gamma-ray primary and proton primary events that trigger BIGRAT at zenith. In this simulation the detectors on the outer mirrors are single three inch photo-tubes, with the camera on the central mirror (see section 3.3.1 and figure 3.11).

It is known from independent measurements that the photoelectron threshold of the outer three inch tubes is about 20 photoelectrons, much higher than for the camera tubes. In the simulation program the triggering threshold of the outer tubes was held constant at this level and the threshold of the camera tubes was varied to produce the observed triggering rate. It was found that the triggering level of the camera tubes was 6-7 photoelectrons. From figure 3.13 it can be seen that the effective threshold of BIGRAT for gamma-rays primaries is about 800GeV, and about 1.2TeV for proton primaries. The threshold of cosmic ray EAS is higher because they are less efficient at producing Čerenkov light. Unlike a gamma-ray cascade, not all of the primary energy of a cosmic ray is transferred into the electromagnetic component (Turver and Weekes 1978). This estimate of effective threshold is not expected to be particularly accurate. The modeling of the detector does not allow for the response of each photo-tube, but rather treats the detector as a whole. The large amount of computer time needed to generate the Monte-Carlo cascades also leads to small numbers of events and hence a statistical uncertainty in the value of the threshold.

The collecting area of BIGRAT may also be found from the Monte Carlo simulations. Collecting area on its own is not a particularly useful parameter, as it is dependent upon the primary energy. It will be useful, however, to compare the collecting area for different zenith angles (see 3.4). Here we will make an arbitrary definition of collecting area as the area containing 90% of the showers that trigger the telescope. Figure 3.13 shows the core location distribution for gamma-ray and proton EAS that trigger the telescope. From this figure it can be seen that at zenith the collecting area for gamma-ray primaries is $6.6 \times 10^4 \mathrm{m}^2$, and $9.1 \times 10^4 \mathrm{m}^2$ for

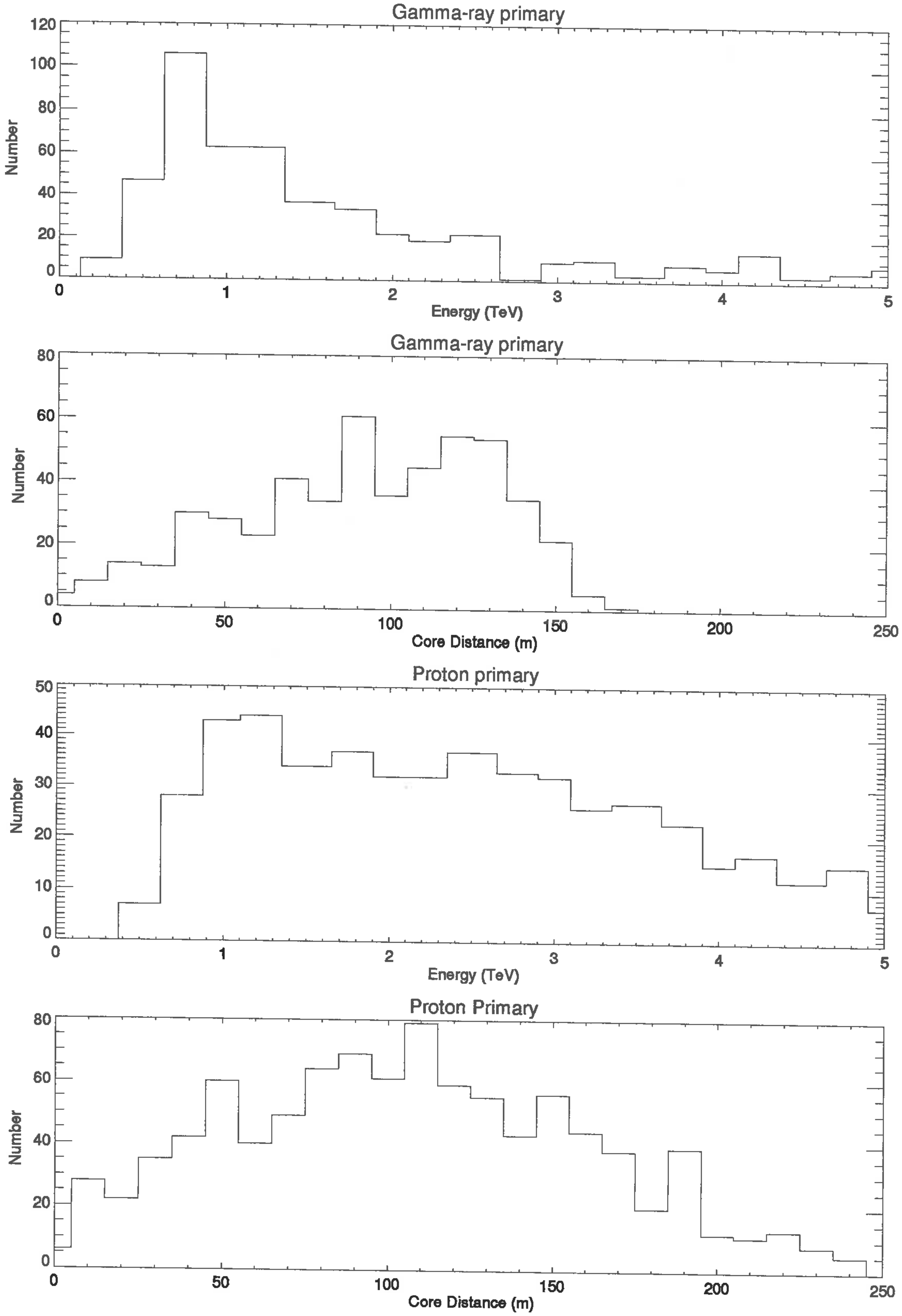

Figure 3.13: The energy and core location distributions of Monte Carlo gamma-ray and proton primary EAS that trigger BIGRAT at zenith.

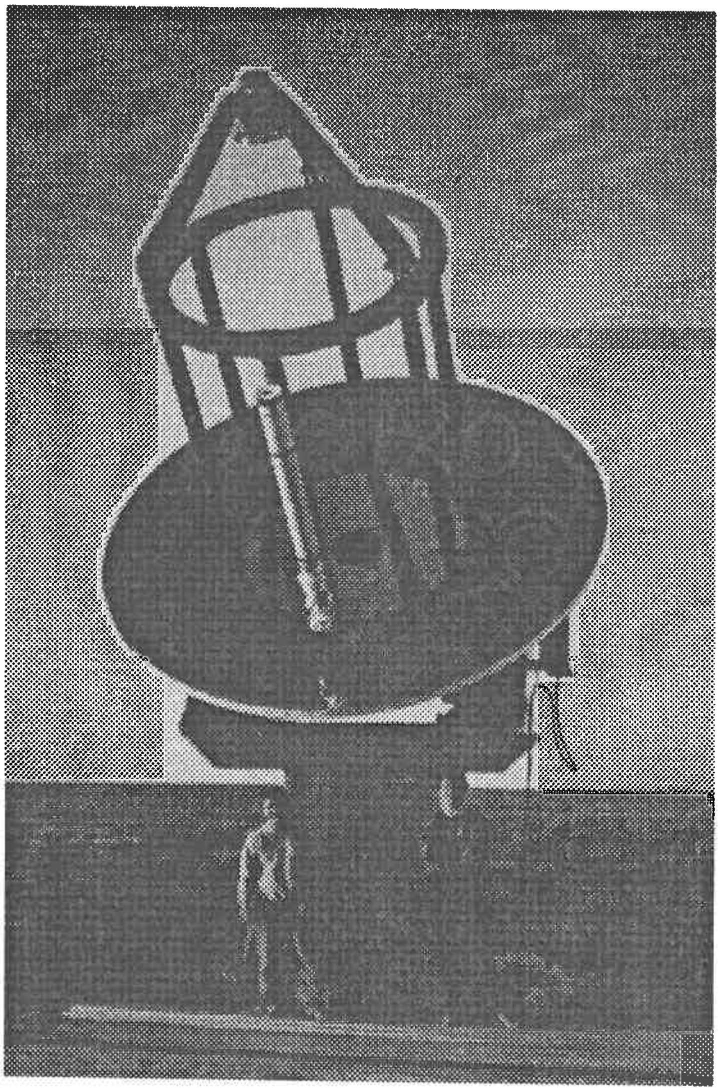

Figure 3.14: Dodaira Telescope

proton primaries.

3.3.3 CANGAROO

In February 1991 the Japanese Dodaira mirror was placed 100m to the east of the Woomera telescope so that stereo observations could be made of potential VHE gamma-ray sources. The CANGAROO (Collaboration between Australia and Nippon for a GAmma-Ray Observations in the Outback) project uses camera systems on both the Dodaira and BIGRAT telescopes to simultaneously observe Čerenkov images. The Dodaira mirror has a diameter of 3.8m and it was previously used for lunar ranging and has much better angular resolution than traditional air

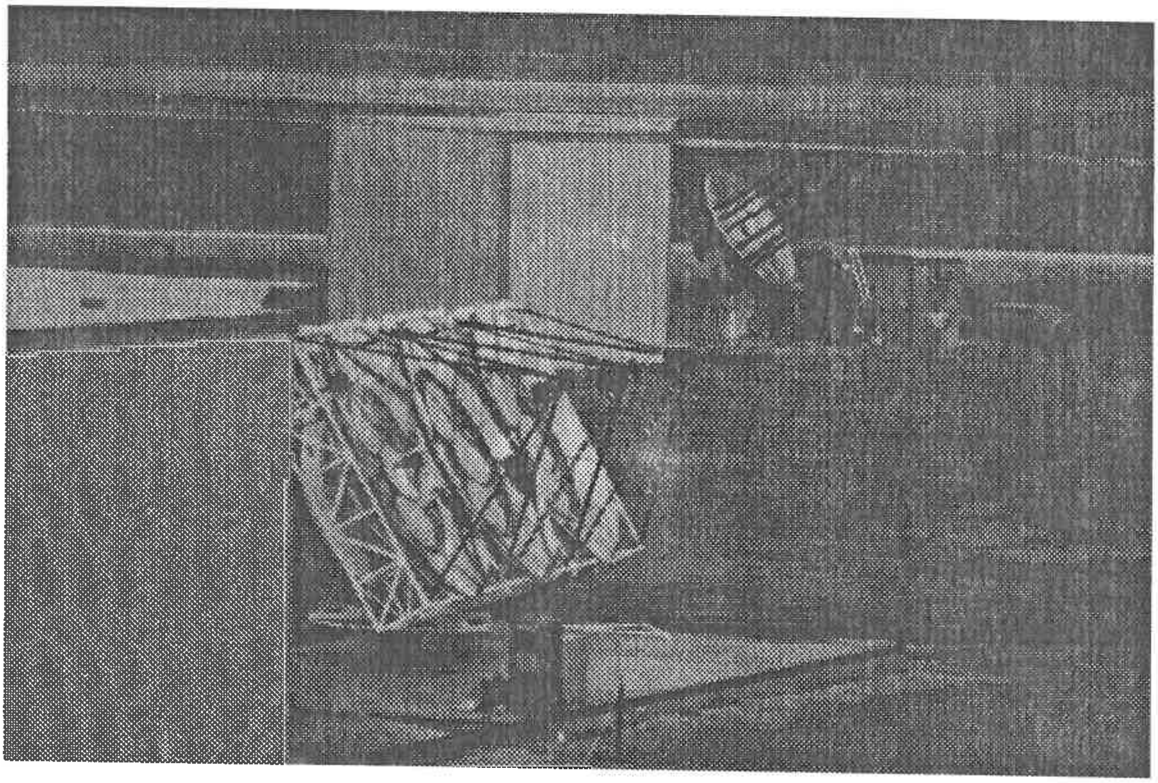

Figure 3.15: CANGAROO- Dodaira and BIGRAT

Čerenkov mirrors. To take advantage of the excellent mirror surface the camera has been constructed of square 10mm by 10mm tubes (Hamamatsu R2248). Initially 220 tubes will be used giving a total field of view of 2.7°. The triggering of the camera and other details of the system have been described elsewhere (Hara et al. 1993, Kifune et al. 1993). For each coincidence detected by the Dodaira or BIGRAT telescopes a $4\mu s$ wide signal is sent to the other telescope. Events which trigger both systems are flagged for future stereo analysis.

The gamma-ray threshold of the Dodaira telescope is estimated to be approximately 1TeV and the vertical triggering rate is about 1Hz. Early stereo observations indicate that the stereo rate between the Dodaira mirror and BIGRAT is about 10-15% of the BIGRAT triggering rate.

3.4 Sommers-Elbert Technique

The conventional method of operating an air Čerenkov telescope is to look at sources that are within 45° of zenith. This keeps the energy threshold of the telescope as low as possible, which is an advantage for most VHE gamma-ray sources which have spectra that are softer than the background cosmic ray spectrum.

Sommers and Elbert (1987) have proposed an alternate observing scheme, in which observations for hard spectra sources are done at extremely large zenith angles. The advantage of large zenith angle observations is an increase in the collecting area of an air Čerenkov telescope. As the zenith angle of observation increases the distance between the point of observation and shower maximum increases. For Čerenkov light from EAS, which has a typical half angle spread of $\sim 1°$, the increased distance to shower maximum causes the light to spread over a much larger area at the observation level. Clearly this will also lead to an increase in the threshold of an air Čerenkov telescope because the greater spreading of the Čerenkov light will give a decreased photon density. Large zenith angle observations allow for the study of gamma-rays over a large range of energies, and also increases the number of sources that can be studied from an observation site.

Sommers and Elbert derive a rough equation for calculating the distance, D, between observation and shower maximum (X_{max}) for a particular zenith angle θ

$$D = \left(7.1 \ln\left(\frac{1030}{X_{max} cos\theta}\right) - H\right) \sec\theta \tag{3.19}$$

where H is the height of observation above sea-level. The atmosphere is assumed to be isothermal and atmospheric depth (X) is calculated by

$$\mathrm{X} = 1030 \exp\left(\frac{-\mathrm{h}}{7.1\mathrm{km}}\right) \mathrm{gcm}^{-2} \tag{3.20}$$

and X_{max} is described by

$$\mathrm{X}_{max} = 36 \ln\left(\frac{E}{74\mathrm{MeV}}\right) \mathrm{gcm}^{-2} \tag{3.21}$$

Using a simple geometrical model, where the Čerenkov light from EAS is assumed to be beamed uniformly over a half angle of $\delta \sim 1°$, the variation of collection area A with zenith angle may be described by

$$A(\theta) = \pi(D(\theta)\tan^{-1}\delta)^2 \tag{3.22}$$

We may calculate the threshold energy $E_{thresh}(\theta)$ at a zenith angle θ by assuming that there are no transmission losses in the atmosphere for Čerenkov light, and that the number of Čerenkov photons produced is proportional to primary energy:

$$E_{thresh}(\theta) = \frac{E_{thresh}(0)A(\theta)}{A(0)} \tag{3.23}$$

where $E_{thresh}(0)$ and $A(0)$ are the energy threshold and collecting area at zenith.

To get a more accurate estimate of the variation in collecting area and energy threshold with zenith angle it is necessary to do Monte Carlo simulations. These were done by the author using the program and methods described previously (see section 3.3.1). Figure 3.16 shows the change in energy threshold and collecting area of BIGRAT with zenith angle for both gamma-ray and proton primaries.

It is possible to estimate how hard a gamma-ray source spectrum must be in order that the signal to noise ratio at a zenith angle θ be the same as at vertical.

$$\frac{S}{N}(\text{vertical}) = \frac{S}{N}(\text{zenith} = \theta) \tag{3.24}$$

where

$$\begin{aligned}
S_v &\propto (E_g^v)^{-\beta} A_g^v \\
N_v &\propto ((E_c^v)^{-\gamma} A_c^v)^{\frac{1}{2}} \\
S_\theta &\propto (E_g^\theta)^{-\beta} A_g^\theta \\
N_\theta &\propto ((E_c^\theta)^{-\gamma} A_c^\theta)^{\frac{1}{2}}
\end{aligned} \tag{3.25}$$

E_g^v and E_c^v are the threshold energies of the telescope for gamma-rays and cosmic rays respectively for showers at zenith. E_g^θ and E_c^θ are the threshold energies at zenith angle θ. Using the same notation, A_g^v, A_c^v , A_g^θ and A_c^θ are the collecting areas for gamma-rays and cosmic rays vertically and at zenith angle θ. The parameter β is the integral gamma-ray source spectrum and γ is the integral cosmic ray spectrum, $\gamma = 1.65$. Putting equations 3.25 into 3.24 gives

$$\left(\frac{E_g^v}{E_g^\theta}\right)^{-\beta} = \frac{A_g^\theta}{A_g^v}\left(\frac{A_c^v}{A_c^\theta}\right)^{\frac{1}{2}}\left(\frac{E_c^v}{E_c^v}\right)^{-\frac{\gamma}{2}} \tag{3.26}$$

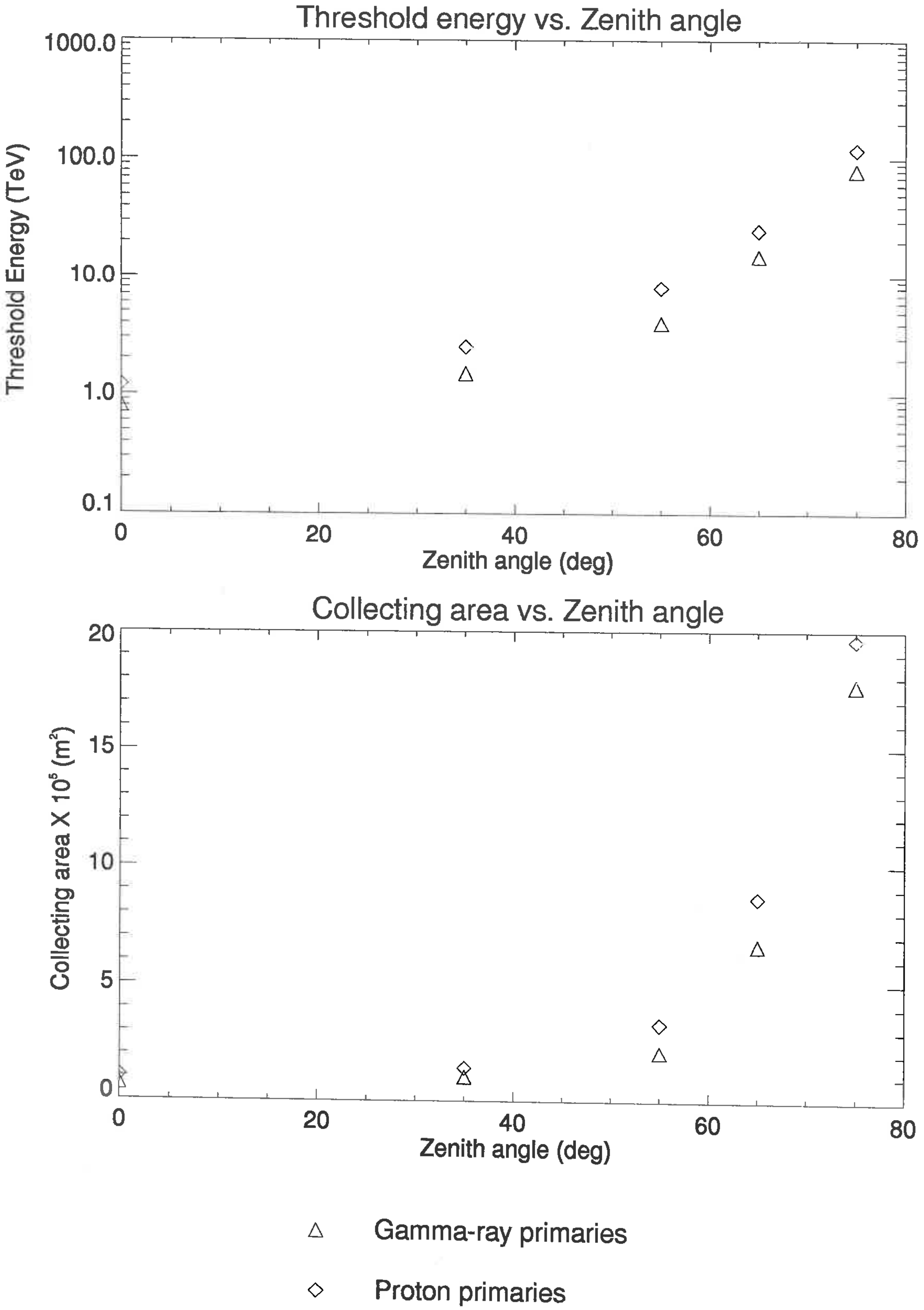

Figure 3.16: Change in threshold energy and collecting area of BIGRAT with zenith angle for gamma-ray and proton primary EAS.

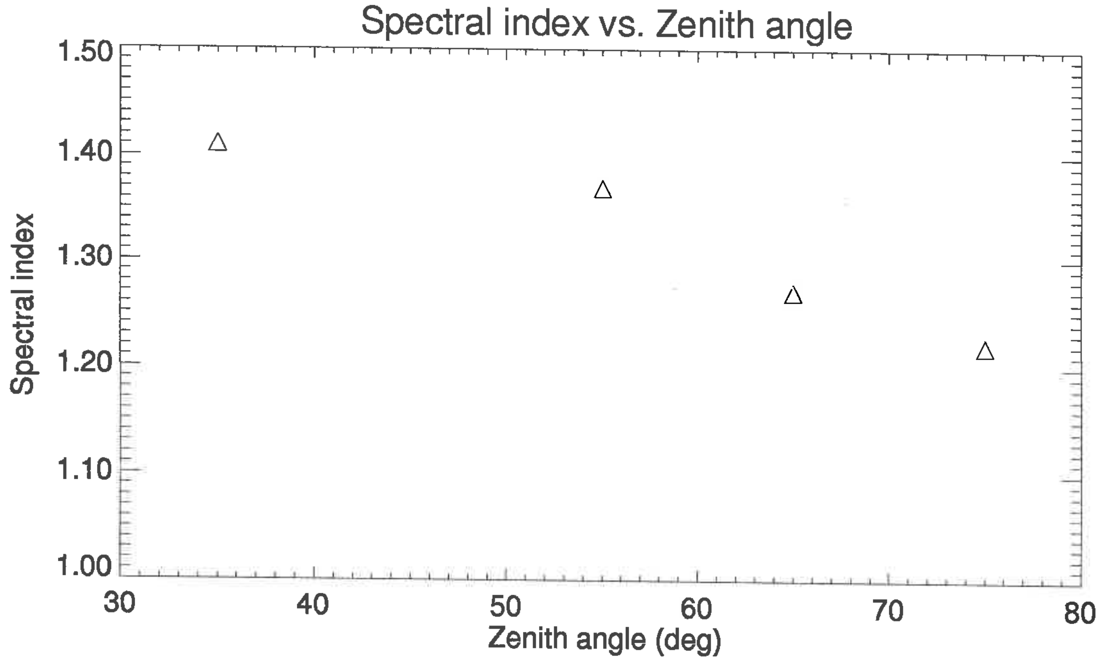

Figure 3.17: Integral gamma-ray spectral index needed at various zenith angles to maintain the same signal to noise as for vertical observation.

rearranging this for β

$$\beta = \ln\left[\frac{A_g^\theta}{A_g^v}\left(\frac{A_c^v}{A_c^\theta}\right)^{\frac{1}{2}}\left(\frac{E_c^\theta}{E_c^v}\right)^{\frac{\gamma}{2}}\right]\left[\ln\left(\frac{E_g^\theta}{E_g^v}\right)\right]^{-1} \tag{3.27}$$

Using the values of figure 3.16 it is possible to calculate values of β such that observing at a zenith angle θ gives the same signal to noise as observing at zenith (see figure 3.17).

Chapter 4

Background Rejection Techniques

It is now over four decades since the first studies of EAS through the atmospheric Čerenkov technique (Galbraith and Jelley 1953). Early calculations of the flux of VHE gamma-rays from the Crab Nebula (Cocconi 1959) and other supernova remnants predicted that these sources would be easily detectable. These early predictions were found to be optimistic, with measured VHE gamma-ray fluxes being orders of magnitude less than expected. Despite intensive effort since the first searches for VHE gamma-rays in the 1960s, progress until recently has been painfully slow. Researchers in this field have been frustrated by low fluxes, the sporadic and unpredictable nature of the sources and the presence of an overwhelming background signal due to EAS from cosmic rays.

In this chapter there will be a discussion of techniques for improving the gamma-ray flux sensitivity of air Čerenkov detectors. Firstly some general considerations will be discussed, including a brief mention of some methods of increasing flux sensitivity. This will be followed by a description of methods of rejecting cosmic ray events on the basis of the shape of the Čerenkov photon image.

4.1 Sensitivity Considerations

For a steady DC signal the sensitivity of a gamma-ray telescope may be described by the number of standard deviations, n_σ, at which the signal is detected. For a source with an integral spectrum described by $F_\gamma(> E_\gamma) = k_\gamma E_\gamma^{-\alpha}$, with a background cosmic ray spectrum $F_{cr}(> E_{cr}) = k_{cr} E_{cr}^{-\beta}$, n_σ is given by

$$n_\sigma = \frac{k_\gamma E_\gamma^{-\alpha} t A_\gamma}{\sqrt{k_{cr} E_{cr}^{-\beta} t A_{cr} \Omega}} \tag{4.1}$$

where A_γ and A_{cr} are the respective collecting areas for gamma-rays and cosmic rays and are assumed to be energy independent. Ω is the effective solid angle of the detector and t is the observing time. From equation 4.1 there are a number of obvious ways to increase the flux sensitivity of an air Čerenkov telescope and these will now be discussed.

4.1.1 Increasing Observing Time

For a steady DC source the significance of a detection will increase as $\sqrt{t}$. For an air Čerenkov telescope the amount of time available for observing a source is quite limited. For most observers a particular source will be visible for only a few months of the year, and observations during this period will be limited to new moon periods with favorable weather conditions.

If a source exhibits transient behavior then analyzing data over too large a time span will tend to wash out the signal. For a pulsed signal the significance will also increase with observation time if the signal remains phase coherent.

4.1.2 Decreasing Energy Threshold

As previously discussed in section 3.3.2 the Čerenkov photon density for a gamma-ray EAS is about twice that of a cosmic ray EAS of the same energy. Assuming that the Čerenkov photon density scales linearly with primary energy, equation 4.1 may be written as

$$n_\sigma \propto E_\gamma^{-(\alpha - \frac{\beta}{2})} A_\gamma \sqrt{\frac{t}{2^{-\beta} A_{cr} \Omega}} \tag{4.2}$$

From equation 4.2 it can be seen that the flux sensitivity will increase with decreasing energy threshold if $\alpha > \beta/2$. Patterson and Hillas (1989) have also shown that decreasing the energy threshold of an air Čerenkov telescope can lead to significant improvement in flux sensitivity for sources with steeply falling power law spectra.

4.1.3 Increasing Collecting Area

The flux sensitivity may be increased by increasing the effective collecting area of an air Čerenkov detector. Cawley (1988) and Patterson and Hillas (1989) have proposed that this may be achieved by using a number of widely spaced Čerenkov detectors. If the collecting areas of the detectors do not overlap then for N detectors the flux sensitivity increases as $\sqrt{\mathrm{N}}$.

4.1.4 Decreasing the FOV (Ω)

From equation 4.1 it can be seen that the flux sensitivity will vary as $1/\sqrt{\Omega}$ for large Ω. For most air Čerenkov telescopes the lowest value of Ω is limited by the angular size of gamma-ray Čerenkov image.

One way of decreasing Ω is to use fast timing of the Čerenkov light front. Most of the Čerenkov emission from an EAS comes from shower maximum, producing a thin "pancake" of light that is only several nano-seconds thick. By timing the passage of the light front at several points it possible to determine the arrival direction of an incident primary particle to a greater accuracy than the FOV of the detector. This allows primary particles that lie outside the cone of acceptance to be rejected. For accurate reconstruction of the direction of the light front, detectors must be widely spaced (typically tens of meters apart). Since the mirrors must be in coincidence with each other this method can lead to high energy thresholds. This technique is mostly used for experiments with solar collectors, which have only crude focusing.

The method of fast timing the Čerenkov light front was first used by Tornabene and Cusimano (1968) and further developed by Gibson et al. (1982) and Gupta et al.

(1982). The French experiment THEMISTOCLE (Kovacs 1990) with a threshold energy of 3 TeV has recently seen a DC gamma-ray signal from the Crab Nebula (Baillon et al. 1991) using the method of fast timing the Čerenkov light front.

The most promising methods for increasing the flux sensitivity of VHE gamma-ray telescopes exploit the differences between gamma-ray and cosmic ray EAS to reject the cosmic ray background. An early example of this is the "double beam technique". It was noticed that for two widely separated narrow beam Čerenkov telescopes operated in coincidence the event rate could be increased by tilting the optical axes of the telescopes toward each other (Hanbury-Brown et al. 1969, Tornabene and Cusimano 1968). The increased sensitivity was attributed to the fact that the optical axis of each telescope now pointed toward the position of shower maximum. It was subsequently found by Grindlay (1971) that beneath shower maximum there was a second angular maximum that appeared to be rich in ultra-violet light. Grindlay interpreted this second maximum as being due to Čerenkov emission from the penetrating muon component of nucleon induced EAS. By rejecting showers which have this second angular maximum it should be possible to discard a substantial number of background cosmic ray showers. One drawback of this method is that it is limited to primary energies above 1TeV, where the penetrating muon component is large enough to be detected.

Another method of increasing gamma-ray flux sensitivity is to reject cosmic ray events on the basis of their Čerenkov lateral distributions. Figure 3.3 showed how the cosmic ray Čerenkov lateral distribution has localized peaks due mainly to penetrating muons. In principle a distributed array of mirrors would be able to detect the differences between gamma-ray and cosmic ray Čerenkov lateral distributions. An extreme example of this is the SOLAR 1 proposal (Tümer et al. 1990), which would use the mirrors of a large solar array to capture a large number of the photons from each EAS.

4.2 Camera Systems

In section 3.2.2 we discussed the the formation of Čerenkov images in terms of the angular distribution of Čerenkov light emitted from EAS. It was shown that EAS at non-zero core locations will form approximately elliptical images in the field of view of an air Čerenkov telescope. It was expected that the size and shape of these images, to some extent, would reflect the longitudinal and lateral development of the EAS that produced them.

In 1985 Hillas made detailed Monte Carlo simulations of the images formed in a 37 pixel camera by EAS induced by different primary particles. It was found that the images formed by gamma-ray primaries and cosmic ray primaries were significantly different. The images due to cosmic ray primaries were found to be longer and fluctuated more than the images due to gamma-ray primaries (see figure 4.1). This is due to the extended development of cosmic ray EAS (see figure 4.2). Images due to cosmic ray primaries were also found to be wider, reflecting the wider lateral distribution of cosmic ray initiated EAS. The major axes of the gamma-ray images were found to point toward the position of the source in the field of view, while cosmic ray images generally did not, reflecting the isotropic arrival directions of the cosmic rays. Figure 4.1 shows some examples of images generated by Monte Carlo shower simulation.

By exploiting the shape of Čerenkov images it is possible to greatly increase the flux sensitivity of an air Čerenkov telescope. For the simplest VHE gamma-ray telescope, a mirror viewed by a single on-axis photo-tube, the shape of the Čerenkov images will determine the optimum field of view. Patterson and Hillas (1989) have shown that by using a number of smaller tubes rather than a large single tube, it is possible to trigger more efficiently from the smaller gamma-ray images. The following sections will describe some detector configurations that use the shape of Čerenkov images to enhance the gamma-ray sensitivity of VHE observations.

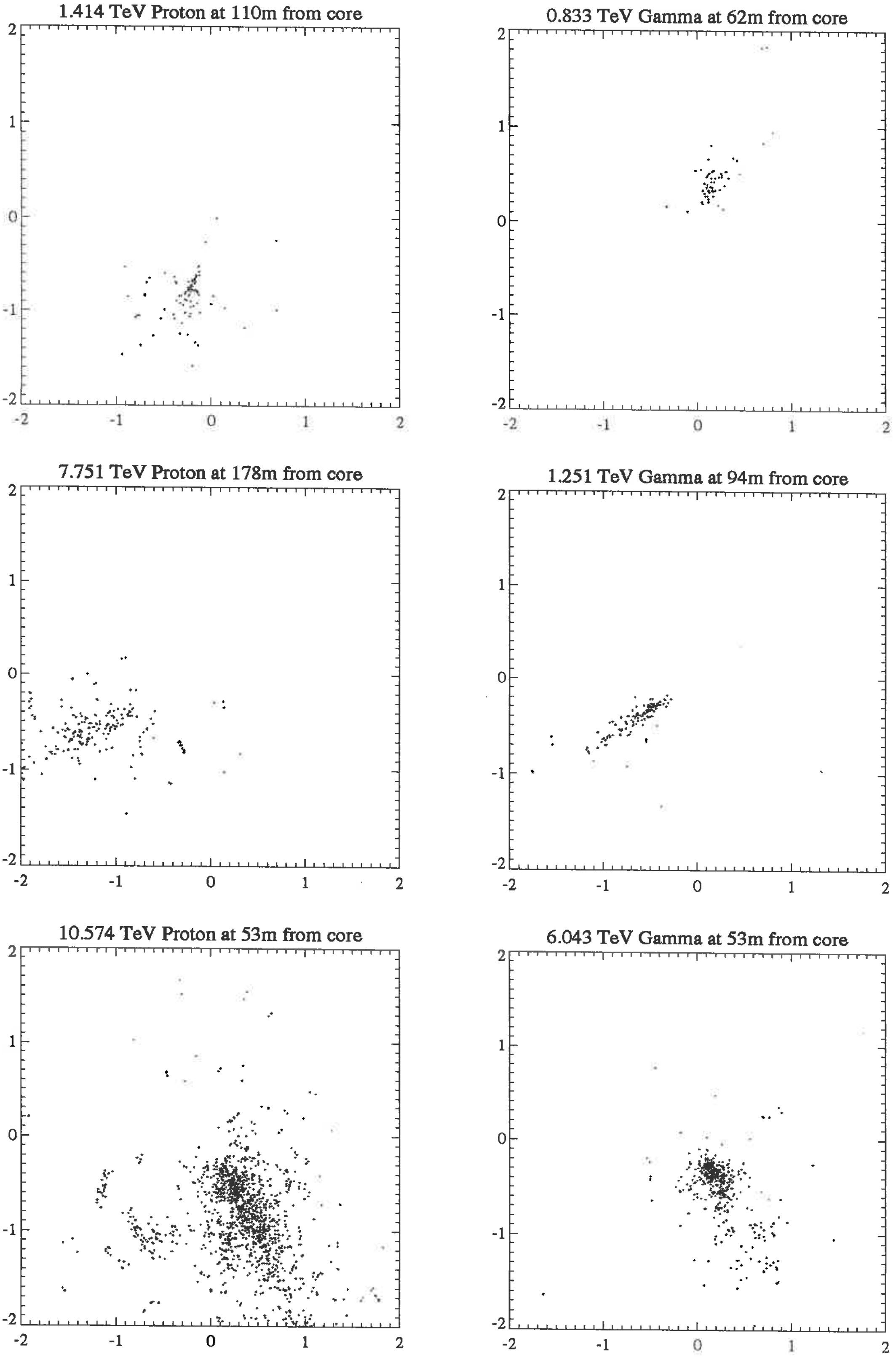
1.414 TeV Proton at 110m from core

0.833 TeV Gamma at 62m from core

7.751 TeV Proton at 178m from core

1.251 TeV Gamma at 94m from core

10.574 TeV Proton at 53m from core

6.043 TeV Gamma at 53m from core

Figure 4.1: Monte Carlo simulation of Čerenkov images from gamma-ray and proton EAS . Each point represents a photoelectron in the field of view. The scale of each plot is in degrees. These images were generated by the Monte Carlo simulation program MOCCA.

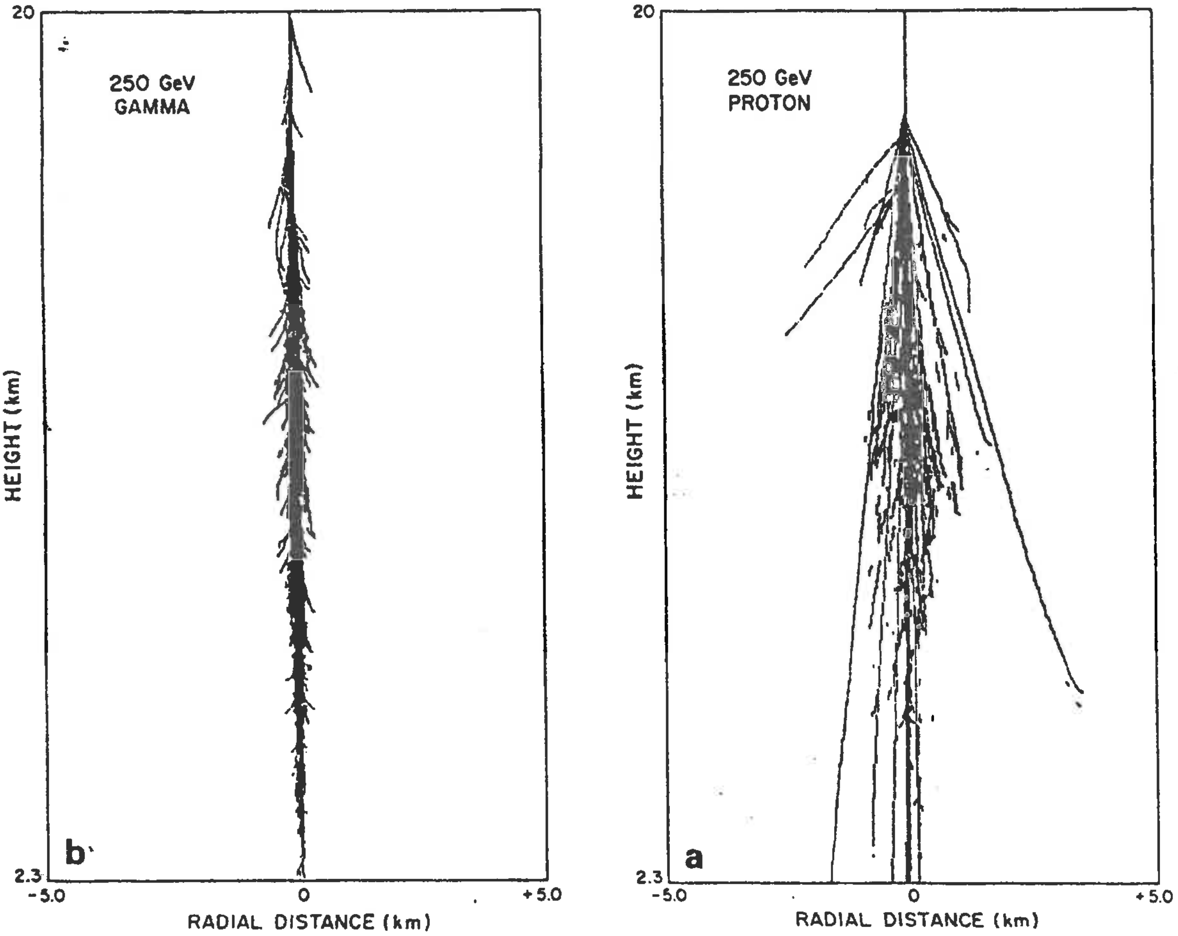

Figure 4.2: Monte Carlo simulation of the development of gamma-ray and proton initiated EAS (from Weekes 1992)

4.2.1 Guard Ring

The guard ring technique has been devised empirically by the Durham group for telescopes now operating at Narrabri in Australia (Brazier et al. 1990). The telescopes consist of three mirrors of 11 m^2, each viewed by a detector package which contains 7 phototubes subtending approximately one degree each. One tube is on axis while the other six are on a 2° circle around it, forming a "guard ring".

Events that trigger the system are divided into three categories, A, B or C. If the majority of the signal falls in only the central tube of the detector, then the event is classed as category A. If the signal is split between the central tube and the guard ring, then it is classed as category B, and if the signal falls mainly in the guard ring it is classed as category C.

It is expected that gamma-ray signals will produce events that are mainly in category A. Most gamma-ray images fall within 1° of the center of field of view, and, because the gamma-ray images are compact, the image should not extend out to the guard ring. For cosmic ray images, which are wider and longer, there is a good chance that part of the image will fall into the guard ring. Events which fall only into the guard ring are assumed to be from off-source cosmic rays. By selecting only category A events, Brazier et al.(1990) claim to reject around 50% of the cosmic ray background while retaining the majority of the gamma-ray signal.

4.2.2 Whipple Camera System

In 1983 a medium resolution camera was installed on the Whipple observatory 10m gamma-ray telescope at Mount Hopkins . The camera consisted of thirty seven 5cm diameter photo-tubes arranged in a hexagonal array. The tube centers were separated by 0.5° giving a total field of view of 3.5°.

The image analysis used for this medium resolution camera is described by Hillas (1985). Hillas parameterizes each image as an ellipse, and defines a number of parameters that describe the size, position and orientation of the image. The parameters used (see figure 4.3) in the original Hillas paper are :

- Length - the RMS length of the major axis of the image. The length of the image is sensitive to the longitudinal development of the shower.
- Width - the RMS length of the minor axis of the image. Width is sensitive to the lateral spread of the shower.
- Miss - the perpendicular distance between the major axis and the center of field of view. The miss parameter is a measure of image orientation and is sensitive to the arrival direction of the primary particle.
- Distance - the distance from the center of field of view to the centroid of the image.
- Azwidth (azimuthal width) - RMS width of the image perpendicular to a line joining the center of field of view and the image centroid. The azwidth

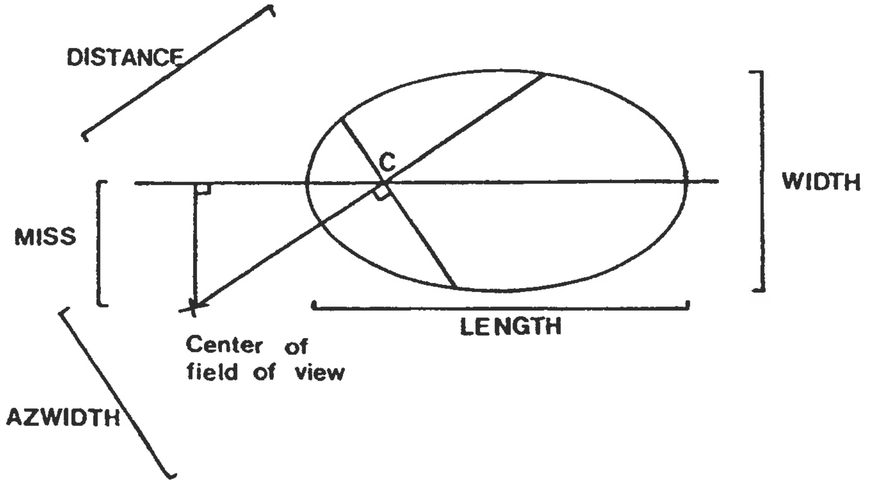

Figure 4.3: Image parameterization. The centroid of the image is marked by C. (from Weekes et al. 1989)

parameter depends upon both the orientation of the image and its width. Azwidth will be smallest for narrow images pointing toward the center of field of view (gamma-ray images).

- Concentration - the ratio of the two largest tube signals to the total tube signal.

The face of the camera is divided into four zones. Zone 0 is the central tube, zones 1, 2 and 3 are formed by the concentric rings of the tubes in the camera. Images that fall mainly in zone 0 are close to circular and cannot be parameterized. Images that fall mostly in zone 3 are also not analyzed as an unknown amount of the image lies outside the field of view of the camera.

Using a Monte Carlo simulation Hillas (1985) calculated the distributions of image parameters for gamma-ray and cosmic ray EAS (see figure 4.4). These simulations show that even with a crude camera system it should be possible to identify gamma-ray and cosmic ray events based on their image parameters. Hillas defined "gamma domains" for each image parameter in which most of the gamma-ray images, but few cosmic ray images lay (see table 4.1).

Hillas' simulations indicate that the Azwidth parameter, which is sensitive to both the shape and the orientation of the image, is the best single cut. Hillas suggests that a mixture of cuts may give the best sensitivity, although it should be

Parameter	Zone 1	Zone 2
width (°)	<0.21 - 0.17x	< 0.19 - 0.20x
length (°)	<0.35 - 0.13x	< 0.33 - 0.13x
miss (°)	<0.17	< 0.22
distance (°)	>0.65	> 0.83 + 0.04x
conc	>0.72 + 0.28x	> 0.72 + 0.31x
azwidth (°)	<0.21 - 0.11x	< 0.20 - 0.11x

Table 4.1: The gamma-ray domains for each of the image parameters. From Hillas(1985) where x=sec(θ)-1 and θ=zenith ang.

noted that the image parameters are not independent of each other.

To describe how well the image cuts work the Whipple group define a quality factor, q, given by

$$q = \frac{N_a^\gamma}{N_T^\gamma}\left(\frac{N_a^{cr}}{N_T^{cr}}\right)^{-\frac{1}{2}} \tag{4.3}$$

where N_a^γ is the number of gamma-rays passing the image cuts from a total of N_T^γ gamma-rays, and N_a^{cr} is the number of cosmic rays accepted from a total of N_T^{cr} cosmic rays. Hillas predicted that the imaging technique with the medium resolution camera should reject 98-99% of the cosmic ray background while keeping 60-70% of the gamma-ray signal.

The value of the imaging technique has been proved on observations of the Crab Nebula (Weekes et al. 1989). During the period December 1986 to February 1988 a steady flux of gamma-rays of energy >0.7 TeV was seen at a significance of 9σ. Both the background image parameter distributions and the amount of signal enhancement were consistent with the predictions of Hillas. As expected the image selection process was able to reject about 98% of cosmic ray background events and gave a quality factor of ~ 4.

Following the success of the medium resolution camera the Whipple group have constructed a camera of higher resolution (Cawley et al. 1990). The new camera consists of 91 pixels of width 0.21° surrounded by "guard ring" of eighteen 0.5° tubes (see figure 4.5). Using the high resolution camera the Crab Nebula was observed (Vacanti et al. 1991) between November 1988 and March 1989. After image cuts

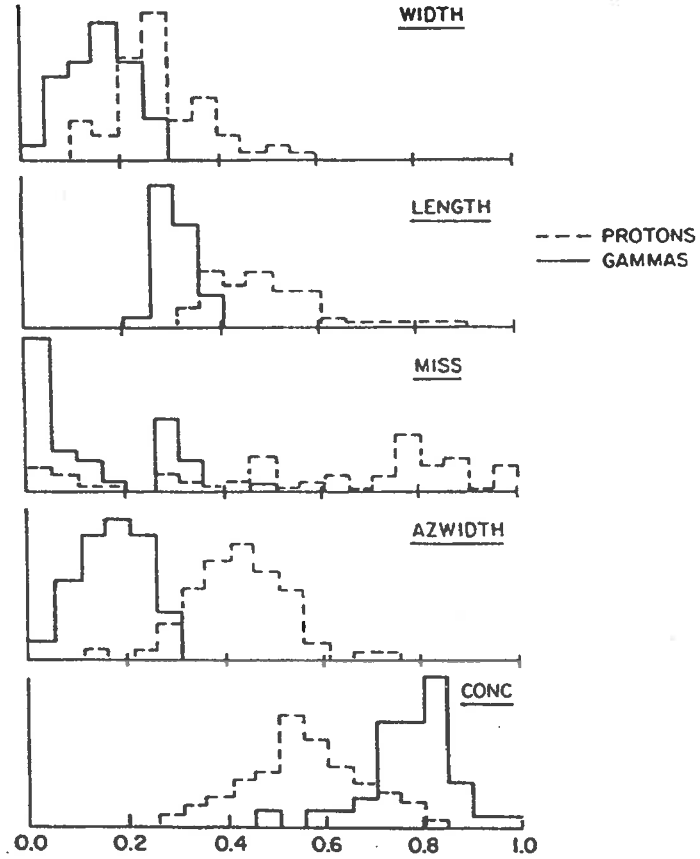

Figure 4.4: Image parameter distributions (from Weekes et al. 1989).

these observations yielded a steady DC emission of gamma-rays at a significance of 20σ. This indicates an increase in sensitivity over the medium resolution camera of a factor of 2.5, giving a total quality factor of ~ 10.

With a signal containing such a large percentage of gamma-rays the Whipple group have been able to optimize their image analysis on the Crab data (Punch et al. 1991). These new "supercuts" were derived by optimizing the image parameter domains on the 1988-1989 data set. In addition to this, more sophisticated techniques for treating ADC pedestal and noise subtraction were implemented. By using supercuts the significance of the 1988-1989 data set was increased to 34σ, indicating an increase in sensitivity of 1.75 over the earlier high resolution image analysis. With this sensitivity it is possible to see the Crab Nebula at a significance of 4σ with just one hour of observation.

Using the supercuts analysis on the high resolution camera, the Whipple group have performed a search for DC emission of VHE gamma-rays from a total of 27

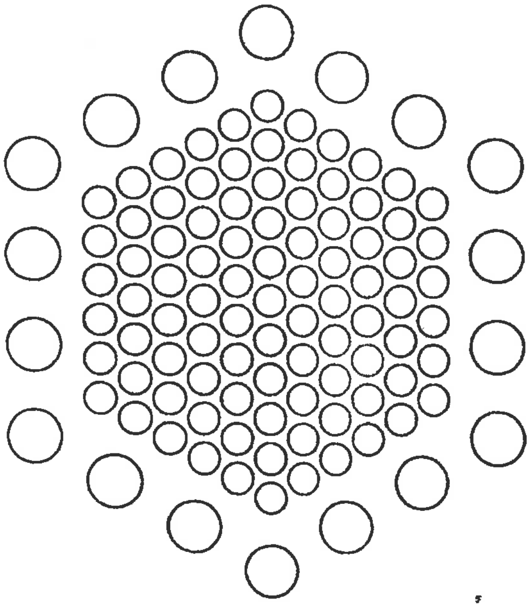

Figure 4.5: Photo-tube layout of the Whipple high resolution camera. (from Reynolds et al. 1993).

sources (Reynolds et al. 1993). It is disappointing to note that despite the unprecedented sensitivity of the Whipple telescope, no significant emission was seen from any source other than the Crab. More recently, however, steady DC emission of gamma-rays has been seen from the giant elliptical galaxy Markarian 421 at a significance of 6σ (Punch et al. 1992).

To further enhance the sensitivity of the imaging technique a second 10m class reflector is being built 120m from the original Whipple telescope (Akerlof et al. 1990). The new telescope, called "GRANITE", will be equipped with a 109 pixel camera to allow stereo viewing of EAS in conjunction with the Whipple high resolution camera. It is predicted that the sensitivity of the new stereo system will be an order of magnitude better than the original high resolution camera.

4.2.3 Woomera Camera System

The Woomera camera (described in section 3.3.1) was installed in the middle of 1992 and became fully operational in March 1993. The response of the Woomera camera to both gamma-rays and cosmic rays is being modeled using Hillas' MOCCA

Monte Carlo program.

The raw camera images are processed in a similar manner to that used by the Whipple collaboration. The ADC pedestal values are subtracted from the raw ADC value for each tube. These numbers are then weighted to allow for the different gains of the tubes. Gain calibration is done using a flash calibrator consisting of 7 LED's driven by a fast rise-time pulse. Finally the image is "cleaned", removing spurious noise that may affect the parameterization of the image.

In addition to the parameters described in Hillas (1985), two other parameters are used: alpha and concentration1. Alpha is the angle between the major axis of the image and the line joining the center of field of view and the image centroid. Alpha has a range of 0° to 90°, and for gamma-ray images alpha is expected to be small. Concentration1 is the percentage of the total signal that falls in the tube containing the largest signal.

Chapter 5

Pulse Shape Measurement Technique

5.1 Introduction

In late 1989 the Woomera group began planning to install a camera system on one of the mirrors of the BIGRAT telescope . At this time the Woomera group was using the Sommers-Elbert large zenith angle observation technique (see section 3.4) to observe northern hemisphere sources(Gregory et al. 1990) . The conventional view of camera systems was that they would not work well for large zenith angle observations. The increased distance to shower maximum for highly inclined showers leads to a smaller image size which reduces the efficiency of the image cuts (Weekes et al. 1989). Observations of the Crab Nebula at large zenith angles seem to indicate that this is the case (Weekes 1991). For the Whipple camera the imaging technique works well above 50° elevation. For showers with elevation between 35° and 50° the imaging technique still works but with reduced efficiency. Beneath 35° the imaging technique does not seem to work at all. This creates a problem for the Woomera group as the northern sources of greatest interest (Crab Nebula, Her X-1, Cyg X-3) all culminate at or below 35° elevation as viewed from Woomera. With this in mind I was interested in developing a technique that could provide rejection of the background cosmic ray flux for highly inclined showers.

It seemed that such a technique could be realized by measuring the temporal distribution of the Čerenkov light from EAS. At this time there were indications that gamma-rays and cosmic rays could be distinguished on the basis of their pulse profiles (Tümer et al. 1990). It seemed likely that this method, unlike the imaging technique, would still work at large zenith angles. In fact it was hoped that with the larger energy and path lengths of the inclined showers that the technique might work better at large zenith angles than vertically. In addition to this, a pulse shape measurement system is relatively cheap and easy to install and is well suited to the type of mirrors used on the Woomera telescope which introduce no timing delays due to the shape of their surface.

5.2 Equipment and Data Taking

A schematic diagram of the experimental system used to measure pulse profiles is shown in figure 5.1. The signal to be digitized is taken from a single on-axis three inch photo-tube (EMI 9822B) on one of the mirrors of the Woomera telescope. This signal is amplified by a twin output 10 times gain high bandwidth amplifier (LeCroy vv100b). One output of this amplifier is sent to a local electronics rack and the other is sent to a digitizer located in the control hut some 40m from the telescope. The signal to the local electronics rack is used in fast coincidence with the other photo-tube signals to generate event triggers. This event trigger is also sent to the control hut to trigger the digitizer.

The digitizer is a Tektronix 7912 transient digitizer. The 7912 has 9 bit vertical and horizontal resolution and an analogue bandwidth of 500 MHz. When tube rise-time, amplifier bandwidth and cabling are included the final bandwidth of the pulse profile measuring system is $\sim$ 150 MHz. The pulses are digitized over a 50 ns window with digitization steps of 0.2 ns. The event arrival times are stored to a relative accuracy of 1 ms, although by comparing these times to those measured by the main system the absolute arrival times can be determined to to better than 1ms. A pulse captured by the 7912 is transferred to a personal computer and stored in RAM drive. At the end of each run the files stored in RAM are transferred to hard

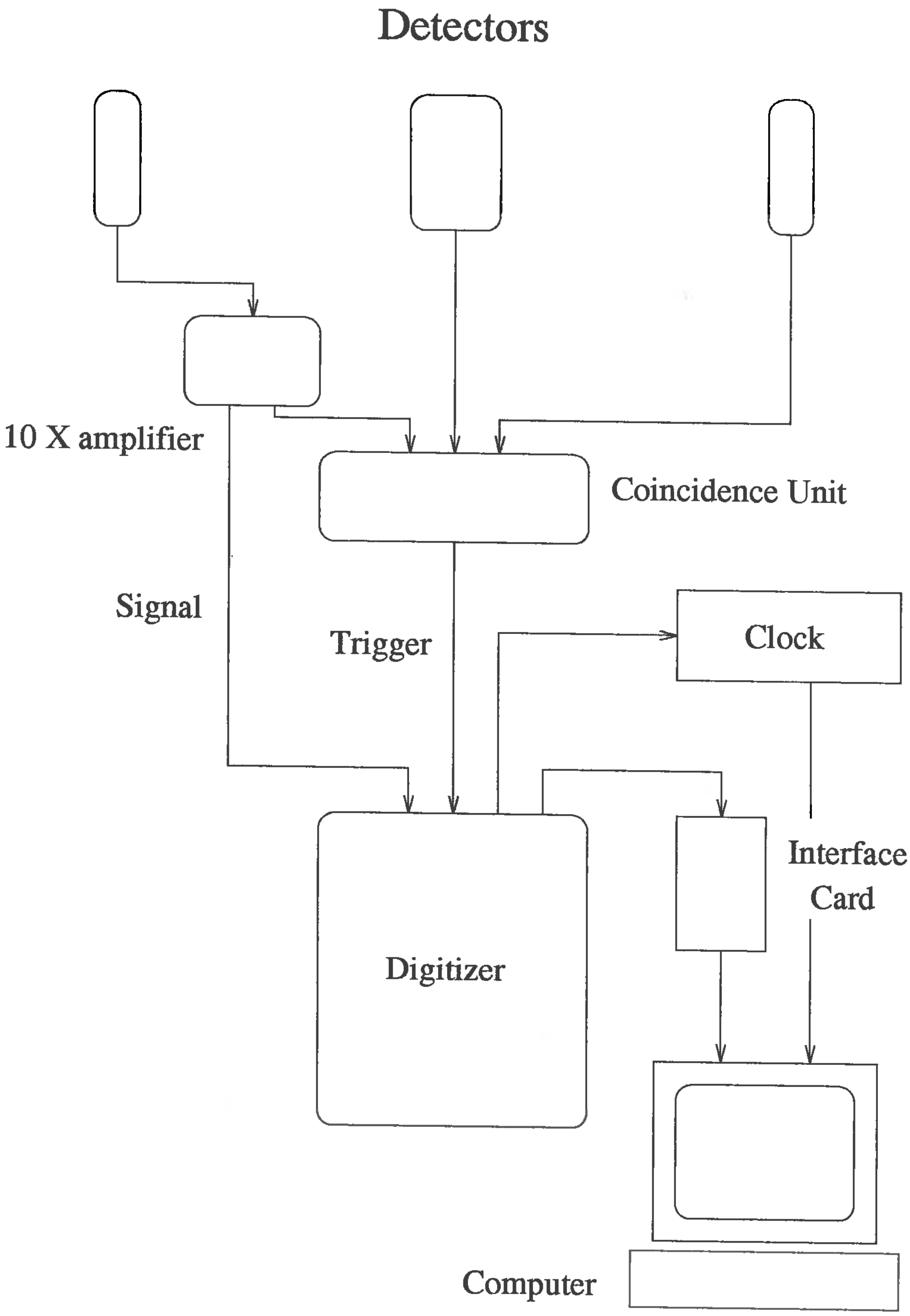

Figure 5.1: Schematic diagram of pulse profile measurement system

drive and then to tape.

The dead time for the digitization of a single pulse is about 200 ms. Although the dead time is quite long it is not generally a problem when observing at large zenith angles where the event rate is < 1Hz.

Before the pulses can be analyzed each digitized pulse undergoes a number of processing procedures. The first of these is "cleaning", in which any stray bits that have registered away from the main pulse are removed. Each pulse is then tested to see if it has been digitized well enough to be accurately reconstructed. This is mainly a problem for very large pulses, where some part of the pulse is off scale. If a certain fraction of pulse has not been captured then the event is rejected. Typically only a few percent of events will be rejected in this way. Finally, the pulse profile is reconstructed from the digitized pulse by interpolation (usually at intervals of 0.1 ns).

5.3 Pulse Shape Formation

In order to use pulse profile measurement to differentiate between gamma-ray and cosmic ray EAS it is desirable to understand how the development of an EAS leads to the formation of a Čerenkov light pulse. This field received considerable attention in the 1970's and early 1980's from cosmic ray research groups attempting to study the longitudinal development of EAS. Most of this work involved the study of Čerenkov pulse profiles viewed by wide aperture detectors at large distances from the cores of EAS (Thornton and Clay 1979,1981, Orford and Turver 1981).

The time structure of Čerenkov light emitted from EAS will be determined by the geometrical path differences between the points of Čerenkov emission at the observation point, and by refractive index effects. As a starting point to the understanding of the formation of a pulse profile, consider the simple scenario outlined by Hillas (1982). Here the particles of the cascade are assumed to travel at velocity c (speed of light in vacuo) with small longitudinal spread very close to the shower axis (see fig 5.2). For such a shower, the spread in arrival times of the Čerenkov photons will be dependent upon the distance of the observer to the core of the shower (see figure 5.3).

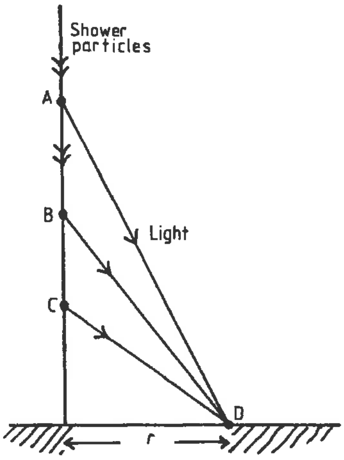

Figure 5.2: Simple shower model (from Hillas 1982)

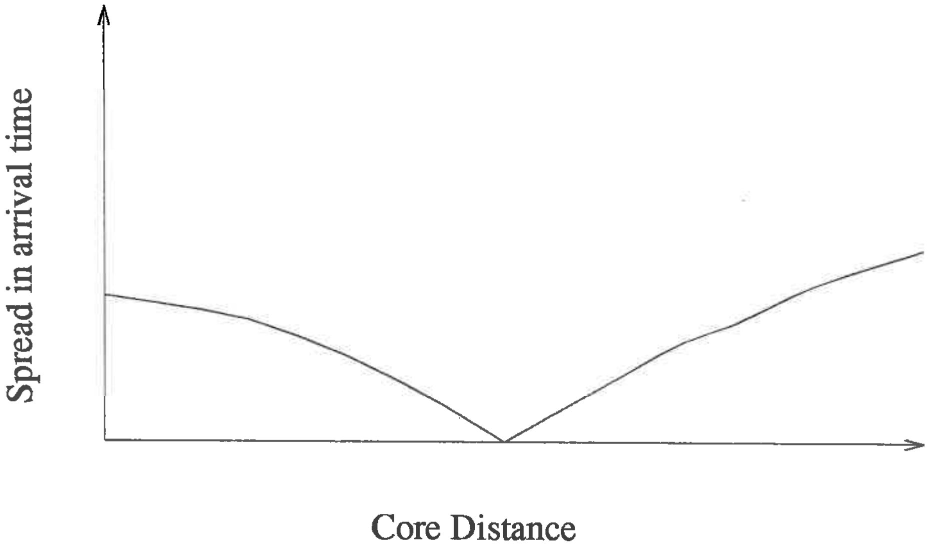

Figure 5.3: Schematic diagram of the expected variation in time spread of Čerenkov photons as a function of core distance for an idealized shower.

For an observer at the core the spread in arrival times will be due entirely to the refractive index delays of the Čerenkov photons with respect to the particle front. From figure 5.2, if the distance between A and C is H gcm^2 then the Čerenkov photons from A will arrive at a time δt later than those from point C, where

$$\delta t = \frac{2.29 \times 10^{-3}\mathrm{H}}{c} \mathrm{seconds} \tag{5.1}$$

For a vertical shower, therefore, the maximum possible time spread at the core will be of the order of 10 ns. As the cascade of figure 5.3 is observed at increasing distances from the core the spread in arrival times will decrease. This is due to geometrical path differences between the top and bottom of the shower compensating for the refractive delays of the Čerenkov photons. At some distance from the core the geometrical path differences and the refractive delays will cancel and the photons will arrive from all points of the shower at the same time. This is analogous to the Čerenkov effect, and for a typical vertical shower this point will lie at around 150 m from the core. Beyond this point the arrival time spread begins to increase again. At the larger core locations the geometrical delays dominate, so the observer will see light generated at the top of the shower arriving first.

It is clear that the model of figure 5.2 is an over-simplification of a real EAS. It takes no account of the finite particle front thickness in the cascade or the lateral spread of shower particles away from the core. Despite these limitations it does raise a number a interesting points that may be relevant to the identification of gamma-ray and cosmic ray EAS :

- The spread of arrival times of Čerenkov photons should reflect the longitudinal extent of the EAS (particularly inside the Čerenkov shoulder).
- Beyond the Čerenkov shoulder the spread in arrival times is strongly core location dependent. For a single VHE gamma-ray telescope, such as the Woomera telescope, identification of the core is not possible. It seems likely therefore, that measurement of pulse profiles for events that fall well away from the telescope will provide no useful information.

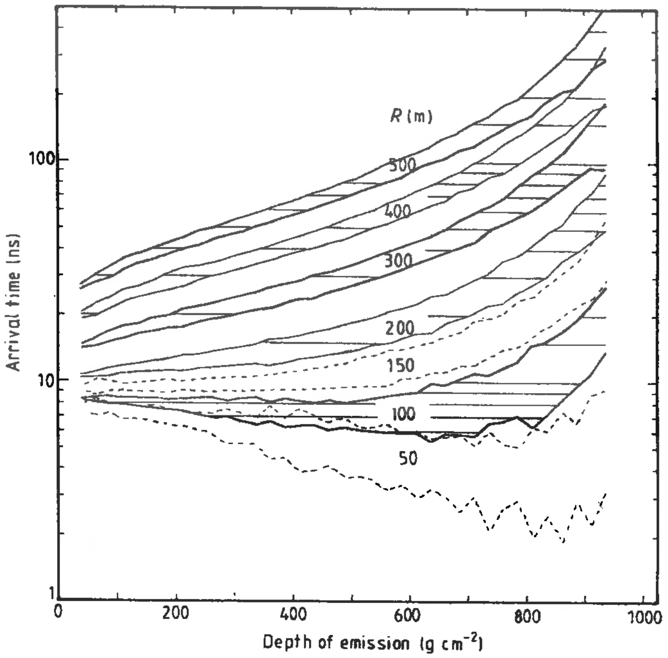

Figure 5.4: The spread in arrival times of Čerenkov photons as a function of emission depth. The numbers in the graph, R(m), indicate the core location (from Hillas 1982).

In figure 5.4 the Čerenkov photon arrival times as a function of core location and emission depth are shown. These data, from Hillas (1982), were generated from a sophisticated Monte Carlo simulation of cascade development. These plots contain useful information for observations at large core distances, but lack detail about the arrival time distributions near to the core.

To study pulse shapes nearer the core I have generated sets of 50 TeV primary Monte Carlo cascades using Hillas' MOCCA simulation program. These cascades were generated at a zenith angle of 65 degrees, which corresponds approximately to the culmination elevation of Hercules X-1 as viewed from Woomera. Groups of approximately 100 cascades were generated at core distances of 0, 325 and 650 meters for each species of primary particle. Four different primary particles were simulated: gamma-rays, protons, oxygen nuclei and iron nuclei. For core distances 0m and 325m the showers were viewed by four meter diameter mirrors. At 650m where the Čerenkov photon density is less, 6m diameter mirrors were used. No aperture limitation was placed on the angular acceptance of the Čerenkov photons. For each photoelectron that fell in a mirror the arrival time and angular position in the field of view were recorded. In addition, the height of photon emission and the position of photon emission with respect to the core of the shower was recorded, as well as the energy and type of emitting particle.

Using this information it is possible to relate the formation of a pulse profile at the point of observation to the development of the EAS. To gain a general feel for pulse development a program to display the development of each shower in a "movie" format was written. The point of emission (height of emission and radial distance to the core) of each Čerenkov photon is displayed on computer screen, one at a time, in order of Čerenkov emission time. For each photon the relative arrival time at the point of observation is displayed in a histogram at the bottom of the screen. Figures 5.5 and 5.6 show some examples of this type of display for gamma-ray and cosmic ray showers at various core locations. These movies allow us to make some general comments about the formation of pulse profiles

- The majority of the Čerenkov photons from the electromagnetic component of the shower are emitted from relatively near the core of the shower. These photons tend to arrive at the point of observation within a few nanoseconds of each other.

- The Čerenkov photons emitted away from the core have a wider spread in time at the point of observation. These photons often arrive after the photons emitted near the core, and so fall on the trailing edge of the pulse profile.

- The muon component penetrates deeper into the atmosphere than the electromagnetic component. The Čerenkov photons from the muon component tend to be found on the leading edge of the pulse profile.

Perhaps the easiest way to display these data is to generate "average" pulse profiles from the Monte Carlo data set. These average pulses are found for both cosmic ray and gamma-ray events by adding the individual pulses together. The pulses are aligned at the maximum pulse height of Čerenkov emission due to the electromagnetic component of the showers. These pulses are shown in figures 5.7, 5.8, 5.9 and 5.10. Also shown are the contributions to the pulses from the

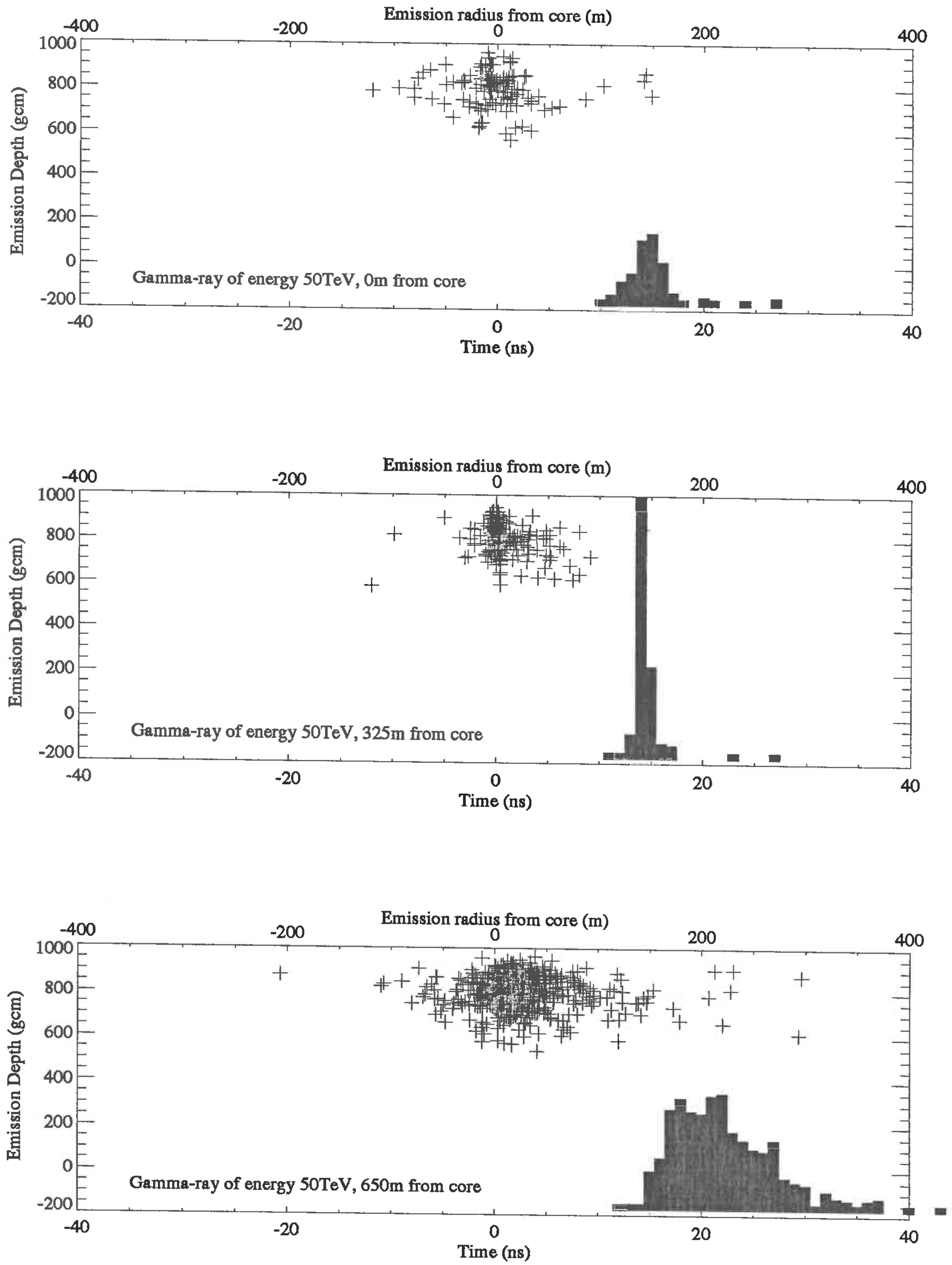

Figure 5.5: "Movie" display of the pulse formed from a gamma-ray initiated EAS at a zenith angle of 65°. The top horizontal scale and the left vertical scale give the position of emission of the Čerenkov photons. The crosses indicate emission from an electron or positron, the triangles indicate emission from a muon. The histogram gives the pulse profile seen by the observer.

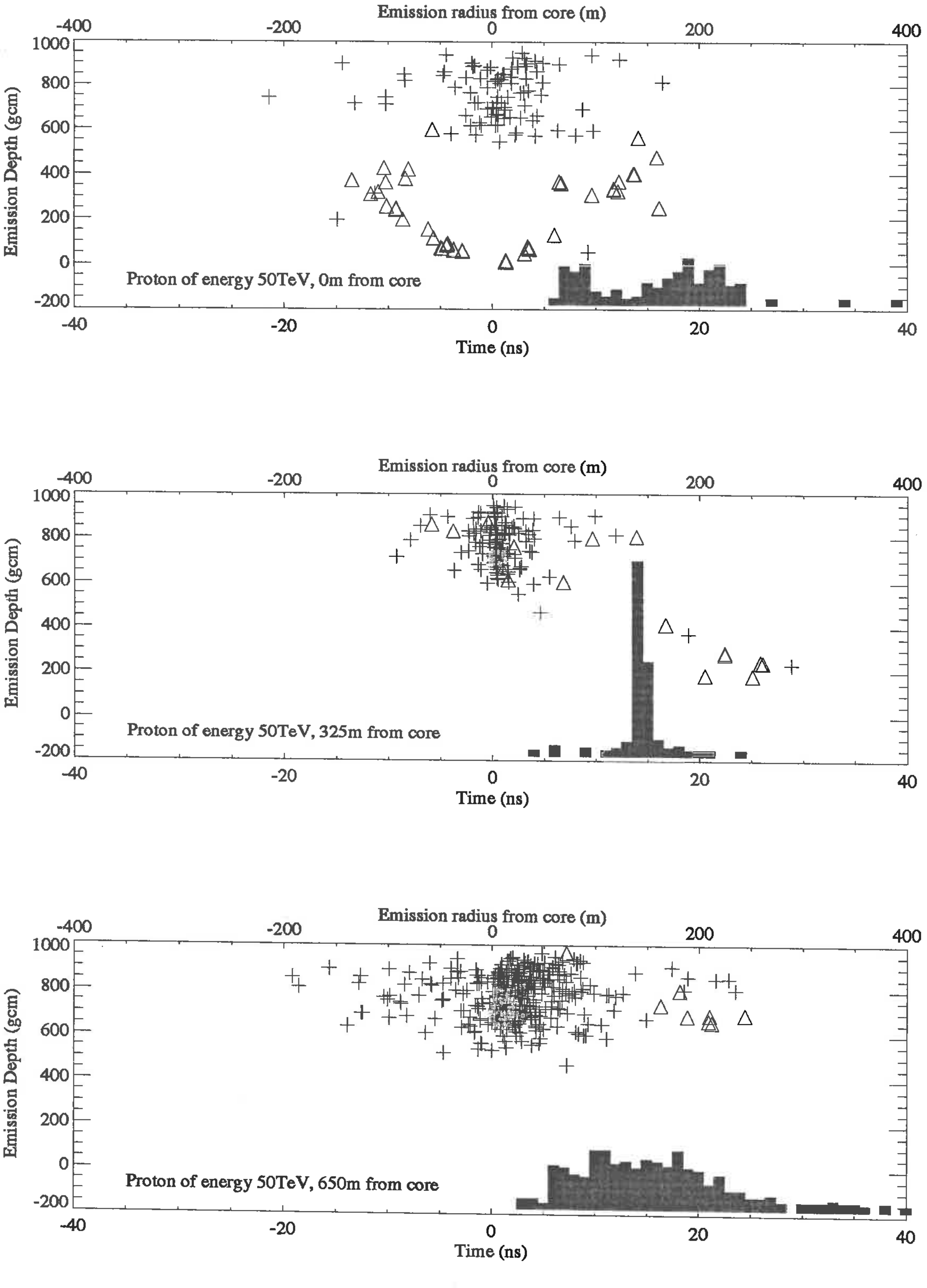

Figure 5.6: Same as for previous figure but for a proton initiated EAS.

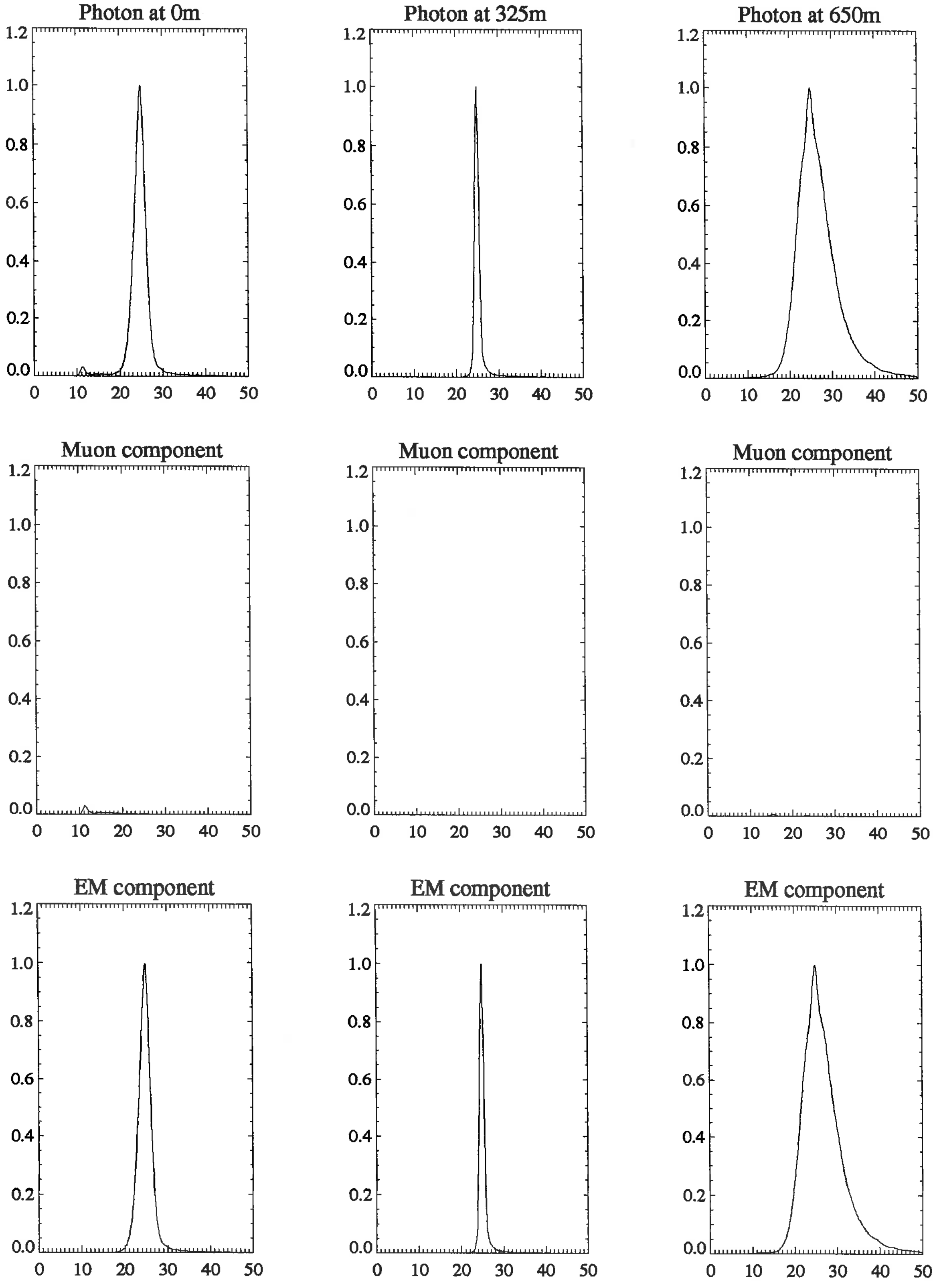

Figure 5.7: Monte Carlo simulation of average pulse profiles produced by gamma-ray primaries at 0m, 325m and 650m from the core (top). Also shown separately are the contributions to the total pulse from Čerenkov photons produced by the muonic (middle) and electromagnetic (bottom) components of the cascade.

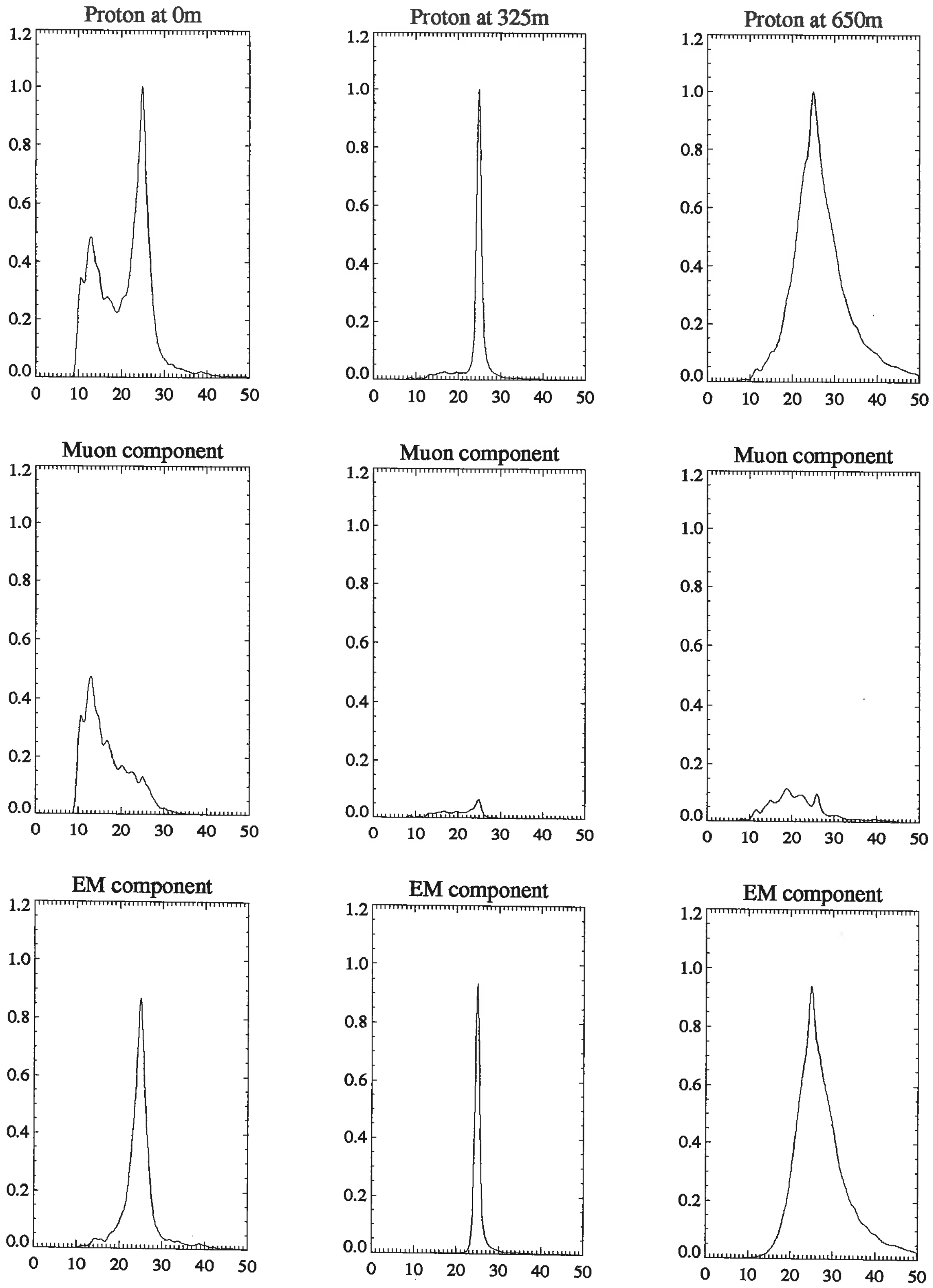

Figure 5.8: Average time profiles for proton initiated EAS

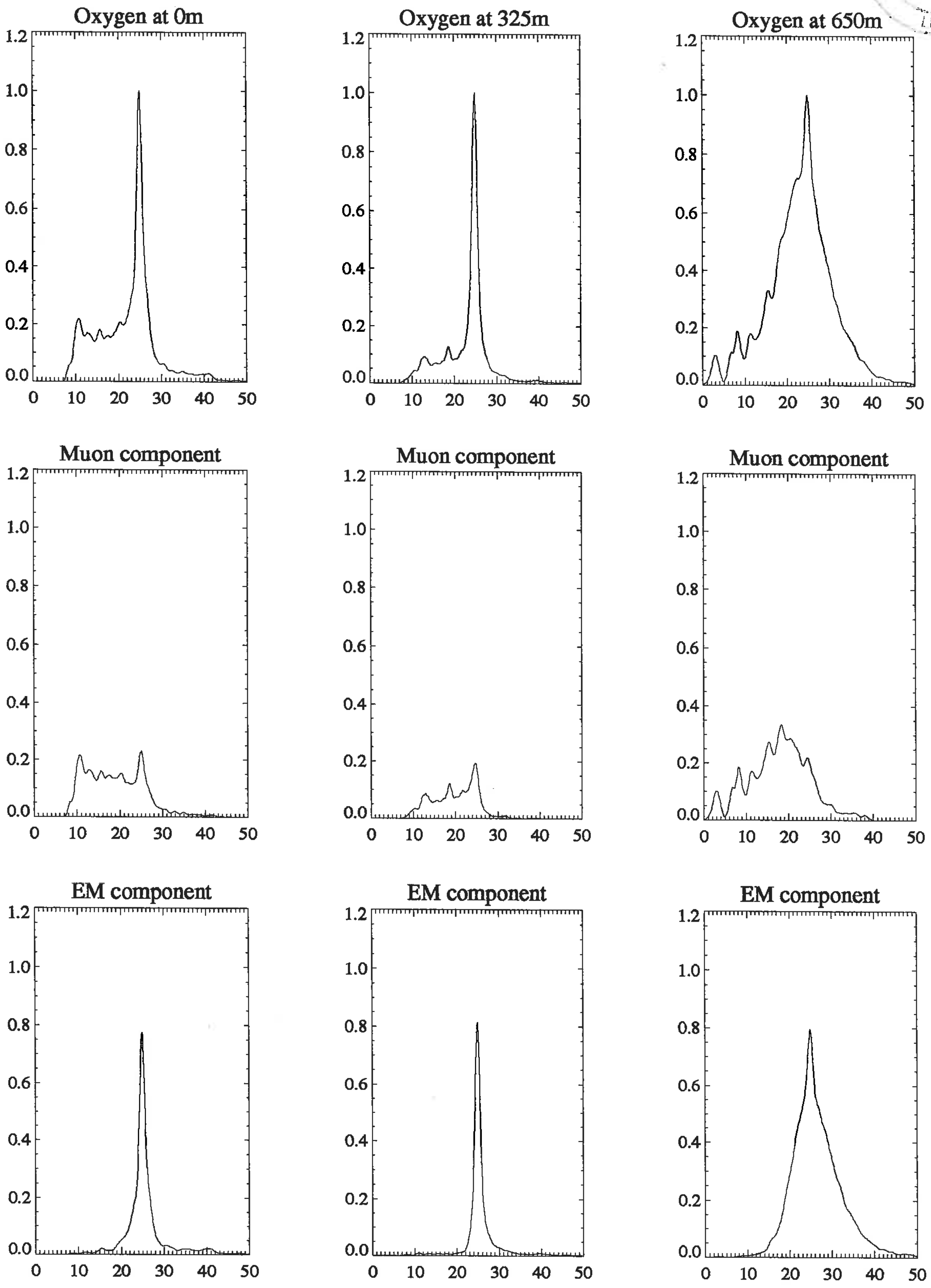
Oxygen at 0m

Oxygen at 325m

Oxygen at 650m

Muon component

Muon component

Muon component

EM component

EM component

EM component

Figure 5.9: Average time profiles for oxygen nuclei initiated EAS.

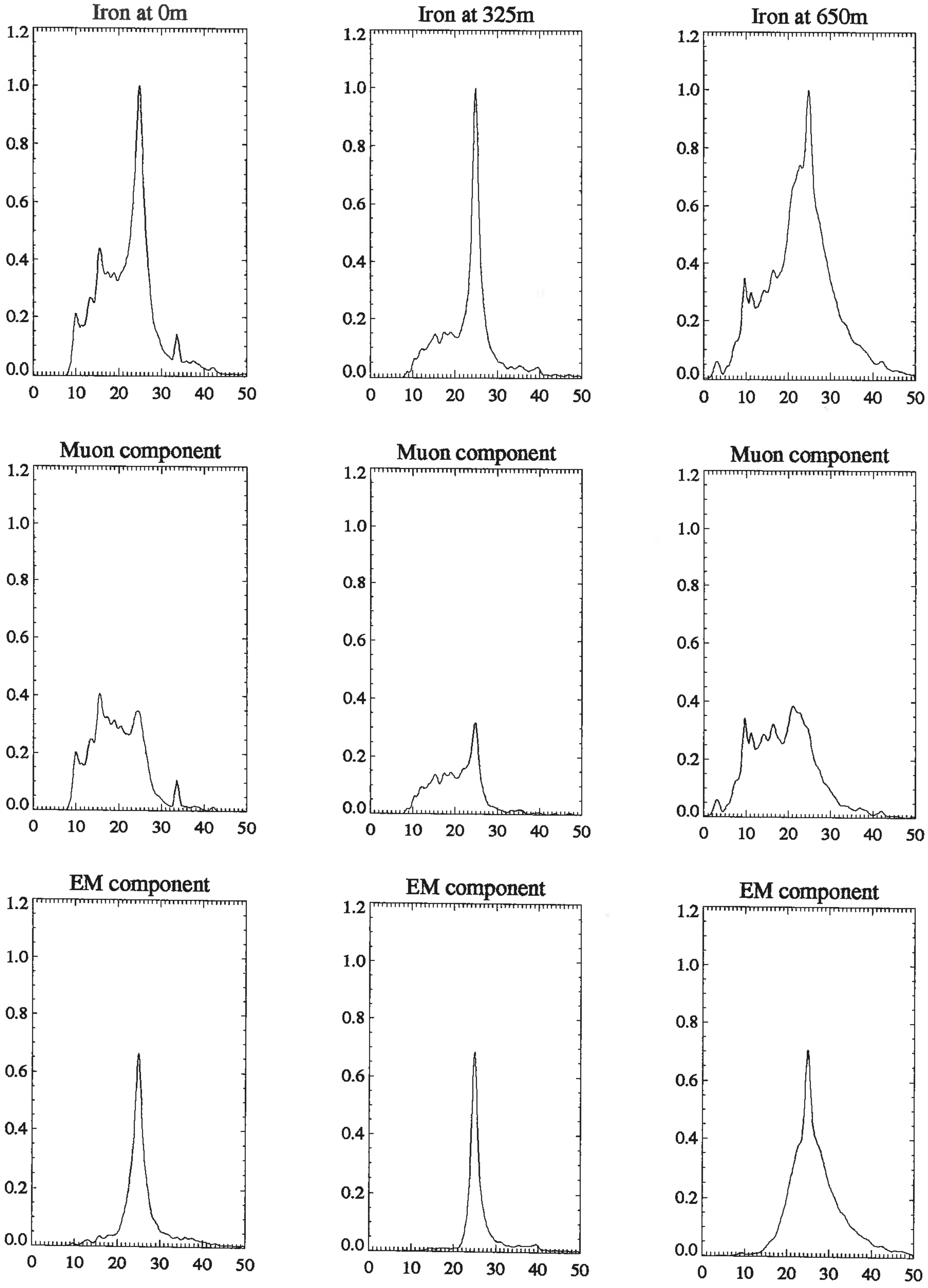

Figure 5.10: Average time profiles for iron nuclei induced EAS.

electromagnetic and muonic components of the showers. These figures show clearly that the Čerenkov emission from the muonic component tends to be seen on the leading edge of the pulse profiles. These simulations also show that at any given core location the average spread in arrival times is smaller for gamma-ray initiated EAS than for cosmic ray initiated EAS.

Figures 5.11 and 5.12 show some details of the Čerenkov emission from the electromagnetic particles of the proton initiated cascades. These scatter plots display the relative arrival times of the Čerenkov photons at the point of observation as a function of the position of emission relative to the core (shower axis). Several cascades are shown on each plot and as before the times are aligned at an arbitrary time (25 ns) so that the peak of photon emission for each shower coincides.

The plots on the left show the relative arrival times of the photons, as a function of radial distance to the core, of the emitting particles. As expected the particles farthest from the core produce photons with the largest spread in arrival times. For showers observed at the core, photons emitted at larger core distances are delayed with respect to the main Čerenkov emission. If the shower is observed away from the core then the photons from these particles may arrive before or after the main Čerenkov emission.

The plots at the right in figures 5.11 and 5.12 show the relative arrival time as a function of vertical emission depth (in gcm^{-2} where 0 corresponds to the top of the atmosphere). These plots show the general features of the simple model of pulse formation discussed earlier. For showers observed near the core, photons emitted at the top of the shower tend to arrive later than those emitted nearer the ground. At 325m from the core ($\sim$ Čerenkov shoulder at 65° zenith angle) the relative arrival time is not sensitive to the height of emission. Beyond the Čerenkov shoulder photons emitted at the top of the cascade tend to arrive ahead of those emitted lower down. Figure 5.12 shows the same information as figure 5.11 but for the Čerenkov photons emitted from the muonic component of the showers. On average the light contribution from the muons tends to occur further from the core than for the electromagnetic particles. The muons also tend to contribute more light closer to the telescope than the electromagnetic particles. Figure 5.12 shows that for muons the

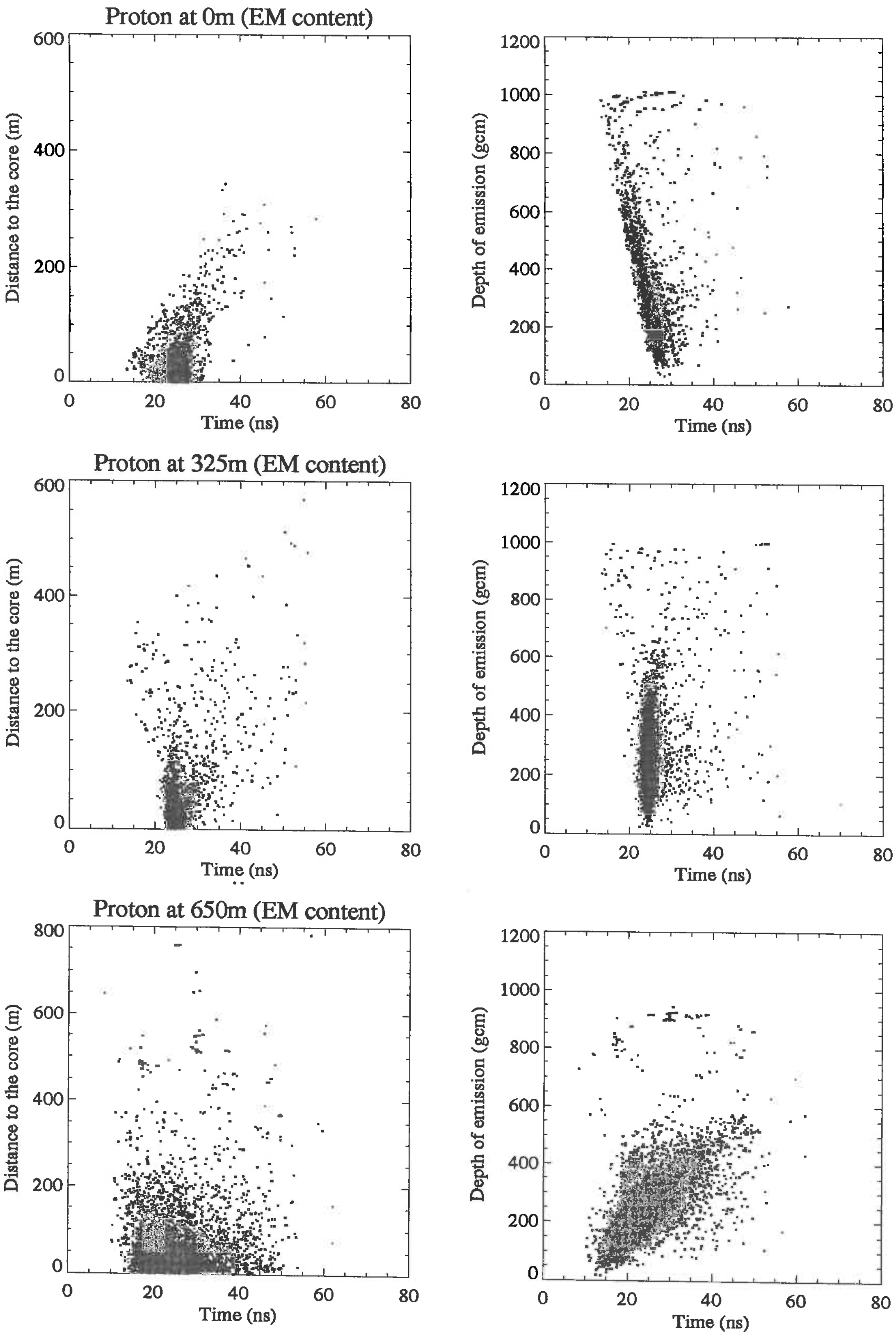

Figure 5.11: Scatter plot of the relative arrival times of Čerenkov photons emitted from the electromagnetic particles of EAS at various core locations (left column). In the right column is the corresponding arrival time vs. depth of emission information.

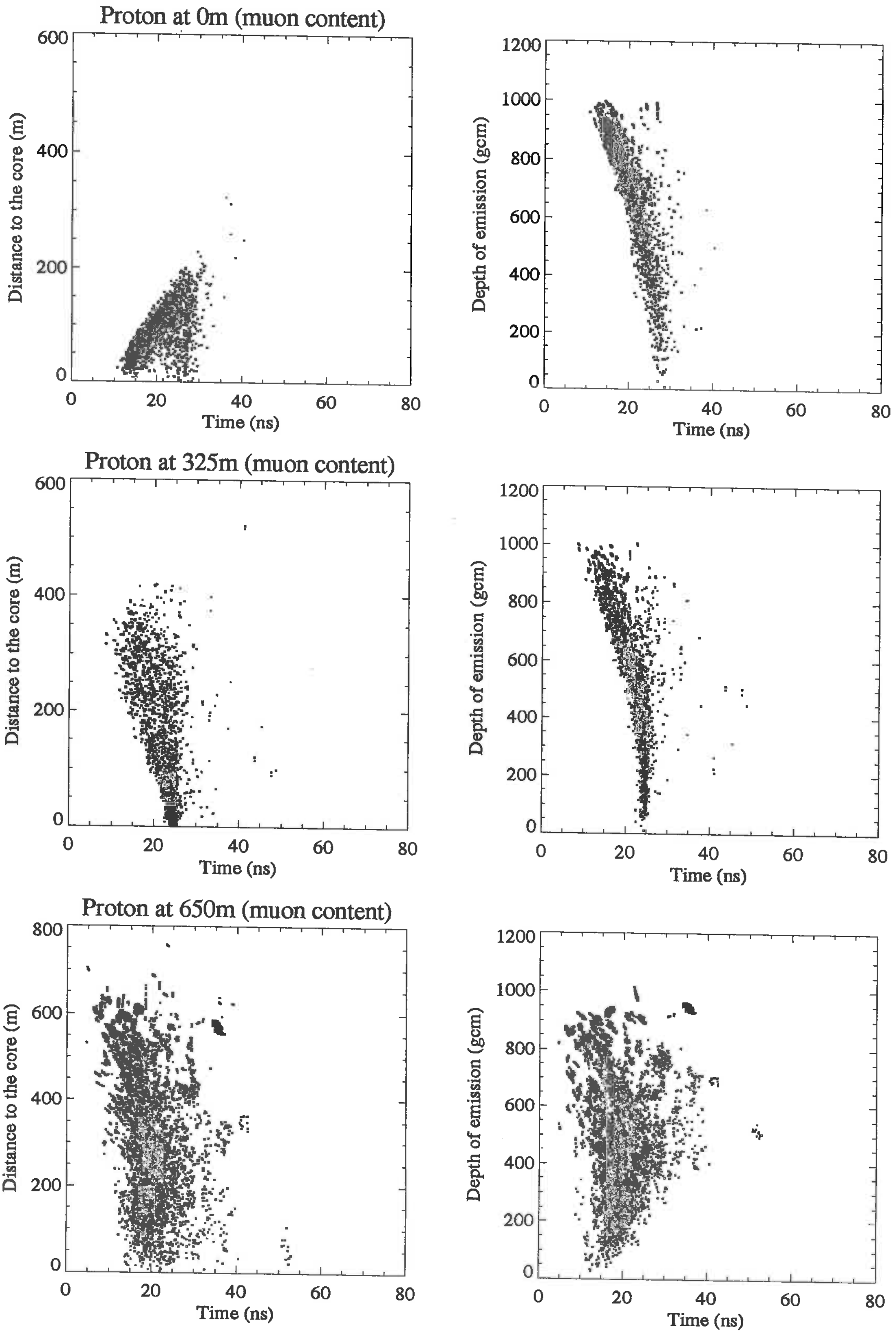

Figure 5.12: Same as for previous figure, but for Čerenkov photons emitted from the muonic component of the EAS.

light emitted closer to the observer will tend to arrive before light emitted higher in the atmosphere for all core distances.

5.4 Pulse Profile Cuts

To use the measurement of pulse profiles to enhance gamma-ray sensitivity we must devise parameters that are sensitive to the differences between the pulse shapes of gamma-ray and cosmic ray EAS.

Tümer et al.(1990), when looking at near vertical showers from the Crab Nebula, classified the pulse profiles in terms of the number of "kinks" on the pulse and on the shape of the trailing edge. The kinks are secondary maxima, either before or after the main pulse. The presence of kinks is assumed to be indicative of cosmic ray EAS. Secondary maxima were seen in early pulse profile measurements (Bosia et al. 1972). Tümer et al. also rejected cosmic ray events on the shape of the trailing edge of the pulse. Cosmic ray EAS were assumed to produce pulse profiles with extended trailing edges, while gamma-ray EAS were assumed to produce a shorter trailing edge. Using these cuts, Tümer et al. claim that they can achieve a quality factor (as defined in chapter 4) for signal enhancement of $q \sim 4$.

I have decided not to use the cuts described by Tümer et al. for a number of reasons:

- The pulse profiles measured by the Woomera system show no kinks above a level attributable to sky noise. This may be due to differing signal to noise ratios of the two systems (Woomera - $E_{threshold}$ ~500GeV, mirror area $\sim 12m^2$, Sandia - $E_{threshold}$ ~600GeV, mirror area $\sim 95m^2$).
- It is often difficult to "tune" the trailing edge of a photo-tube pulse to give a clean, smooth and consistent trailing edge. This makes it difficult to identify genuine features of an EAS pulse profile on the trailing edge of a pulse.
- Monte Carlo simulations of cosmic ray EAS do not indicate a large signal on the trailing edge of the pulse profiles. Also, these simulations do not indicate that a large number of the cosmic ray events have significant kinks on the pulse

profiles. Patterson and Hillas (1989) have also showed that the quality factor attained by identifying the secondary maxima of cosmic ray initiated EAS is only ~ 1.2.

- It is difficult to write software that can reliably identify the kinks on a pulse profile. Tümer et al. identified the type and number of kinks manually. This type of analysis is not desirable because it is extremely time consuming and it is difficult to achieve consistency in making cuts.

Instead I have decided to use, at least initially, more conventional pulse parameters. The parameters used most extensively are rise-time (10% to 100% of pulse maximum), fall-time (100% to 20% of pulse maximum) and full width at half maximum (50% to 50% of pulse maximum). The description of fall-time was influenced by the noisy and highly variable nature of the trailing edge of the photo-tube pulse.

Figures 5.13 and 5.14 show pulse parameter distributions measured with BIGRAT for zenith angles 0, 35, 55, 65 and 75 degrees. Figure 5.14 also shows the delta function response of the pulse measurement system for the same pulse parameters. The delta function response was measured by recording the pulses from muon Čerenkov tracks through slabs of glass placed against the face of the photo-tube. This method does not include the effect of the mirror surface on the formation of the pulse, but this has been measured and was found to be negligible.

Figures 5.15 and 5.16 show Monte Carlo simulations of the distribution of pulse parameters for BIGRAT at 65° from zenith. This set of Monte Carlo data was designed to realistically simulate the response of the Woomera telescope to gamma-rays and cosmic rays at approximately the culmination elevation of Hercules X-1. The energy of showers was selected from an appropriate distribution (integral spectrum of -1.65 for cosmic rays and -1.1 for gamma-rays) starting from an energy just beneath the triggering threshold of the telescope at this elevation. The core locations for the cascades were selected from an appropriate distribution out to a distance of 700m. The mirrors in the simulation program were configured to match those of the Woomera telescope and the aperture was limited to the largest angular

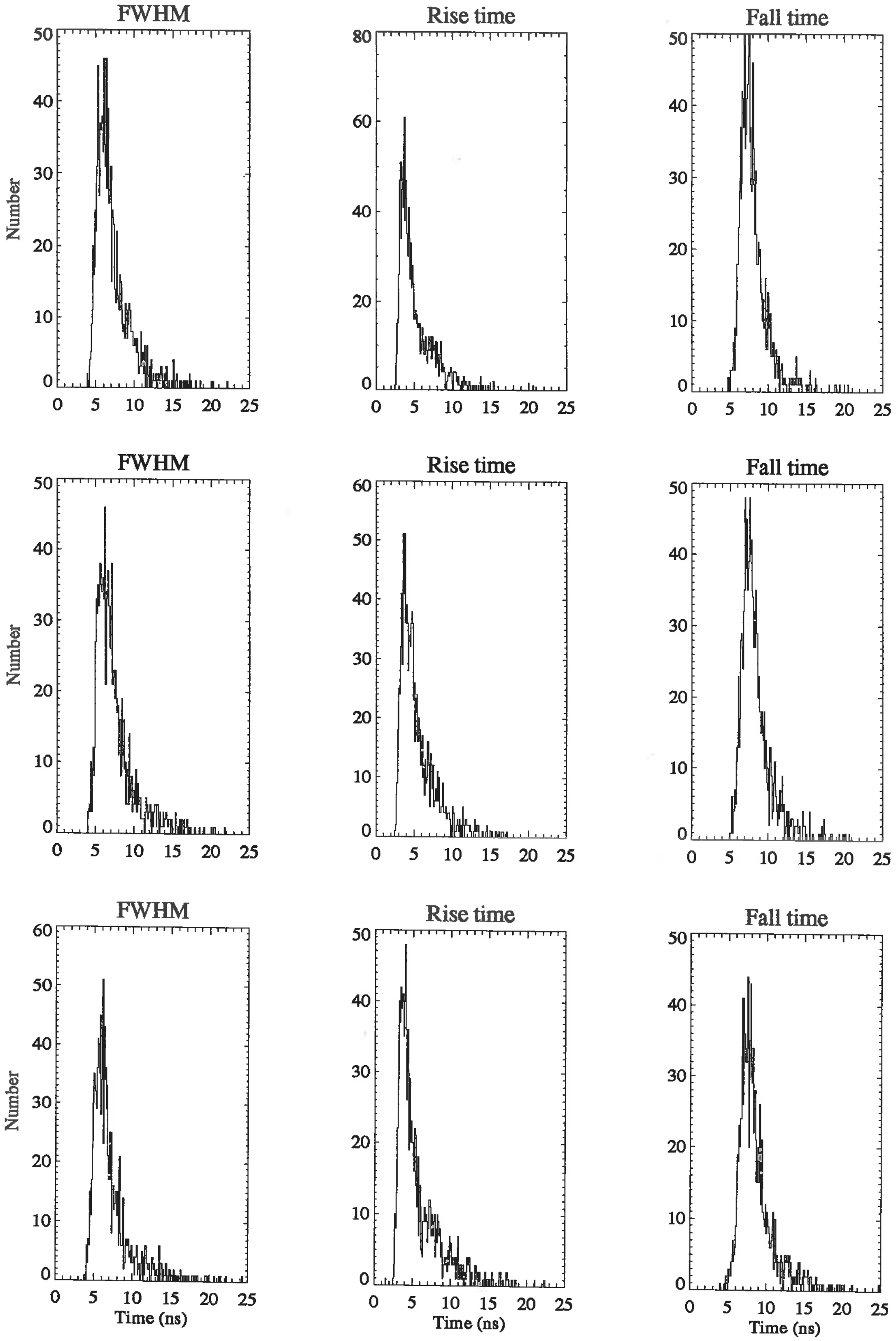

Figure 5.13: Measured pulse parameter distributions for showers at zenith (top), 35° (middle) and 55° (bottom) from zenith.

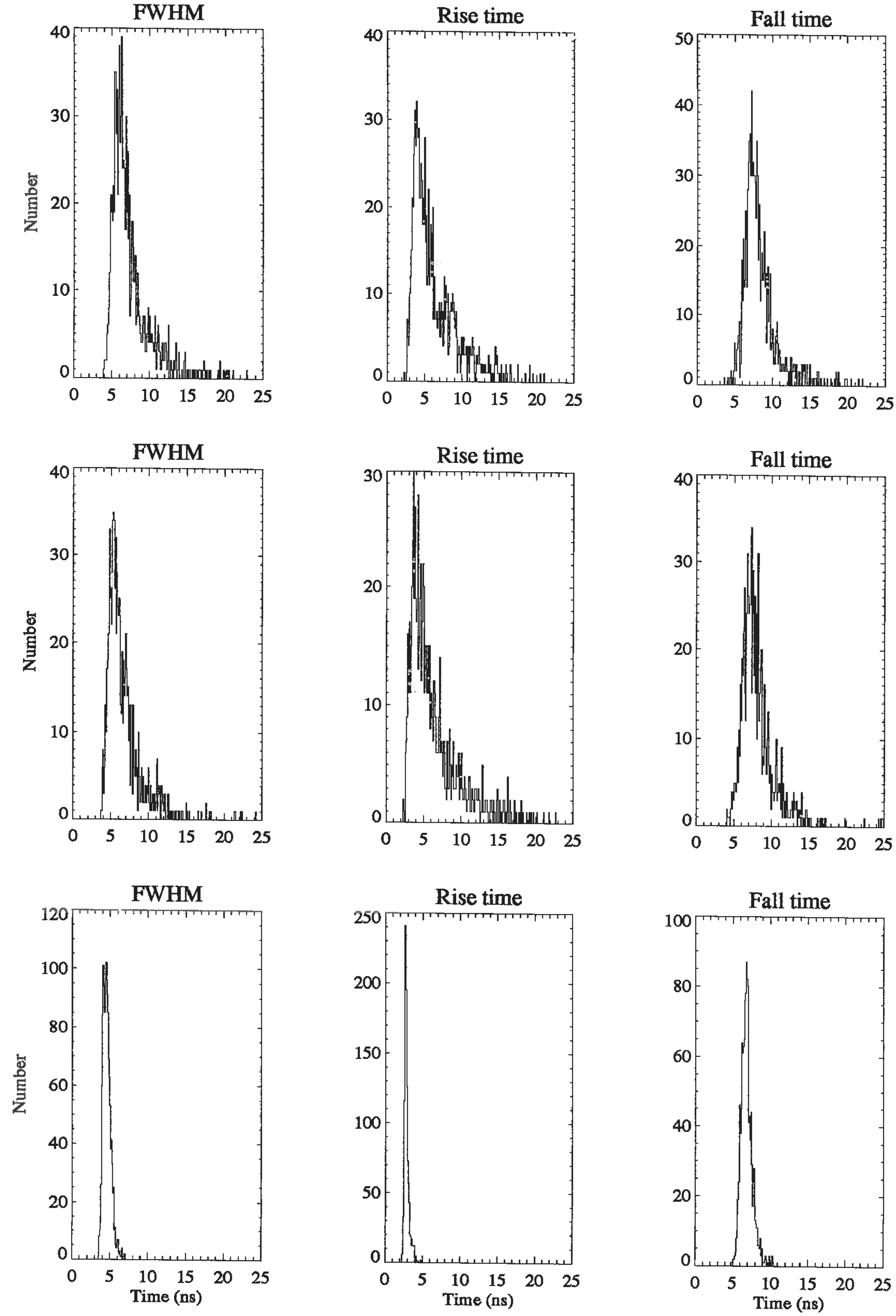

Figure 5.14: Measured pulse parameters for 65° (top) and 75° (middle) from zenith. The bottom graphs show the delta function response of the pulse measurement system.

acceptance that is reasonable for the Woomera telescope. The selection of the energy, core location and angular displacement of the EAS is described in more detail in section 3.3.2. Figures 5.15 and 5.16 show the distributions of pulse parameters for Monte Carlo gamma-rays, protons, oxygen nuclei and iron nuclei that trigger the Woomera telescope. To make the simulations realistic, system noise and experimental response must be included.

Noise is added to the Monte Carlo pulses by taking actual measurements of the sky noise. This is achieved by artificially triggering the pulse measurement system while tracking Hercules X-1. These sky noise pulses are then converted to a photoelectron scale and added to the simulated pulses. This method takes account of sky noise, tube noise and any electrical interference that is measured by the system.

The experimental response of the system is modeled by assuming that the single photoelectron response of the system and the delta function response are the same. A selection of delta function responses are recorded (as in figure 5.14), and the height of each is normalized to one photoelectron. For each Monte Carlo photoelectron in a pulse profile the normalized delta function response is added at the arrival time of the photoelectron. A different delta function response pulse is used for each Monte Carlo pulse profile that is generated. This reproduces the fluctuations inherent in the pulse measurement system. By using the actual delta function response of the system we may then compare the Monte Carlo simulated pulses directly with those measured on the telescope.

From a comparison of the 65° data in figure 5.14 and figure 5.15 it is clear that the observed pulse parameter distributions cannot be explained by a pure proton primary composition. It may be possible, using Monte Carlo parameter distributions for various primary species, to make a crude estimate of the primary cosmic ray composition. I have done some preliminary work on composition for data taken at 65° from zenith, which corresponds to primary energies of around 30TeV. The approach I have taken is to generate Monte Carlo pulse parameter distributions for proton, helium, oxygen and iron primaries at this zenith angle. The parameter distributions are then mixed in different ratios to try and reproduce the the observed pulse parameter distributions. Great care must be taken when generating the Monte

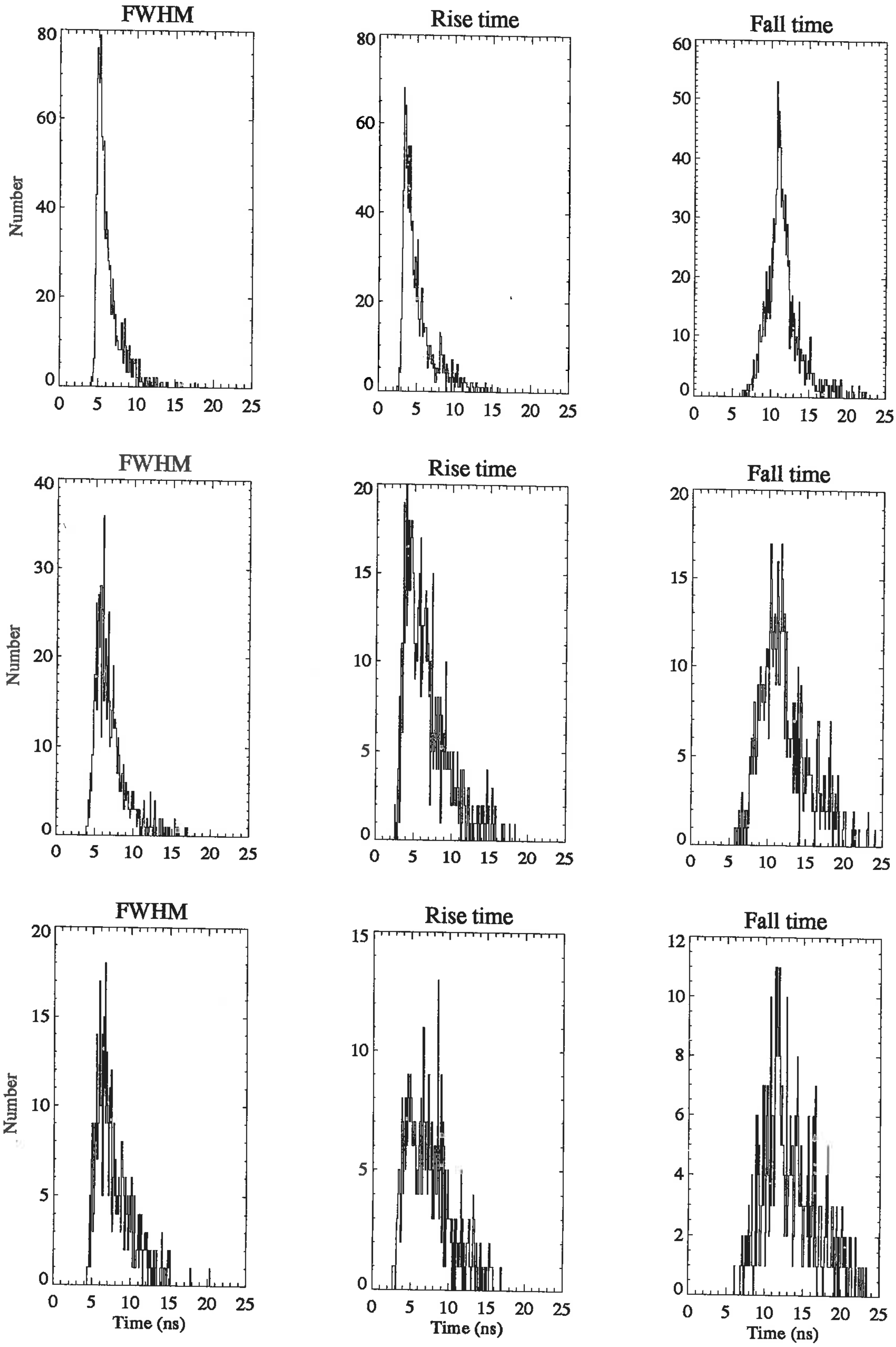

Figure 5.15: Monte Carlo pulse parameter distributions at 65° from zenith for proton primaries (top), oxygen primaries (middle) and iron primaries (bottom).

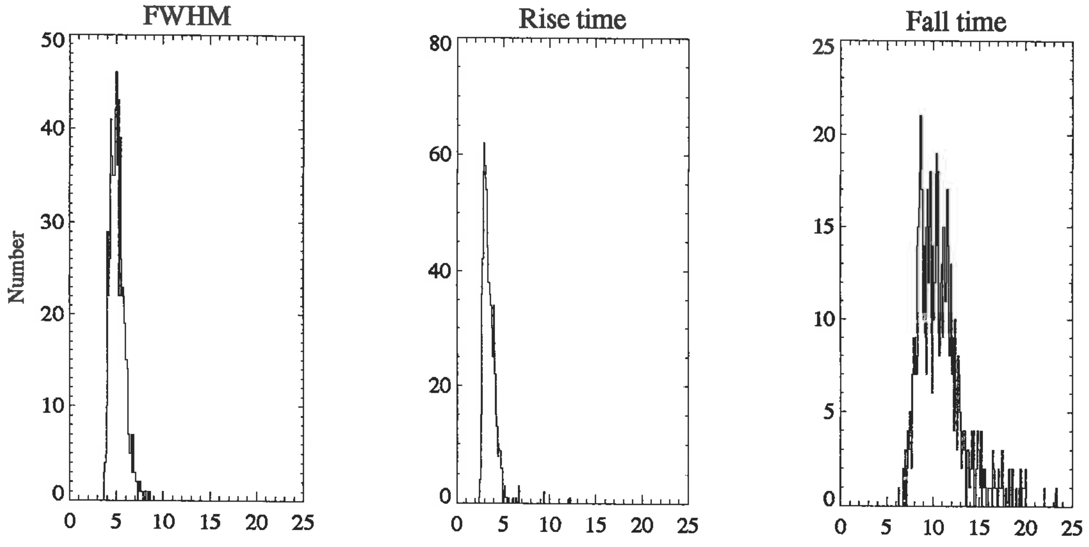

Figure 5.16: Monte Carlo pulse parameter distributions for gamma-rays at 65° from zenith.

Carlo pulse profiles to account for systematic effects introduced into the measured pulse parameter distributions by instrumental effects. It is possible, by using this method at different zenith angles, that the primary cosmic ray composition may be estimated over a large range of energies (~TeV to ~PeV). The accuracy of the method could be tested at the lower energies by comparing results with direct measurements of the primary cosmic ray composition. No results are presented here because the work is only preliminary and it is beyond the scope of this thesis.

5.5 Making Parameter Cuts

Having described the pulse profiles in terms of rise-time, fall-time and FWHM it is now necessary to define the "gamma-ray domains" for these parameters. We must also decide upon the method of implementing these cuts, and whether any other factors must be included when trying to select the gamma-ray like events.

Pulse Maximum Cut

Firstly, we must consider the effect of the pulse maximum on our ability to

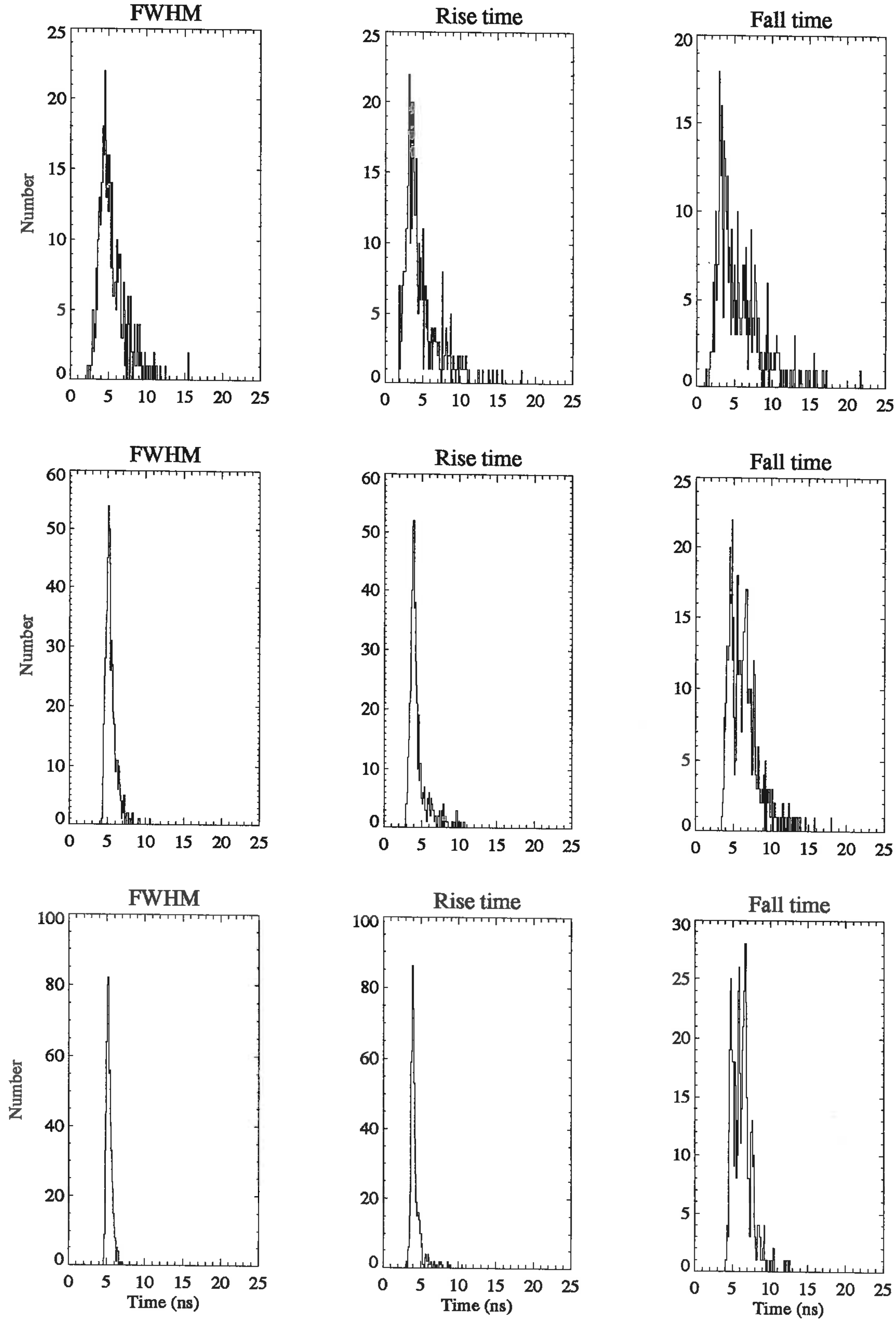

Figure 5.17: Blurring of the pulse parameters for an ideal (delta function) pulse of height 5 photoelectrons (top), 15 photoelectrons (middle) and 25 photoelectrons (bottom). See text for details.

determine the other pulse parameters. Pulse maximum describes the maximum height of the main peak of a pulse profile. If pulses are accepted that are too small, then this could lead to errors in assigning other pulse parameters because of sky noise contamination. Figure 5.17 shows the effect of sky noise on the delta function response of the pulse measurement system for pulses of varying pulse maximum. A single pulse profile, generated from a muon track through glass, is repeatedly parameterized with a selection of sky noise profiles added. Figure 5.17 shows the blurring of the delta function response of the system for these pulses scaled to have pulse maxima of 5, 15 and 25 photoelectrons.

For the analysis of Her X-1 data I have chosen 25 photoelectrons as the minimum acceptable pulse height. At this level, the blurring of pulse parameters is less than the fluctuations in the delta function response of the system. For data collected with the camera on the Woomera telescope a 25 photoelectron cut rejects about 40 % of events. For the triplet detector system, which has a lower threshold, about 50 % of events are rejected (see section 3.3.1 for a description of these detectors).

For another source, with different sky noise characteristics, it would be necessary to repeat this process with new sky noise measurements to determine the value of the pulse maximum cut.

5.6 Rise-time, FWHM and Fall-time Cuts

The lack of a strong southern hemisphere "standard candle" makes the experimental determination of optimum cuts impossible. I have derived parameter cuts by comparing the parameter distributions of Monte Carlo gamma-rays with the measured cosmic ray parameter distributions. Table 5.1 shows the maximum quality factors for the three pulse parameters at various zenith angles. Only quality factors for which >40% of the gamma-rays are accepted are included in this table (not including events rejected by the pulse maximum cut).

Table 5.1 shows that the quality factors for the FWHM and rise-time cuts vary with zenith angle. For the FWHM cut the maximum quality factor that is attainable

	0°	35°	55°	65°	75°
FWHM	2.04 ± 0.15 (42.2/4.3)	2.24 ± 0.16 (41.0/3.4	1.45 ± 0.10 (45.1/9.6)	1.71 ± 0.10 (62.3/13.3)	1.35 ± 0.09 (71.1/27.8)
Rise-time	1.51 ± 0.11 (46.0/9.3)	1.83 ± 0.12 (46.8/6.5)	1.61 ± 0.12 (42.5/7.0)	2.0 ± 0.13 (45.5/5.2)	2.25 ± 0.19 (44.4/3.89)
Fall-time	1.0 (100/100)	1.0 (100/100)	1.0 (100/100)	1.0 (100/100)	1.0 (100/100)

Table 5.1: Maximum quality factors for each pulse parameter cut at various zenith angles. The numbers in brackets are the (% of accepted gamma-rays/% accepted cosmic rays).

decreases with increasing zenith angle, while the opposite is true for the rise-time cut. The changes with zenith angle are due to the way the parameter distributions for a given species of primary change with zenith angle. In addition to this the composition of the cosmic rays may be changing as the threshold energy of the telescope changes.

The distribution of rise-time parameters gets markedly broader for a given species of cosmic ray with increasing zenith angle. This can be explained in terms of an increased percentage of the Čerenkov signal from muons as the zenith angle increases. For protons, for example, the Monte Carlo simulations show that the average muon contribution to the total Čerenkov signal increases from 10% at zenith to 20% at 65° from zenith. For gamma-ray EAS, which have no significant muon content, the rise-time distribution only broadens slightly with increasing zenith angle. This leads to a small increase in the quality factor with increasing zenith angle. This effect would be enhanced if the composition of primary cosmic rays were to get heavier with increasing energy. Table 5.2 shows how the maximum quality factor varies with primary species at a zenith angle of 65°. It can be seen that the heavier cosmic rays produce broader rise-time distributions and hence higher quality factors. Recalling figures 5.8, 5.9 and 5.10 this may also be explained in terms of the higher Čerenkov yield from muons for the heavier cosmic rays.

The FWHM distributions for both gamma-rays and cosmic rays broaden with increasing zenith angle. The overall effect of this is that the maximum attainable quality factor decreases with increasing zenith angle. For protons only, for example,

	protons	helium	oxygen	iron
FWHM	1.18 ± 0.06 (92.4/61.5)	1.29 ± 0.07 (90.4/49.5)	1.54 ± 0.09 (62.3/16.5)	2.44 ± 0.16 (44.9/3.3)
Rise-time	1.34 ± 0.07 (87.2/42.4)	1.62 ± 0.11 (45.5/7.9)	3.16 ± 0.21 (45.5/2.1)	3.74 ± 0.25 (45.5/1.5)
Fall-time	1.0 (100/100)	1.0 (100/100)	1.0 (100/100)	1.19 ± 0.07 (64.1/29.0)

Table 5.2: Maximum quality factor attainable for various primary species at 65° from zenith.

q for the FWHM cut changes from around 1.9 at zenith to 1.2 at 65° from zenith. Table 5.2 shows that an increasingly heavy composition at higher energies would tend to offset this decrease in quality factor with increasing zenith angle.

Table 5.1 shows that the maximum attainable quality factor at any zenith angle for the pulse shape technique is around 2. Early simulations of the camera on the Woomera telescope show that it will have a quality factor of 2–2.5. Thus the quality factor of the pulse measurement technique is comparable to that of the Woomera camera system. The pulse measurement technique also has the advantage of being cheaper and simulations show that it will work for observations at all zenith angles.

Pulse Cut Methodology

When applying camera image cuts it is possible to define the gamma-ray domain in terms of absolute parameter values. For pulse shape cuts, however, this has not proved to be practicable. The pulse shape cuts are made on the edges of rapidly changing distributions. Small changes in the value of a given parameter cut can cause large changes in the percentages of events passing the cut. Tests between data taken over a period of time have shown that consistent cuts cannot be achieved for absolute parameter value cuts. It is possible that changes in the photo-tube response or in the atmospheric conditions could cause this problem. Instead of a fixed cut, I have decided to use a "percentile cut", where a given percentage of all events recorded are accepted by a cut. The value of the percentile cut will then be given by the percentages of accepted cosmic rays in table 5.1. Clearly if a gamma-ray signal is present, the fraction of gamma-rays passing the cut will not be fixed. Figure 5.18 shows the variation in quality factor (q) as a function of the percentage of gamma-rays present in a sample. This figure is for the rise-time parameter at an zenith angle of 65° using the optimum rise-time cut given in table 5.1.

While the fixed percentile method of making cuts is most obviously applicable to searches for periodic signals, it may possibly be modified for DC excess searches. In a typical DC excess search observations are made of the search region and one or more background regions of sky. Pulse parameter cuts may then be made at a fixed percentage for, say, the on-source region. This percentage may then be translated to a parameter value for the on-source distributions, which can then be applied to the off-source regions. Care must be taken when using this approach to ensure that differences in the observing regions do not cause significant changes to the shapes of the pulse parameter distributions.

From table 5.1 it is possible to estimate which cuts should be used at each zenith angle. The approach I have taken is to use only the single parameter with the best quality factor at each zenith angle. While it is possible to increase the overall quality factor by using multiple cuts the improvement is small, reflecting the lack of independence of the parameters from each other.

While table 5.1 gives the optimum percentile cut at fixed zenith angles it may be better to increase the percentage of events accepted when analyzing real data files. This will allow for the fact that a real file is collected over a range of zenith angles. The bottom graph of figure 5.18 also shows that it is better to have a percentile cut that is larger than the optimum value rather than smaller. Accepting a larger percentage of events will also keep the quality factor high for a data set that contains a reasonably large percentage of gamma-rays. If a signal is found in the uncut data then the gamma-ray content can be estimated and the cut adjusted to give the optimum quality factor.

If a signal is found in the cut data, then to calculate the flux we need a procedure for estimating the number of gamma-rays in the uncut sample. One way of doing this is to use the definition of the quality factor (equation 4.3) and the top graph of figure 5.18. The number of gamma-rays and cosmic rays in the cut data can

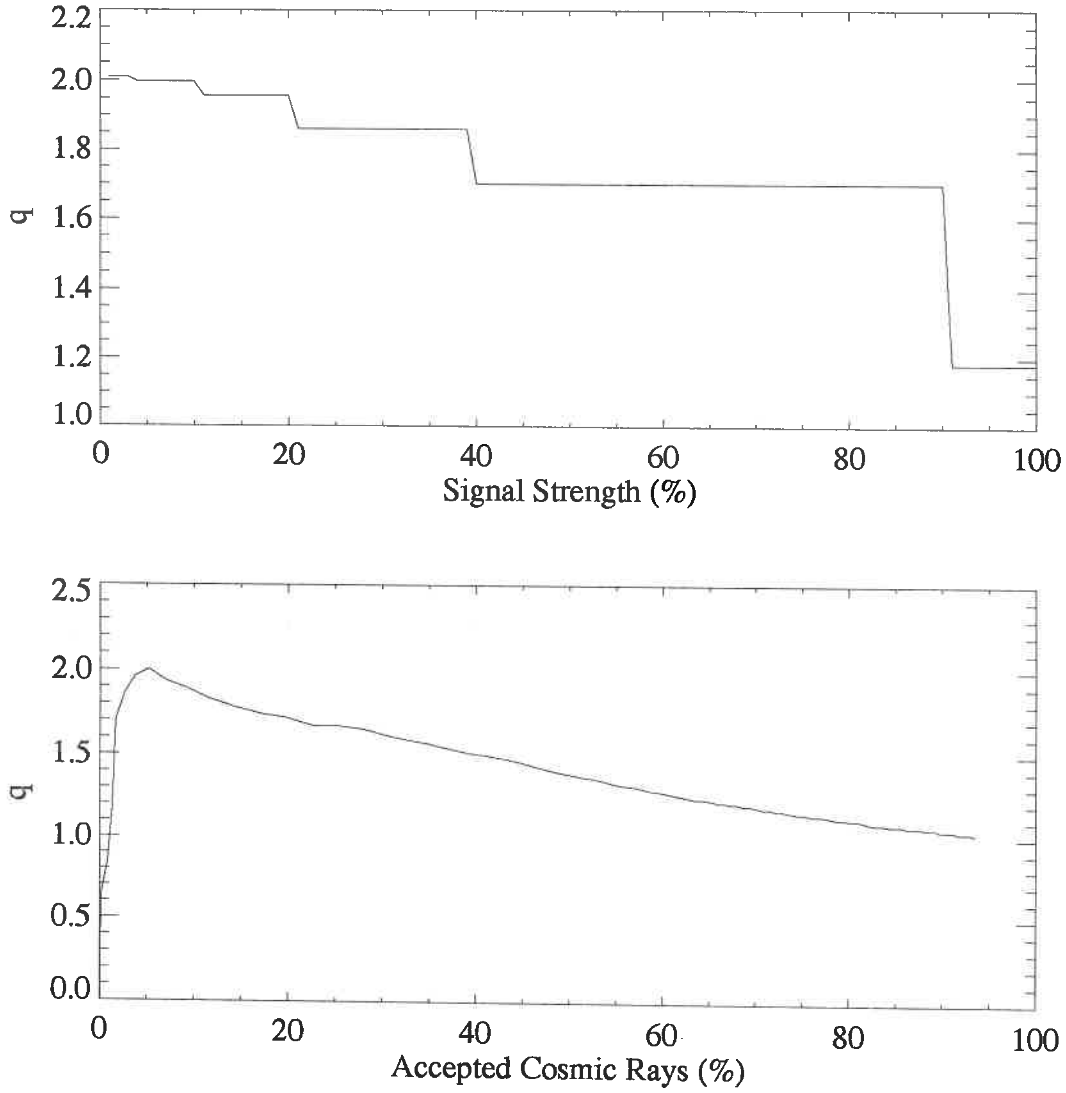

Figure 5.18: Quality factor (q) versus the percentage of gamma-rays in a data sample, where 100% represents equal number of gamma-rays and cosmic rays (top) (see text for more details). The steps in the graph are due to the binning (in 0.1 ns bins) of the rise-time parameter distribution. The variation in q with the percentage of accepted cosmic rays (bottom) is also shown. The q values for the bottom graph assume that the gamma-ray content of the sample is small. Both graphs are for the rise-time cut on Monte Carlo data at 65° from zenith

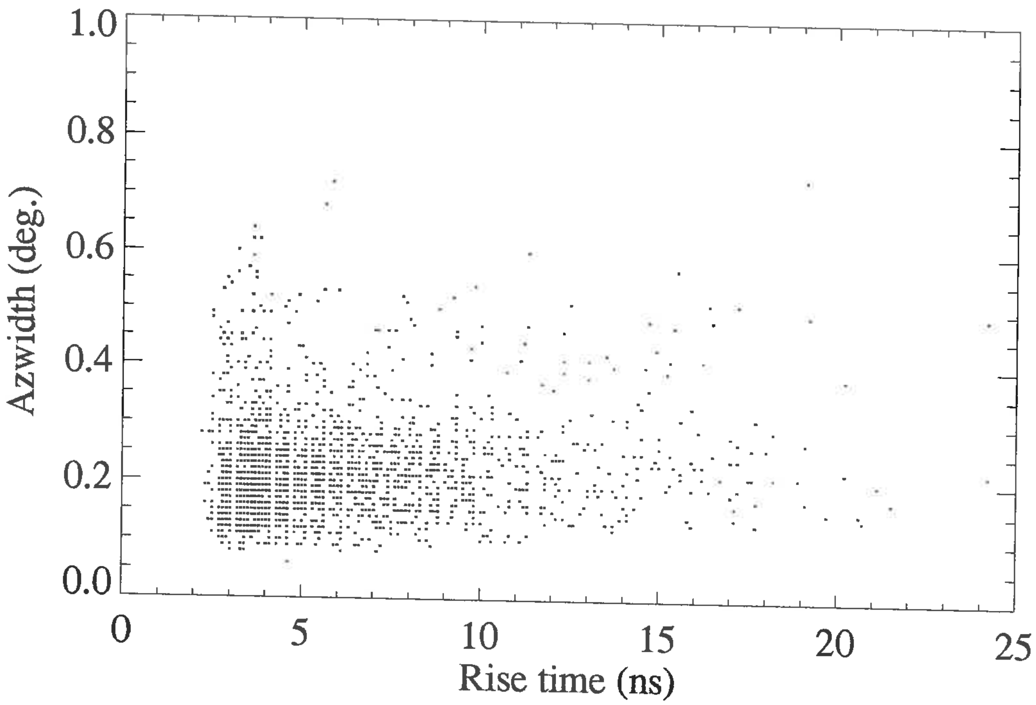

Figure 5.19: Scatter plot of rise-time against azwidth for a file taken at approximately 65° from zenith.

be found by calculating the signal strength from the value of the test statistic and the assumed shape of the light curve of the source. The value of the quality factor can then be calculated as a function of the percentage of gamma-rays in the uncut data. The correct combination of q and gamma-ray percentage should be consistent with the top graph of figure 5.18. Figure 5.18 is only valid for one value of the rise-time cut. If another value is used this graph must be re-calculated from the Monte Carlo simulations.

5.7 Combined Camera and Pulse Profile Cuts

At the present time the determination of the parameter cuts for the camera is not complete. When it is, it will be possible to enhance the sensitivity of the Woomera telescope by combining pulse profile and camera cuts. The value of combining the cuts will depend largely upon how independent the camera and pulse cuts are. Figure 5.19 shows a scatter plot of the rise-time parameter versus the camera "azwidth" parameter for data taken with the Woomera telescope at 65° from zenith. The lack of correlation between the two parameters suggests that a combined pulse profile and camera cut would work better than a pulse profile cut by itself. Any gamma-rays should lie in the bottom left hand corner of figure 5.19. Typically gamma-ray events would have rise-times less than 3.0 ns and azwidths less than 0.2°.

Chapter 6

Data Analysis

6.1 Search for a Periodic Signal

A search for VHE gamma-rays from an X-ray binary or radio pulsar will usually rely on the application of some form of time series analysis technique. By looking for a signal that is modulated by the rotational period of a pulsar it is possible to make a more sensitive search for gamma-ray emission than by testing for a DC excess from the source region. In addition, a time series analysis does not require off-source observations to estimate background rates.

In a typical VHE pulsar analysis, recorded events are assigned a pulsar phase ϕ_i ($\in [0,1]$) by folding the event arrival times, t_i, at the pulsar period. The rotation of a pulsar is described by the rotational frequency ν_0, and the frequency derivatives $\dot{\nu}_o$ and $\ddot{\nu}_0$, defined at epoch T_0. The pulsar phase, $\phi(t)$, for an event arriving at time t is given by the fractional part of

$$\phi(t) = \phi_0 + \int_{T_0}^{t} \nu(t)dt \tag{6.1}$$

where ϕ_0 defines the pulsar phase at T_0. Expanding $\nu(t)$ in terms of a Taylor series gives

$$\phi(t) = \phi_0 + \nu_0(t - T_0) + \frac{1}{2}\dot{\nu}_0(t - T_0)^2 + \frac{1}{6}\ddot{\nu}_0(t - T_0)^3 \tag{6.2}$$

Using $P(t) = \frac{1}{\nu(t)}$ this may be written as

$$\phi(t) = \phi_0 + \frac{(t - T_0)}{P_0} - \frac{1}{2}\frac{(t - T_0)^2}{P_0^2}\dot{P}_0 + \frac{1}{6}(t - T_0)^3 \left(2\frac{\dot{P}_0^2}{P_0^3} - \frac{\ddot{P}_0}{P_0^2}\right) \qquad (6.3)$$

Having assigned pulsar phases, we can now test for the presence of a pulsed signal in the data. If the data contain no pulsed component then the pulsar phases will be distributed randomly between 0 and 1. A significant deviation from randomness in the angular distribution of phases would indicate the presence of a pulsed signal.

The search for a periodic signal involves a process known as significance or hypothesis testing. The hypothesis that is tested is known as the null hypothesis H_0. Any other hypothesis is known as the alternative hypothesis H_1. In the context of searching for a periodic signal in data from an air Čerenkov telescope we could define H_0 and H_1 as :

- H_0 : Event arrival times are random and due entirely to background cosmic rays.
- H_1 : Some event arrival times are not random, but modulated by a period associated with the source.

Commonly a test statistic is constructed, and H_0 accepted or rejected in favor of H_1 depending on the value that the test statistic takes when applied to the data available. At VHE energies there are a number of commonly used circular statistics for testing for the presence of a pulsed signal:

Epoch Folding

Epoch folding has been used extensively in VHE and UHE gamma-ray astronomy, although it has fallen out of favor in recent times. Epoch folding involves binning the pulsar phases and testing the uniformity of the resulting distribution using Pearson's χ^2 statistic. If the data are binned into m bins with x_j events in the j^{th} bin then

$$\chi^2 = \sum_{j=1}^{m} \frac{(x_j - \bar{x})}{\sigma_j^2} \tag{6.4}$$

where $\bar{x}$ is the mean number of events per bin and σ_j^2 is the variance associated with x_j. If no pulsed signal is present then the distribution of events will be governed by Poisson statistics ($\sigma_j^2 = \bar{x}$). Equation 6.4 would then be distributed as a χ^2 with (m-1) degrees of freedom (χ^2_{m-1}). A significant pulsed content in the data would lead to a large value of χ^2 with a correspondingly small chance probability.

The epoch folding technique is powerful at detecting narrow phase peaks, but it does have problems associated with the binning process. Unless the light curve of the source is well known the position and number of phase bins cannot be determined a *priori*. A narrow phase peak may be split between bins, reducing the significance of the detection. If the data is re-binned then a statistical penalty is incurred, which also reduces the significance of detection. Additionally, the χ^2 value may underestimate the significance of a result if the number of events per bin is small.

Rayleigh Test

The Rayleigh test was developed for the study of bird migration by Lord Rayleigh (1894). It was first introduced into gamma-ray astronomy by Gibson et al. (1982) and is now used extensively in high energy astrophysics.

The Rayleigh statistic is formed from the addition of unit vectors of angle $2\pi\phi_i$, calculated from pulsar phases ϕ_i. The resultant vector $\bar{R}$ is indicative of the mean direction of the vectors and is given by

$$\bar{R} = \frac{1}{N}\left(\left[\sum_{i=0}^{N-1} \cos(2\pi\phi_i)\right]^2 + \left[\sum_{i=0}^{N-1} \sin(2\pi\phi_i)\right]^2\right)^{\frac{1}{2}} \tag{6.5}$$

where N is the number of events. A small value of $\bar{R}$ indicates that the phases are uniformly distributed, while a large value of $\bar{R}$ is indicative of the presence of a pulsed signal. If the number of events is large (>100) then $2N\bar{R}^2$ is distributed as χ_2^2, and so the probability of obtaining a particular value of $2N\bar{R}^2$ is given by

$$Pr(\geq 2N\bar{R}^2|H_0) = \exp(-N\bar{R}^2) \tag{6.6}$$

For a small number of events the probability may be calculated from

$$Pr(\geq \Gamma | H_0) = \exp(-\Gamma)(1 + A - B - C) \tag{6.7}$$

where

$$\begin{aligned}
A &= \frac{(2\Gamma - \Gamma^2)}{4N} \\
B &= \frac{(24\Gamma - 132\Gamma^2 + 76\Gamma^3 - 9\Gamma^4)}{288N^2} \\
C &= \frac{(1440\Gamma + 1440\Gamma^2 - 8280\Gamma^3 + 4890\Gamma^4 - 870\Gamma^5 + 45\Gamma^6)}{17280N^3} \\
\text{and } \Gamma &= N\bar{R}^2
\end{aligned}$$

Greenwood and Durrand (1955)

The Rayleigh statistic is most sensitive to broad sinusoidal light curves and less sensitive to narrower light curves. It can also be very insensitive to multiple phase peak light curves. In the extreme case, where the light curve has two equal intensity peaks separated by 0.5 in phase, the Rayleigh statistic has no sensitivity. In this case the vectors from each peak cancel, giving a small Rayleigh test value despite the presence of even a strong pulsed signal. It would be advantageous, in this situation, to have available a test statistic that allows for higher harmonic content than the fundamental.

Z_m^2 Test

The Z_m^2 test is an extension of the Rayleigh test. Z_m^2 is defined by

$$Z_m^2 = \frac{2}{N}\sum_{j=1}^{m}\left(\left[\sum_{i=0}^{N-1} cos(2\pi j \phi_i)\right]^2 + \left[\sum_{i=0}^{N-1} sin(2\pi j \phi_i)\right]^2\right) \tag{6.8}$$

where N is the number of events. It can be seen that the Z_m^2 test is simply the summation of twice the Rayleigh power evaluated for m harmonics. If $\bar{R}_j^2$ is the Rayleigh statistic evaluated at the j^{th} harmonic then

$$Z_m^2 = \sum_{j=1}^{m} 2N\bar{R}_j^2 \tag{6.9}$$

The chance probability of obtaining a value of Z_m^2 is given by

$$Pr(\geq Z_m^2|H_0) = \exp\left(\frac{-Z_m^2}{2}\right) \sum_{k=0}^{m-1} \frac{(Z_m^2)^k}{2^k k!} \tag{6.10}$$

Bevington (1969)

If the number of events is small then the probability may be calculated by using equation 6.7 (de Jager 1987). If we define α_j as the individual chance probabilities for obtaining the m values of $2N\bar{R}_j^2$, then the α_j can be combined to form a new test statistic, β say, where

$$\beta = -2\sum_{j=1}^{m} \ln\alpha_j \tag{6.11}$$

and β is distributed as χ^2_{2m}.

When using a Z_m^2 statistic it is necessary to decide upon the value of m best suited to the source being studied. The Z_1^2 (Rayleigh test) is most suited to detecting broad phase peaks. The Z_2^2, while slightly less powerful at detecting broad peaks than the Z_1^2, is more powerful at detecting narrower phase peaks (Nagle et al. 1988). For this reason the Z_2^2 test has been widely used for gamma-ray detection at both satellite and VHE energies. If the phase peak is very narrow, such as that seen often at UHE energies where emission is modulated by the orbital period of a binary system, then the Z_{10}^2 is commonly used.

Protheroe Test

The Protheroe test (Protheroe 1985) was developed specifically for use in VHE and UHE gamma-ray astronomy. The Protheroe statistic, Υ_N, is defined as

$$\Upsilon_N = \frac{2}{N(N-1)} \sum_{i=1}^{N-1} \sum_{j=i+1}^{N} \left(\Delta_{ij} + \frac{1}{N}\right)^{-1} \tag{6.12}$$

where N is the number of events and Δ_{ij} is the phase separation between ϕ_i and ϕ_j, given by

$$\Delta_{ij} = 0.5 - |[|(\phi_i - \phi_j)| - 0.5]| \tag{6.13}$$

The probability for obtaining a given Υ_N must be determined by Monte Carlo simulation. The computing time to calculate Υ_N scales as N^2 which limits the usefulness of the Protheroe test to samples containing small numbers of events.

The Protheroe test was designed to detect narrow phase peaks. It has been used mainly for UHE gamma-ray detection from binary systems.

6.1.1 Searching a Range of Periods

When using circular statistics to detect gamma-ray emission from pulsars it is not usually possible to look at just a single period. It is more often the case that a search must be made over a range of periods. The need for this arises from a number of factors :

- Lack of knowledge of the pulsar parameters can lead to an uncertainty in the extrapolation of the pulsar period to the epoch of observation.
- The pulsar period may vary unpredictably on short time scales due to rapid spin up or spin down.
- The detected pulsar period may differ from the actual pulsar period because of statistical limitations. This can arise from sampling effects if the data sample or signal are too small.
- The period of gamma-ray emission may differ from the period of the pulsar. An example of this is Hercules X-1, where gamma-ray emission has been reported at periods shifted from the true pulsar period.

To overcome these problems it is often necessary to search over a range of periods, P_1 to P_2, around the region of interest. Such a search involves the calculation of a circular statistic at discrete points between P_1 and P_2.

Searching a large range of periods gives a greater probability of finding an apparently significant result by chance. It is therefore necessary to estimate the number of independent trials associated with a period search by calculating the number of independent period spacings (IPS).

From Fourier theory it is known that in a data sample of duration T, statistically independent frequencies are separated by $\Delta\nu = \frac{1}{T}$. The number of statistically independent periods, M, in the range P_1 to P_2 is given by

$$\begin{aligned} M &= T\left(\frac{1}{P_1} - \frac{1}{P_2}\right) \\ &= \frac{T(P_2 - P_1)}{P_1 P_2} \end{aligned} \tag{6.14}$$

The distance between independent periods, IPS, is then

$$\Delta P = \frac{P_1 P_2}{T} \tag{6.15}$$

Now consider a period search on M independent periods, which yields a maximum test statistic value S_{max}. If the chance probability of S_{max} is p then the probability of finding p within the range of periods searched is

$$Pr(> S_{max}|H_0) = 1 - (1 - p)^M \tag{6.16}$$

In VHE gamma-ray astronomy, where detections are often marginal, it is clearly advantageous to search over as small a range of periods as possible.

It is usual, when searching a range of periods, to calculate the value of a test statistic at intervals less than the independent period spacing. This practice is known as oversampling, and ensures that close to the maximum value of the test statistic is found. When estimating the chance probability of obtaining a test statistic value, the oversampling must be allowed for.

Equation 6.16 tends to underestimate the true chance probability when oversampling is used. De Jager (1987) describes a Monte Carlo method for calculating this factor of underestimation. An alternative method is to calculate the distribution of test statistic values for a "background" consisting of a large range of periods near the on-source period search region. If the same oversampling is used for the background and on-source period regions then the chance probability may be

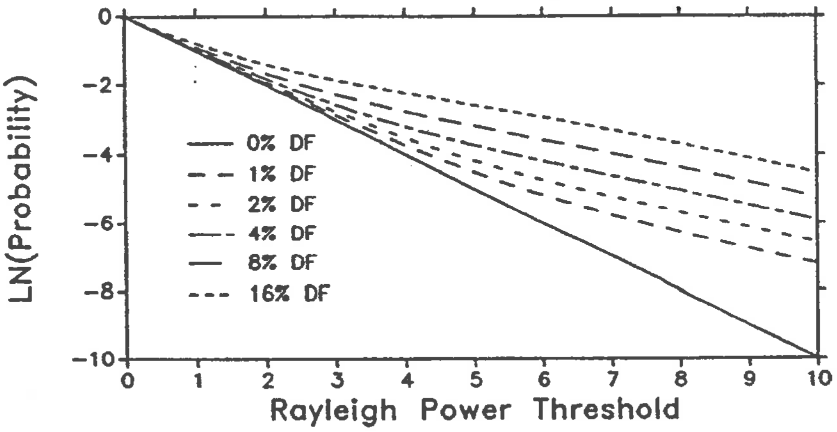

Figure 6.1: Plot of cumulative distributions of Rayleigh powers for various source duty factors (from Lewis 1990).

found directly from the background distribution of test statistic values. From here on the period range covering the source search region will be referred to as the "on-period" region. The period range used to estimate the background distribution of test statistic values will be referred to as the "off-period" region.

6.1.2 Testing Rayleigh Power Distributions

It is possible to analyze a set of observations by looking at the distribution of all Rayleigh powers in the data rather than just the largest Rayleigh powers. The following method has been suggested by Lewis (1990). The data are divided into segments of approximately uniform size. The distribution of powers in the on-period and off-period regions for all segments are then found. The off-period region can be made very large so that the background power distribution is well determined. To avoid binning problems cumulative rather than differential distributions are used.

If a signal is present then the distributions of powers for the on-period and off-period regions will differ. Figure 6.1 shows the difference between on-period and off-period Rayleigh power distributions for various source duty factors. Figure 6.1 assumes a sinusoidal light curve with 283 signal events in a total sample of 5000.

There are a number of statistical tests for determining the significance of the difference between cumulative distributions (Eadie et al. 1971). Lewis also suggests the use of a Fisher test (Fisher 1958, Eadie et al. 1971). If the chance probability for obtaining a Rayleigh power P_i in segment i is h_i when no signal is present then the test statistic H_f is given by

$$H_f = -2\ln\left[\prod_{i=1}^{N_t} h_i\right] \tag{6.17}$$

H_f is distributed as χ^2 with $2N_t$ degrees of freedom, where N_t is the number of data segments multiplied by the number of independent periods in the on-period search region. Normally the probabilities h_i would be found directly from the off-period distribution of powers.

6.2 Hercules X-1 Observations

6.2.1 1992 Data Set

During the 1992 observing season a total of ten observations were made of Hercules X-1 (see table 6.1) . This does not include data files that were not analyzable because of cloud cover or equipment failure or observations taken without pulse shape information being recorded. Normal observation did not include off-source scans, although some off-source runs were made to check systematic effects. Of the ten on-source runs, three included coverage of the nominal eclipse ingress of Her X-1 (j8799a, j8804b, j8833b). There were also three files (j8806c, j8857a, j8801b) taken around eclipse egress.

All files collected were analyzed in the same way. The arrival times for each file were binned into five minute intervals to test for the presence of cloud. Distributions of pulse parameters for the uncut data were generated to test for any problems associated with the pulse profile measurement system. The files, containing the arrival times and pulse parameters for each event, were then edited to include only those events within the range of orbital phases of interest. Pulse parameter cuts were then applied to these files. For the 1992 data a pulse height cut was applied so that the largest 50% of pulses were retained. Of these events the pulses with the fastest 10% rise-times were accepted for analysis. The values of the parameter cuts were made *a priori* and are consistent with the cuts derived in section 5.5. The files were

Julian Day	Time (UT)	Duration (s)	Orbital phase	35 Day Phase
j8799a^i	10:26-16:38	22320	0.896-0.047	0.05
j8803a	10:48-15:41	24780	0.257-0.377	0.16
j8804b^i	10:33-16:13	20400	0.839-0.978	0.19
j8806a	13:06-14:07	3660	0.490-0.515	0.22
j8806c^e	11:06-14:45	10899	0.029-0.118	0.24
j8829a	10:58-11:45	2820	0.554-0.573	0.91
j8857a^e	10:39-11:49	4200	0.015-0.044	0.71
j8797a	11:38-16:20	16920	0.749-0.864	0.99
j8801b^e	10:18-16:18	21600	0.069-0.216	0.11
j8833b^i	11:20-13:56	9360	0.915-0.979	0.02

Table 6.1: Hercules X-1 data files taken during 1992. The number of the file indicates the Truncated Julian Day at the beginning of the file. The letter after the JD is to identify files taken on the same day. The superscripts i and e indicate files including eclipse ingress and egress respectively.

separated into three groups for period analysis: eclipse ingress files, eclipse egress files and other files. These three groups were analyzed independently because of the possibility of different gamma-ray production mechanisms for each group.

Earth to solar system barycentre reduction was approximated by a six term trigonometric series based on the mean orbits of the earth and the four major planets (Deeter et al. 1981). This approximation is expected to be accurate to better than 0.2s until the year 2000. Tests using the JPL DE 200 ephemeris (Standish 1982) have confirmed that this approximation is sufficiently accurate for our analysis of Her X-1. Source barycentering was calculated assuming a circular orbit for Her X-1 with a.sin(i)=13.181 light s. As I have been unable to obtain contemporaneous measurements of the 35 day phase it was calculated from the ephemeris of Ögelman (1987), extrapolated to produce the measured 35 day phases of more recent x-ray measurements (Mihara et al. 1991). As a result there is some uncertainty in the 35 day phase.

6.2.1.1 Eclipse Ingress

From 1990 to 1992 a total of 75 nights observation were made of Her X-1 before the pulse shape measurement system was installed. An analysis of these data with the Z_1^2 statistic at the X-ray pulsar period was performed. The powers were consistent with a random distribution. The largest power found (1% chance probability) included eclipse ingress, and so this data (April 29 1992) was analyzed in more detail. This observation lasted 320 minutes covering the orbital phases 0.877 to 0.007. A 60 minute sliding window showed that the largest contribution to the Rayleigh power occurred during the hour centered on eclipse ingress (orbital phase 0.93). Based on this analysis a 120 minute window centered on eclipse ingress was defined as a nominal *a priori* region of interest for other observations. This region of interest covers the orbital phases 0.907 to 0.955.

Of the three eclipse ingress files taken in 1992 with the pulse measurement system only j8804b (July 1) was taken under ideal conditions. The file taken on June 26 (j8799a) was affected by changing amounts of light cloud cover during parts of the run. On July 30 (j8833b) heavy cloud was present, leaving only 50 minutes (orbital phases 0.928 to 0.949) of analyzable data.

After pulse parameter cuts a total of 46 events were left in file j8799a, 124 events in j8804b and 41 events in j8833b. The values of the Z_1^2 statistic were calculated for each file for the period range 1.236s to 1.240s. The period range is approximately ±0.3% of the pulsar period, the same range used by the Whipple group in its analysis of Her X-1 (Reynolds et al. 1991). The results of these Rayleigh tests are shown in figure 6.2. Both j8799a and j8804b show large Rayleigh powers at a period of 1.2371s, which is blue-shifted from the pulsar period of Her X-1 by 0.052%. For the same files without pulse parameter cuts, or just the pulse height cut, there are no significant Rayleigh powers at this period. The file j8833b shows no significant Rayleigh power at 1.2371s even after pulse parameter cuts. The distribution of pulsar phases at 1.2371s for the three ingress files are shown in figure 6.3. In the phaseogram of j8833b there is some indication of the presence of a double peaked structure. Given the X-ray behavior of Her X-1 (see section 1.5) it is possible that gamma-ray emission may also occur at the second harmonic of the pulsar period. Figure 6.4 shows the values of the Z_1^2 statistic for the range ±0.3% around the second harmonic of the pulsar period. This figure shows that the file j8833b has Rayleigh power peak near the second harmonic of 1.2371s.

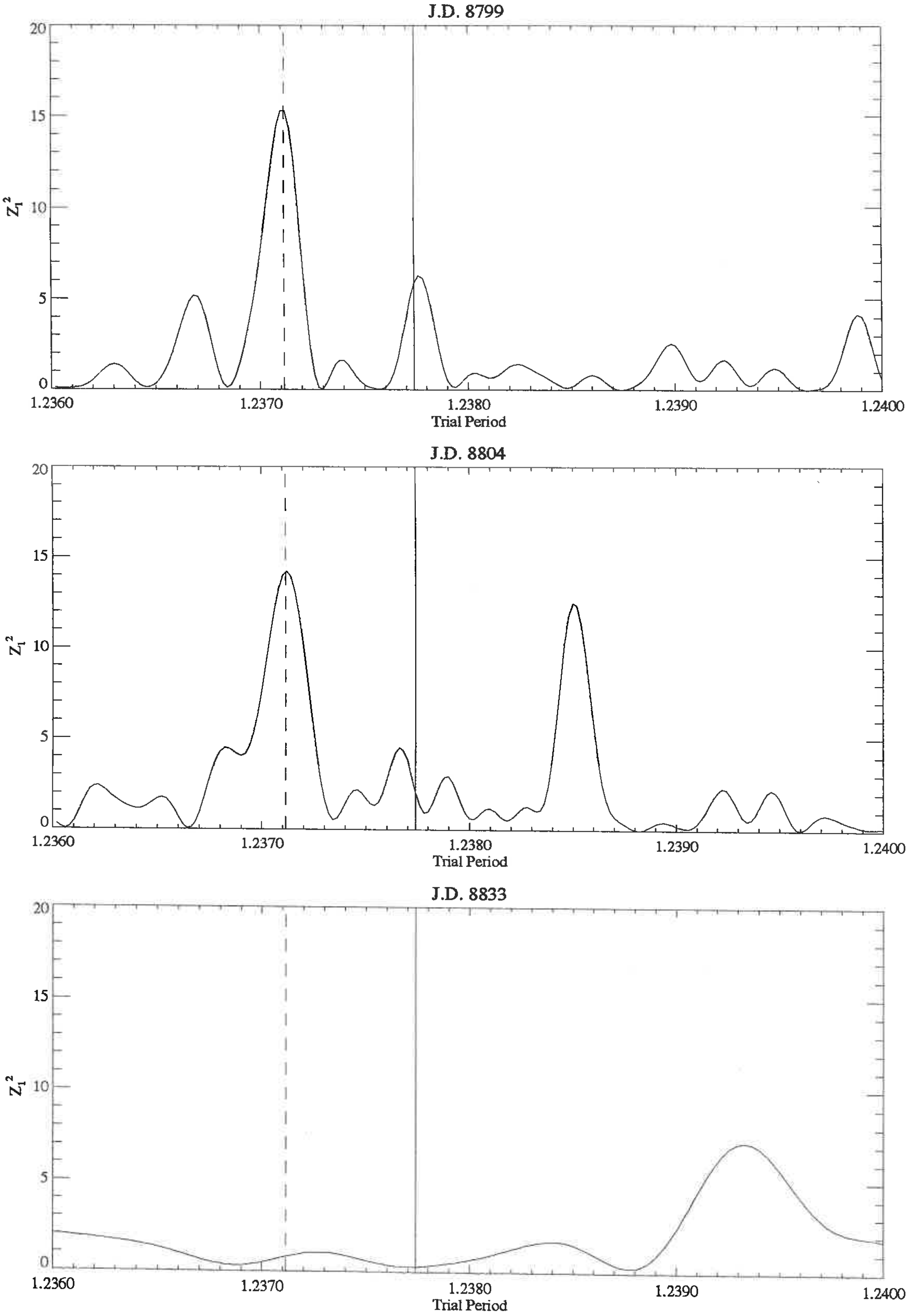

Figure 6.2: The Z_1^2 statistic as a function of period around the first harmonic of the x-ray period. The solid line indicates the value of the x-ray period (1.23774s). The dashed line is at a period of 1.237115 s.

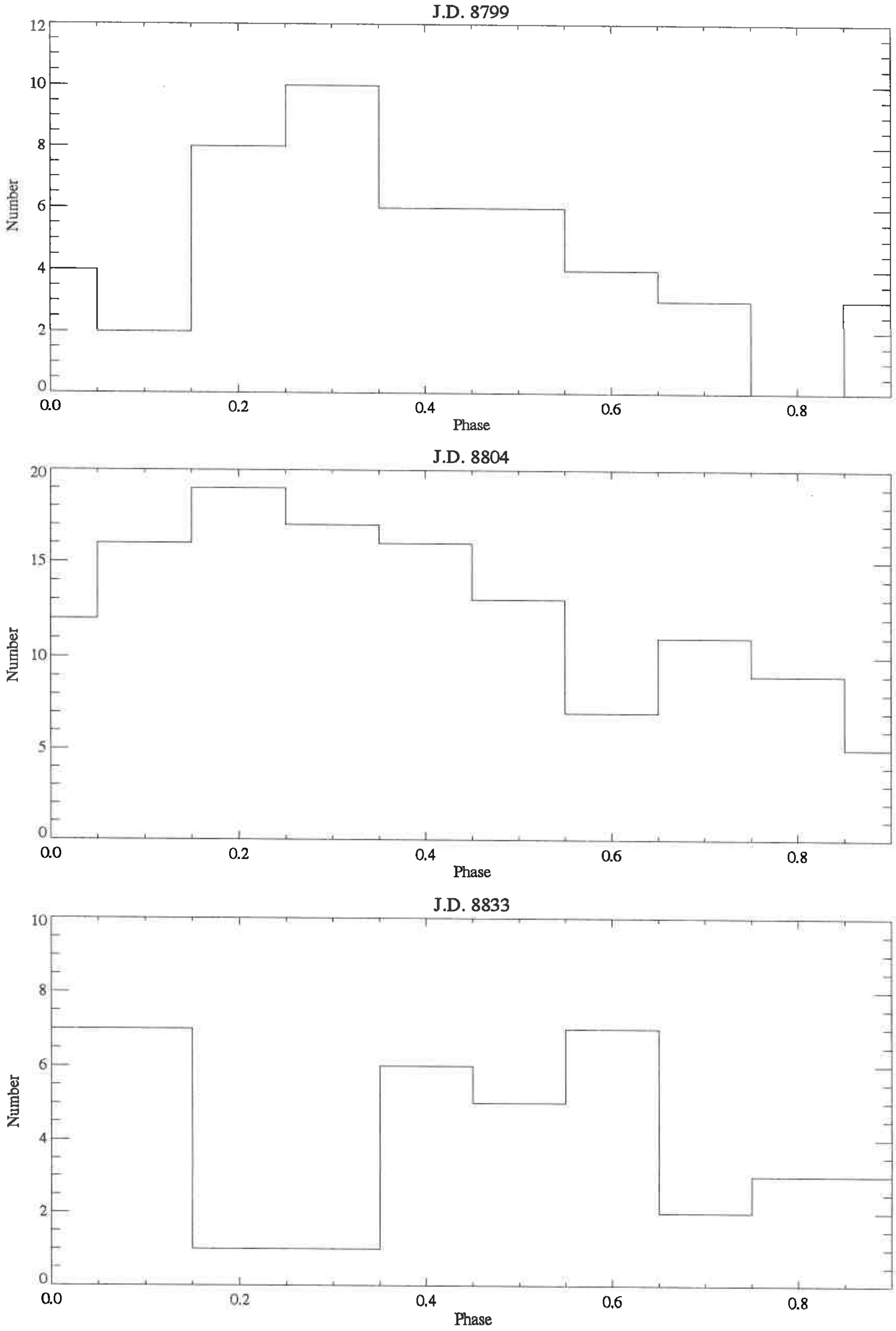

Figure 6.3: The distribution of pulsar phases at a period of 1.237115s for the three eclipse ingress files (arbitrary T0).

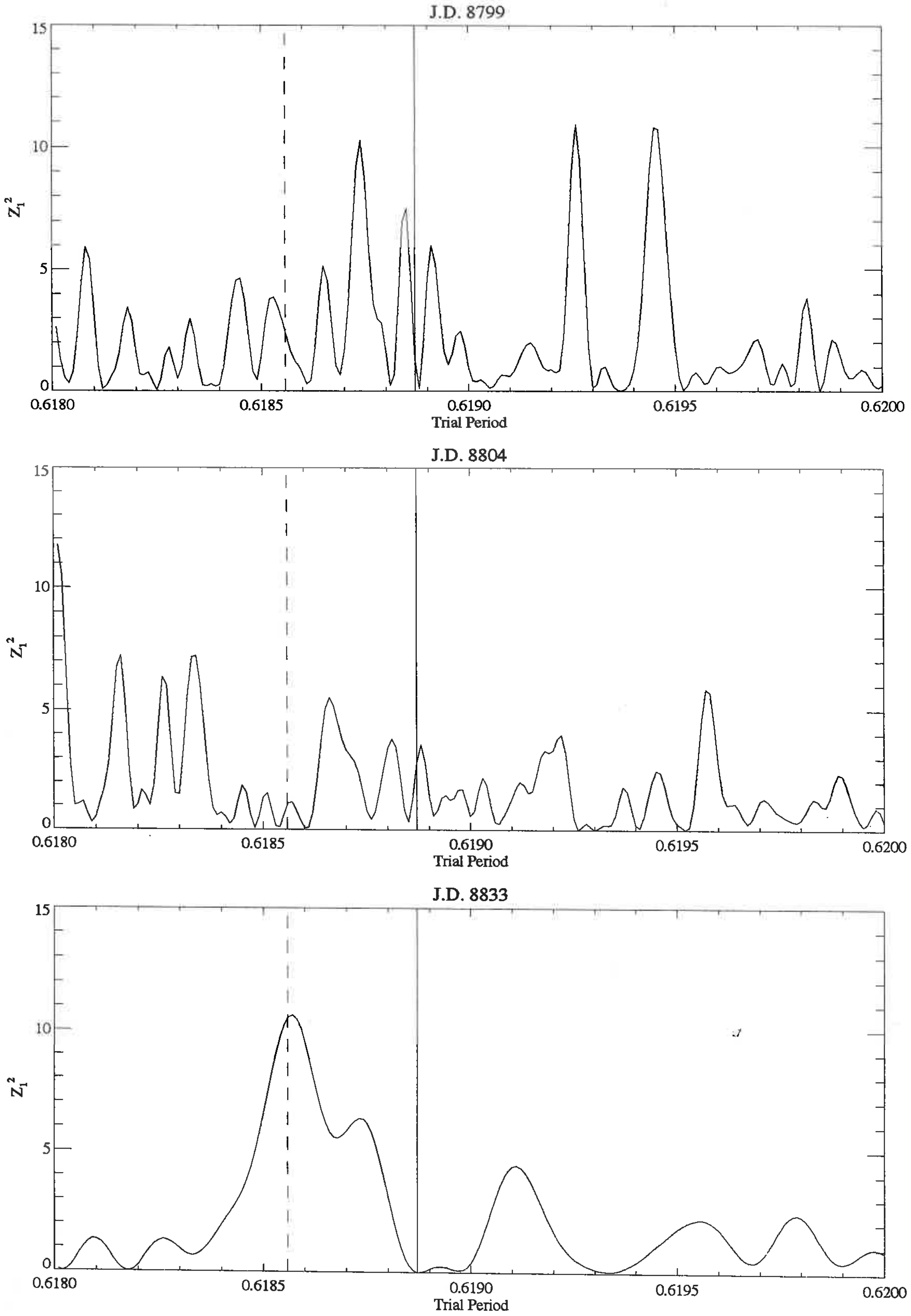

Figure 6.4: The Z_1^2 statistic as a function of period around the second harmonic of the x-ray period. The solid line indicates the value of the second harmonic of the x-ray period (1.23774s). The dashed line is at the second harmonic of 1.237115 s.

To estimate the final significance of the Rayleigh powers at 1.2371s the separate probabilities for the significant Rayleigh powers on each night were combined. The probability of obtaining a value of Z_1^2 was estimated statistically for each file. The distribution of powers for each file was found for periods between the first and second harmonics of the signal search region. The chance probability was then found directly from these distributions. This method accounts for effects such as oversampling in the period analysis. The chance probabilities for the powers in files j8799a and j8804b were found to be 1.15×10^{-3} and 2.02×10^{-3} respectively. For j8833b the power at the second harmonic corresponded to a chance probability of 1.6×10^{-2}. Combining these through

$$P_{12} = P_1 P_2 (1 - \ln P_1 P_2) \tag{6.18}$$

yielded a total chance probability of 8.03×10^{-6}. After allowing for the number of independent periods searched and a factor of two for searching both first and second harmonics the final chance probability is 1.35×10^{-4}.

Assuming that the gamma-ray light curve of Her X-1 is sinusoidal we can calculate the percentage of the events in each of the files that are pulsed at 1.2371s (table 6.2). It is now possible to estimate the flux of gamma-rays from Her X-1 using the Monte Carlo simulations previously discussed (section 3.4). The duration of the three ingress files and the numbers of events passing cuts were quoted previously. It is clear from these numbers that the triggering rate of the file j8799a is much less than that of the other two ingress files. I will firstly calculate the gamma-ray fluxes for the files j8804b and j8833b, and return to the file j8799a later.

Firstly we must estimate the increase in threshold of the observation due to the 50% pulse maximum cut. If we assume that the majority of the events in the uncut file are from cosmic ray EAS then the increase in threshold energy with the 50% pulse maximum cut will depend largely upon the spectral index of the primary cosmic rays. Using this assumption increases the gamma-ray threshold of the telescope at Her X-1 elevations to 27 TeV. The gamma-ray flux may now be calculated using Monte Carlo simulations to find the collecting area and triggering efficiency of the telescope to gamma-rays. It is also necessary to estimate what

File	Pulsed Fraction (%)	Flux $\times 10^{-12}$($cm^{-2}s^{-1}$)	Lumin. $\times 10^{35}$ (erg s^{-1})
j8799a	76 ± 21	(> 49TeV) 2.5 ± 0.8	14.7
		(> 27TeV) 4.8 ± 1.5	15.2
j8804b	44 ± 13	(> 27TeV) 2.4 ± 0.8	7.8
j8833b	65 ± 22	(> 27TeV) 3.8 ± 1.3	11.9

Table 6.2: Average pulsed fraction, flux and source luminosity for the three ingress files taken during 1992.

percentage of the gamma-rays pass the pulse shape rise-time cut ($\sim 40\%$). This number was obtained by the method described in section 5.6. For all of these calculations the integral power law spectral index of the gamma-rays was chosen to be -1.1. Assuming that Her X-1 lies 5.8kpc from us we can also calculate the luminosity above 27 TeV, assuming that the gamma-rays are emitted isotropically. The calculated fluxes and luminosities for the files j8804b and j8833b are given in table 6.2. The errors quoted for the flux are the statistical errors associated with estimating the signal strength. They do not include the errors in estimating the gamma-ray threshold and collecting area. Effects due to the changing zenith angle of observation and the presence of cloud are also ignored.

Now consider the file j8799a. The lower triggering rate of this file is most probably due to the presence of changing amounts of light cloud during the observation. I will calculate the flux of gamma-rays from this observation by assuming that the decrease in rates is due to a uniform increase in energy threshold throughout the file. Using this assumption raises the threshold of observation from 27TeV to 49TeV. The flux and luminosity may now be calculated as discussed previously. It is assumed that the higher energy showers, when viewed through cloud, exhibit the same triggering efficiency and collecting area that was used for the other ingress files. It is also assumed that the rise-time cut behaves in the same way. The flux and luminosity above 49TeV for j8799a are shown in table 6.2. If an integral gamma-ray spectrum of -1.1 is assumed then the flux and luminostiy may be extrapolated back to a threshold of 27TeV. These numbers are also shown in table 6.2.

We will now look at one of the ingress files, j8804b, in more detail. J8804b is the only file unaffected by cloud that covers the entire region of interest around eclipse ingress. Figure 6.5 shows a 1 hour wide bin sliding through the file after parameter cuts have been made, indicating the chance probability at 1.2371s as a function of orbital phase. The peak of emission lies at orbital phase 0.937, which is some 12 minutes after the onset of eclipse. There is some uncertainty in the orbital position of peak emission because of poor statistics and the fact that a one hour wide bin is used. Figure 6.5 seems to indicate that the signal extends until at least half an hour beyond the start of eclipse. Figure 6.5 also indicates that there is some emission well before the onset of eclipse.

6.2.1.2 Eclipse Egress

The three eclipse egress files were prepared in the same way as the ingress files. Where possible, files were adjusted to contain events within one hour either side of eclipse egress. The files were analyzed separately with the Z_1^2 test for periods ±0.3% around the first and second harmonics of the x-ray period of Her X-1. This analysis

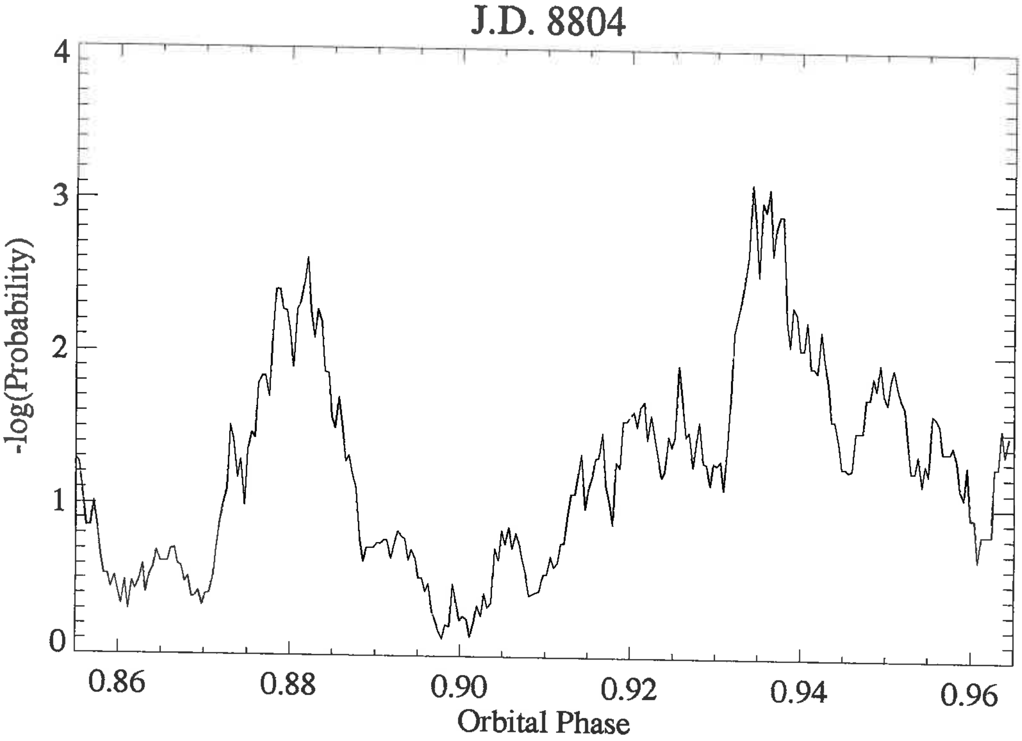

Figure 6.5: The chance probability in a 1 hour wide sliding bin passed through file j8804b at a period of 1.2371s.

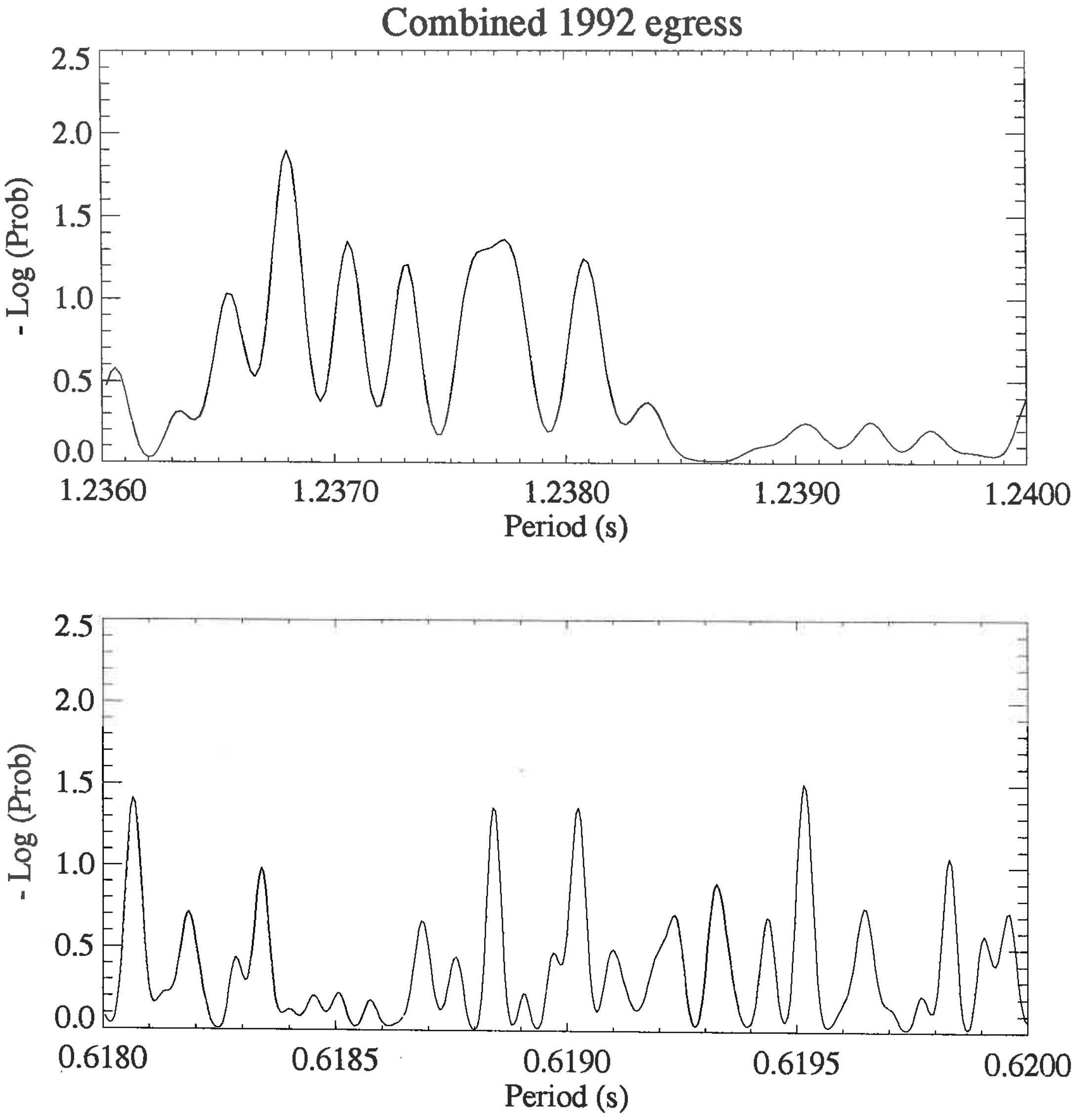

Figure 6.6: Nominal chance probability versus period for the three 1992 eclipse egress files. The Rayleigh powers have been added incoherently and analyzed as Z_3^2.

showed no evidence of statistically unlikely Z_1^2 values within these files. Figure 6.6 shows the nominal probability versus period for the three files added incoherently at the first and second harmonics. If m Z_1^2 values are added then the resulting test statistic will be distributed as Z_m^2. After trials are accounted for none of the peaks in figure 6.6 are statistically significant.

6.2.1.3 Other Orbital Phases

The files containing data at orbital phases other than ingress or egress were truncated to two hours length. Rayleigh tests were performed for each file for periods ±0.3% around the first and second harmonics of the X-ray period. No statistically unlikely peaks were seen in any of the files. Figure 6.7 shows the nominal chance probability versus period for the four files added incoherently.

6.2.2 1993 Data Set

During the 1993 observing season a total of 11 analyzable runs were recorded from Her X-1. These runs, listed in table 6.3, include five eclipse ingress and four eclipse egress observations. The data were prepared and analyzed in the same way as the 1992 data set. The increased energy threshold of the Woomera telescope, due to the installation of a camera system, meant that the 25 photoelectron pulse maximum cut now accepted 60% of raw events.

As with the 1992 data set eclipse ingress, egress and other orbital phases were treated separately. Data files around eclipse transition included, where possible, an hour either side of nominal x-ray eclipse transition. Files at other orbital phases were split or truncated to a similar length.

6.2.2.1 Eclipse Ingress

The five eclipse ingress files were analyzed using the Z_1^2 statistic for periods of ±0.3% around the first and second harmonics of the x-ray period. The results of this are shown in figures 6.8 and 6.9. These plots do not show any indications of pulsed

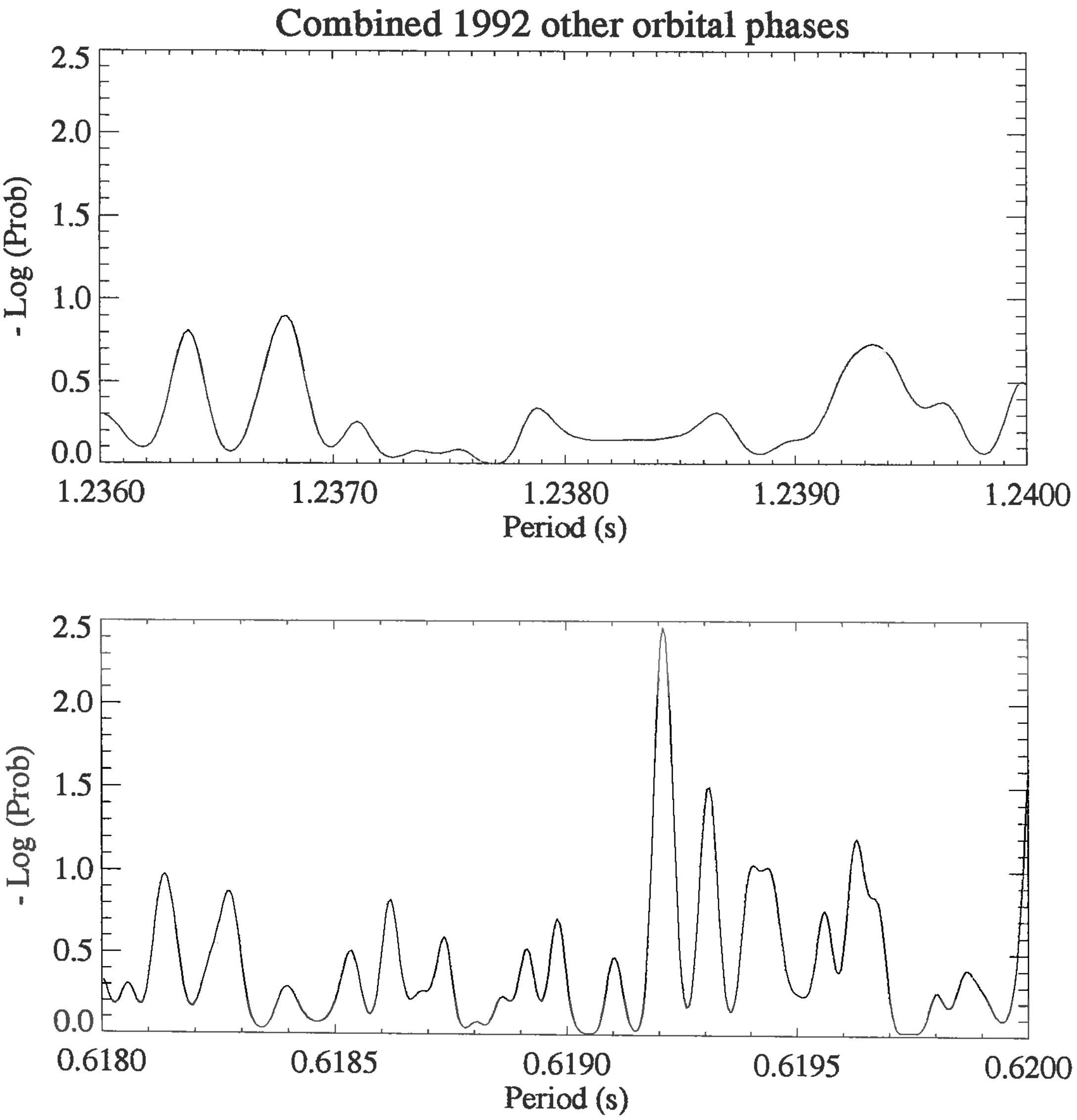

Figure 6.7: Nominal chance probability versus period for the four files that did not include eclipse ingress or egress. Rayleigh powers have been added incoherently and analyzed as Z_4^2.

emission from Her X-1 at a fixed period.

The least likely peak in the 1993 ingress data occurred on JD 9104 (April 27) at a period of 1.23644s. Figure 6.10 shows how the strength of this peak changes with orbital phase. Unfortunately, due to the setting of the source, figure 6.10 does not include the orbital phase of peak significance for the 1992 ingress file j8804b. If only the orbital phases 0.87-0.92 of j9104a are analyzed then the significance of this peak increases to $\sim 10^{-4}$. This is not statistically significant when the number of trials are allowed for. The trials would include the number of independent periods

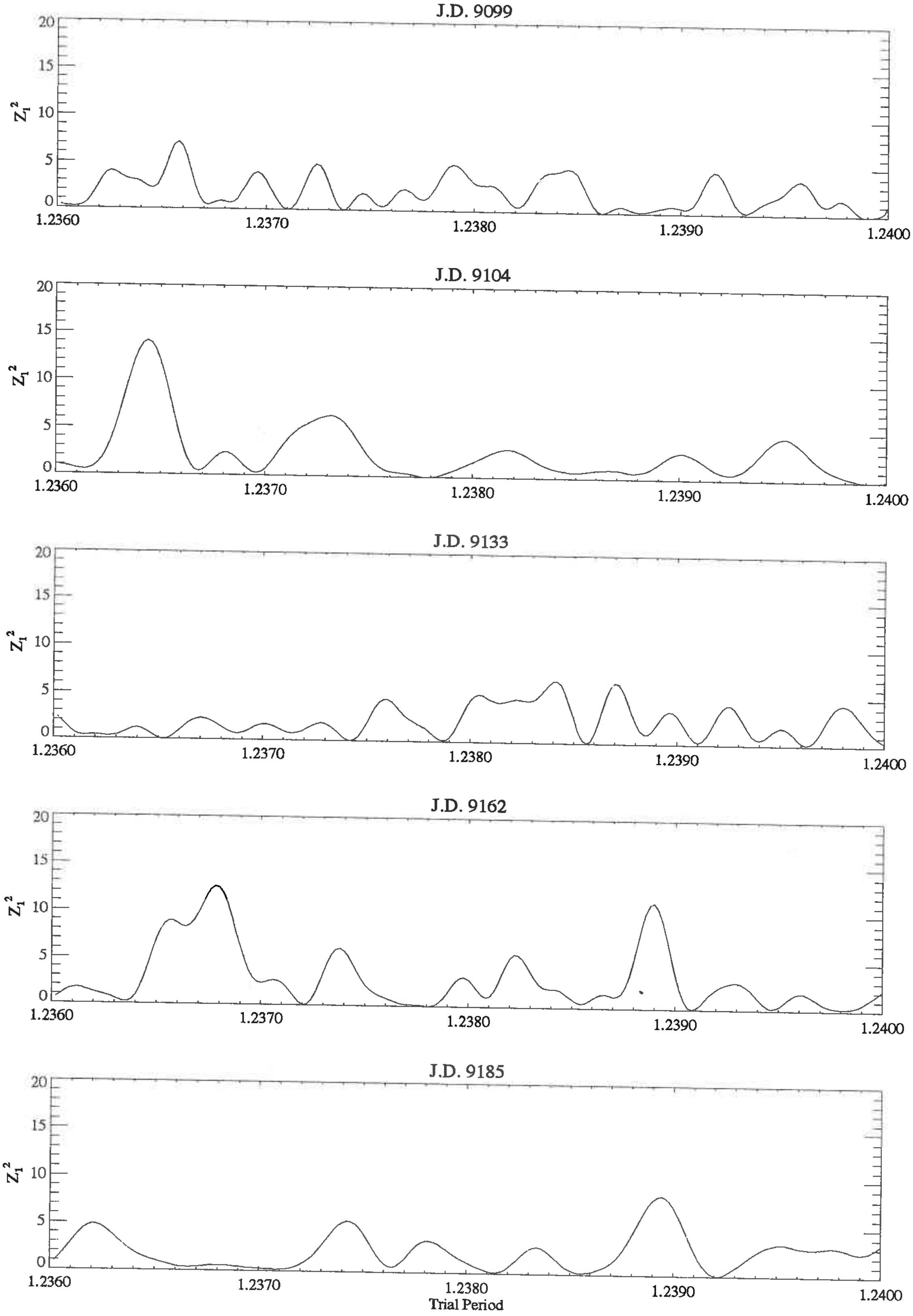

Figure 6.8: The value of the Z_1^2 statistic as a function of period for the 1993 ingress files around the first harmonic of the x-ray period.

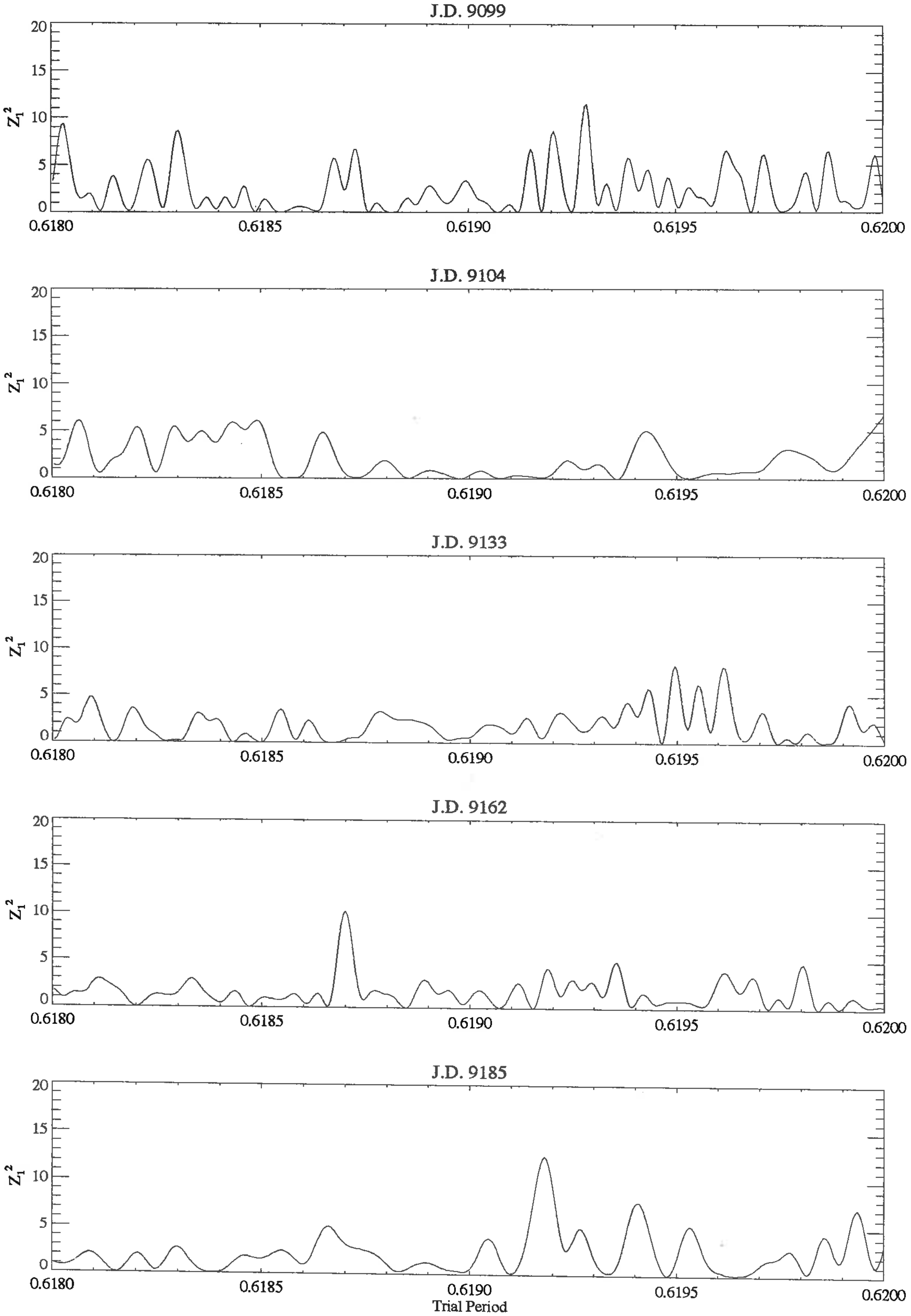

Figure 6.9: The value of the Z_1^2 statistic as a function of period for the 1993 ingress files around the second harmonic of the x-ray period.

Julian Day	Time (UT)	Duration (s)	Orbital phase	35 Day Phase
j9099b^{i}	15:26-18:45	11940	0.883-0.964	0.59
j9101a^{e}	14:53-18:58	14100	0.046-0.146	0.65
j9104a^{i}	14:58-20:02	18240	0.813-0.937	0.73
j9106a^{e}	15:32-18:39	11220	0.003-0.479	0.79
j9132b	13:15-17:59	17040	0.240-0.355	0.53
j9133b^{i}	13:21-18:15	17640	0.830-0.950	0.56
j9134d	13:39-17:53	15240	0.426-0.529	0.59
j9135b^{e}	13:48-17:49	14460	0.017-0.116	0.62
j9162a^{i}	12:10-16:16	14760	0.858-0.959	0.39
j9180a^{e}	11:36-14:08	9120	0.02-0.082	0.93
j9185b^{i}	9:41-13:27	13560	0.914-0.006	0.08

Table 6.3: Hercules X-1 files taken during 1993. The file labeling system is the same as for the 1992 data.

searched, the oversampling, the number of other ingress files analyzed and a penalty for truncating the data to give the most significant result. Figure 6.11 shows an orbital phase vs. significance scan for the second most significant peak in the 1993 ingress data. This peak occurred at a period of 1.23676s in file j9162a. The significance peaks at orbital phase 0.915, around half an hour before x-ray eclipse. After trials are included this peak is not statistically significant.

Figure 6.12 shows the distribution of Rayleigh powers for all the eclipse ingress files for both on-period and off-period regions. The on-period region includes the Rayleigh powers for $\pm 0.3\%$ around the first and second harmonics of the x-ray period. Rayleigh powers for the off-period region were derived from periods between the first and second harmonics (0.62s - 1.23s). Rayleigh power distributions are shown for both the uncut data (only a pulse maximum cut applied) and the data after pulse parameter cuts. A Fisher test was used to compare the on-period and off-period distributions for both cut and uncut data. For the uncut data the chance probability that the on-period distribution arises from a fluctuation in the background is 0.75. The chance probability for the cut data is 4.86×10^{-2}.

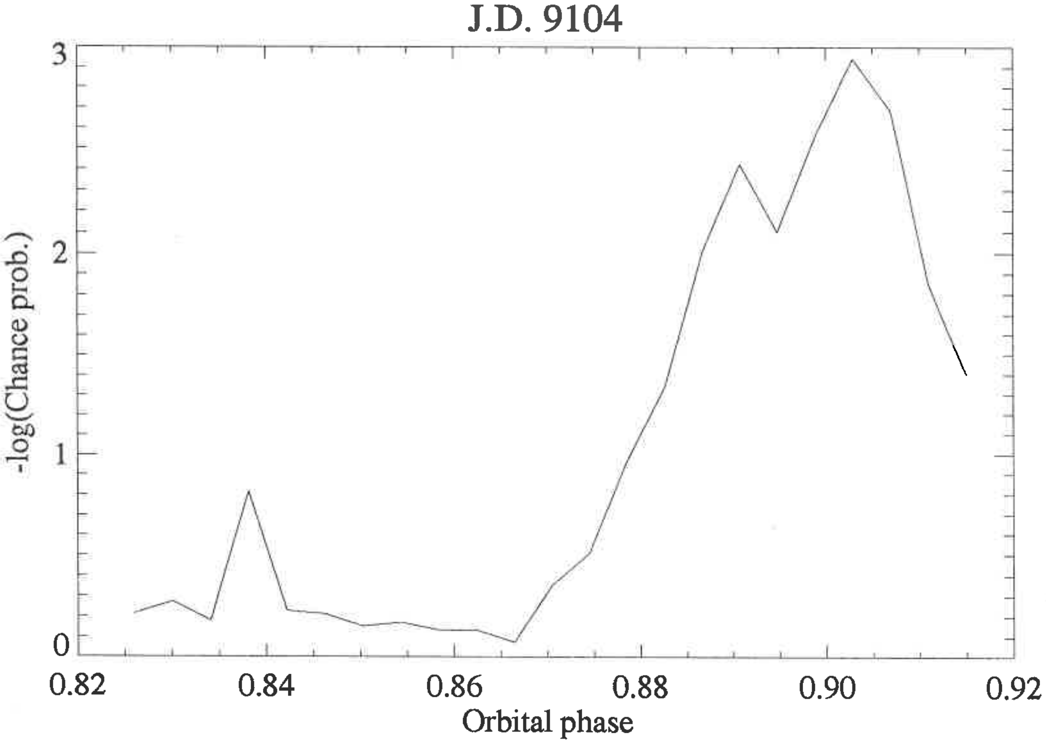

Figure 6.10: One hour wide sliding bin through ingress file j9104a.

6.2.2.2 Eclipse Egress

The four eclipse egress files were treated in the same way as the ingress data. Where possible, egress files were truncated to encompass orbital phases an hour each side of x-ray eclipse egress. Period scans using the Z_1^2 test around the first and second harmonics of the x-ray period show no statistically unlikely episodes. Figure 6.13 shows the incoherently combined chance probability versus period for the first and second harmonics.

Figure 6.14 shows the Rayleigh power distributions at egress for both the cut and uncut data. The chance probabilities that on-period and off-period regions were drawn from the same distribution for uncut and cut data are 3.25×10^{-2} and 8.03×10^{-2} respectively.

6.2.2.3 Other Orbital Phases

The two data files not taken at ingress or egress were split into four files, each of approximately two hours length. Rayleigh tests around the first and second

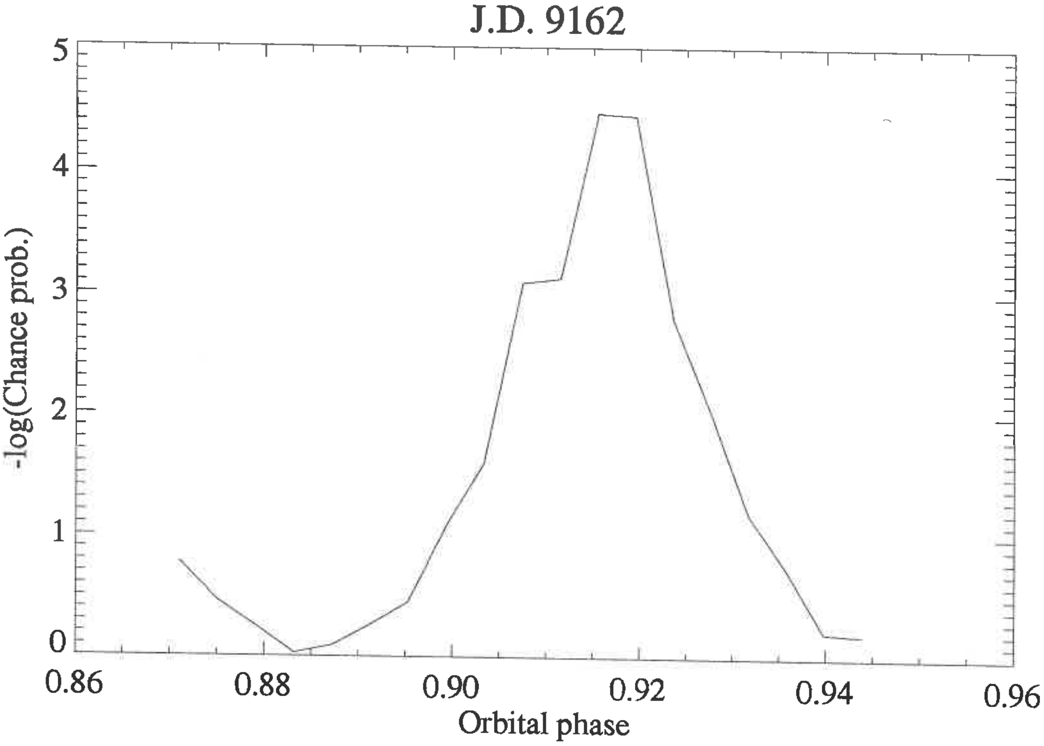

Figure 6.11: One hour wide sliding bin through ingress file j9162a.

harmonics of the X-ray period show no apparently significant peaks. Figure 6.15 shows the chance probability for these files incoherently added for both first and second harmonics.

Figure 6.16 shows the distribution of Rayleigh powers for these data files. Fisher tests on these distributions show no statistically significant difference between the on-period and off-period regions.

6.2.3 Summary

Analysis of data from Hercules X-1 has shown the possibility of gamma-ray emission from this object. In this section I will try to assess the significance of this claim and discuss features of the observations that detract from or enhance the claim for gamma-ray emission.

The three ingress files taken during 1992 all showed evidence for emission at a period blue-shifted from the x-ray period by 0.05%. The statistical significance of these three signals was found to be 1.35×10^{-4}. Detections of this significance are common in VHE and UHE gamma-ray astronomy and do not provide overwhelming

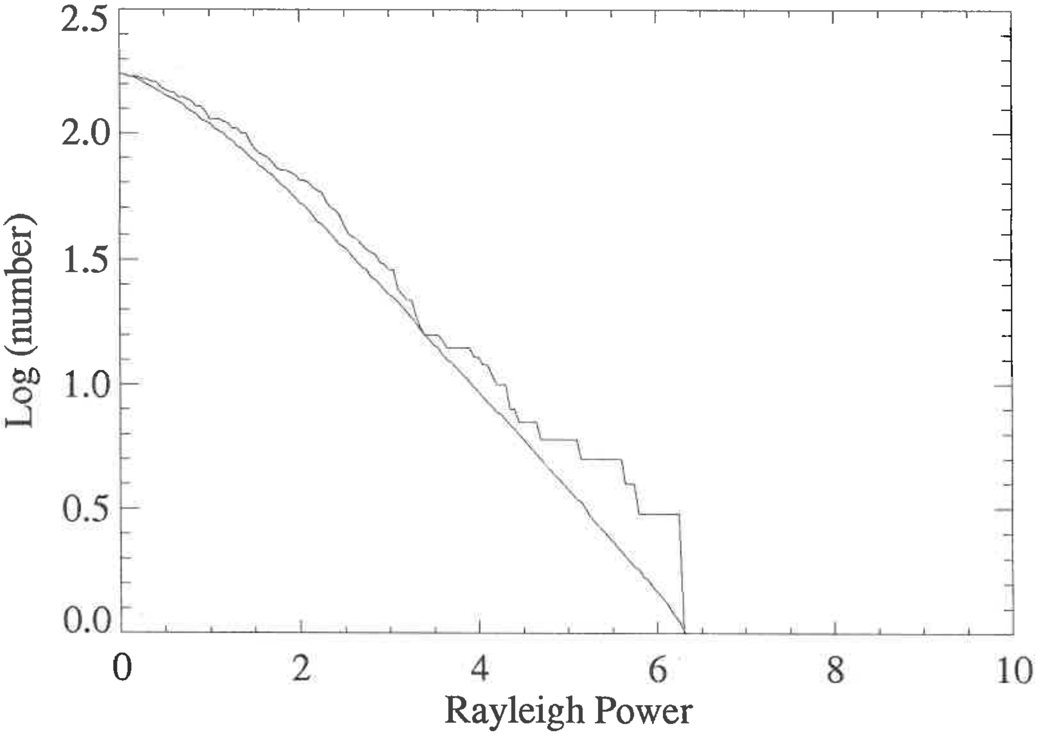

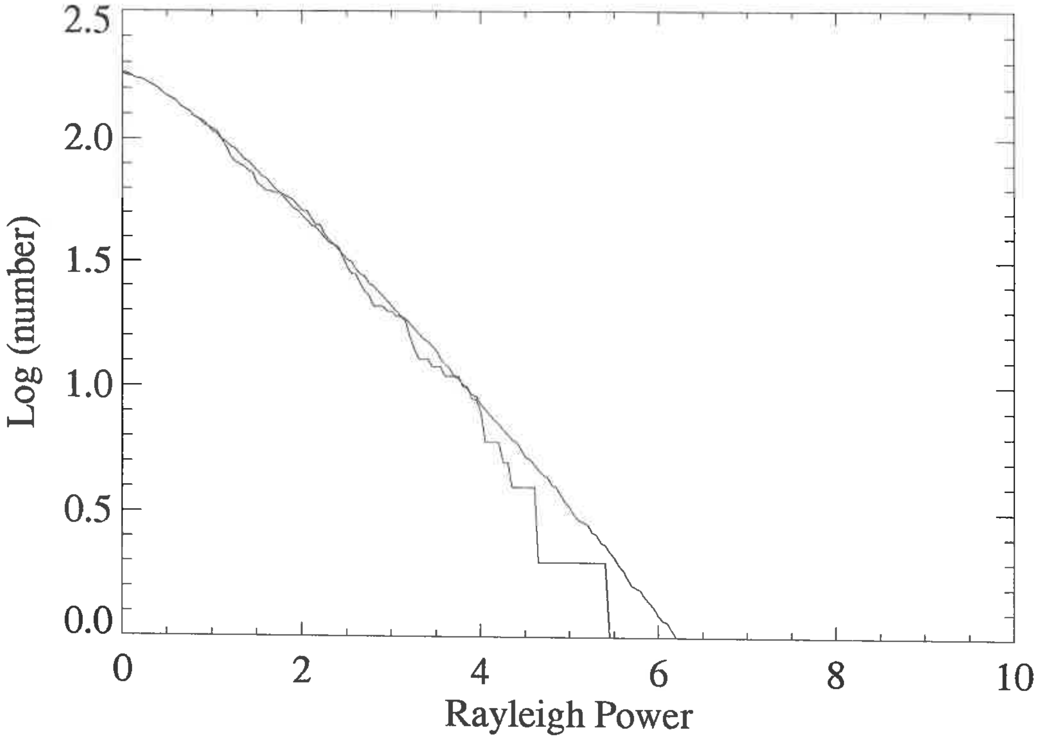

Figure 6.12: Distribution of Rayleigh powers for 1993 eclipse ingress files. The bottom graph shows the distribution before pulse profile cuts and the top shows the distribution after cuts. The straighter line indicates the background distribution of Rayleigh powers.

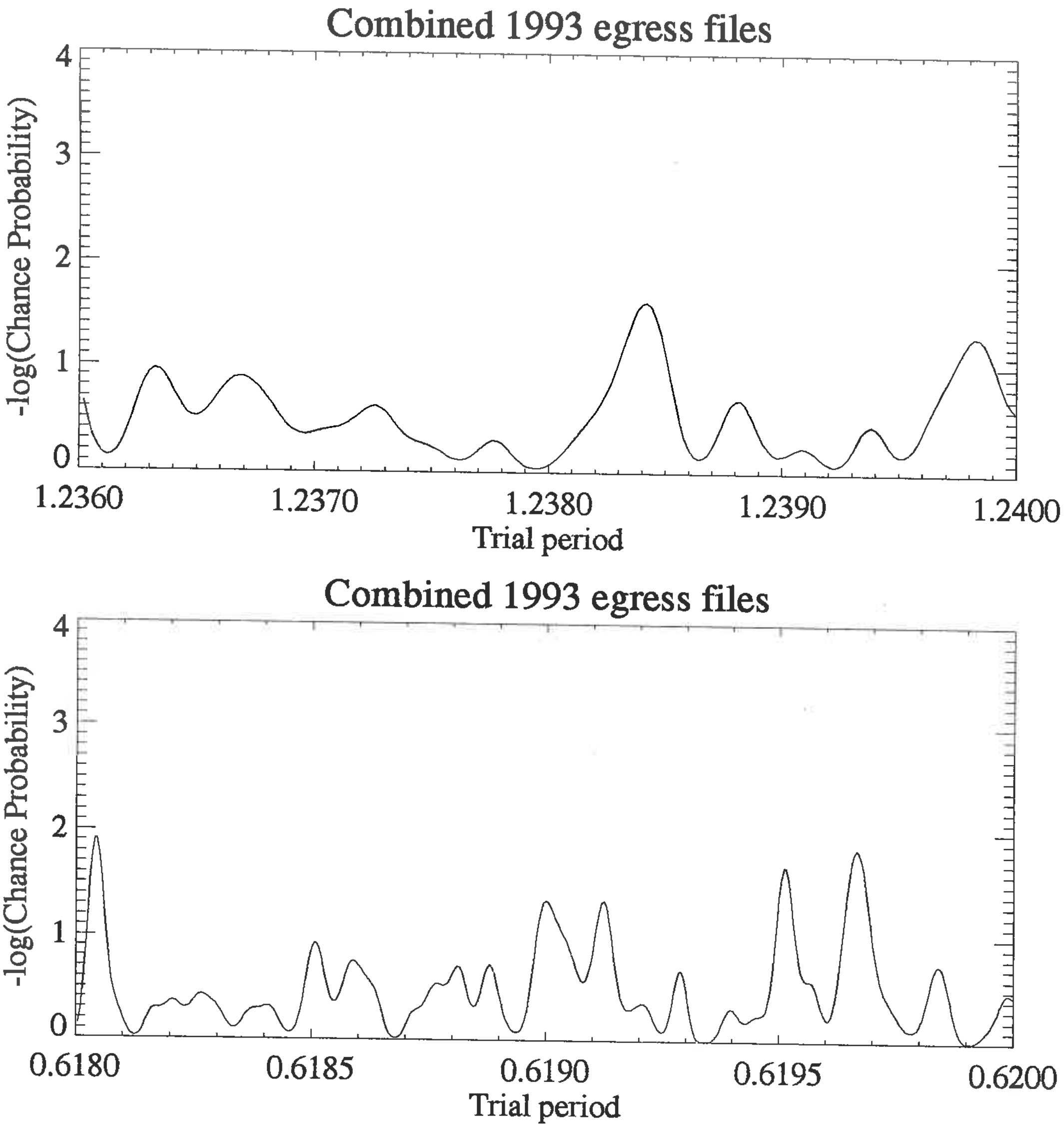

Figure 6.13: Nominal chance probability around the first and second harmonics of the x-ray period for 1993 eclipse egress files. The files have been added incoherently and analyzed as Z_4^2.

evidence for gamma-ray emission.

The luminosity of the observations were all found to be around 10^{36} erg/s. This is comparable to the luminosities of other claimed detections (Weekes 1988) and less than the bolometric luminosity of Her X-1 ($\sim 10^{37}$ erg/s). If the emission were assumed to be beamed rather than isotropic then the calculated luminosity would be reduced.

The use of the pulse profile measurement system lends some weight to the claim that the signals are due to gamma-rays. It was found that the signals were enhanced

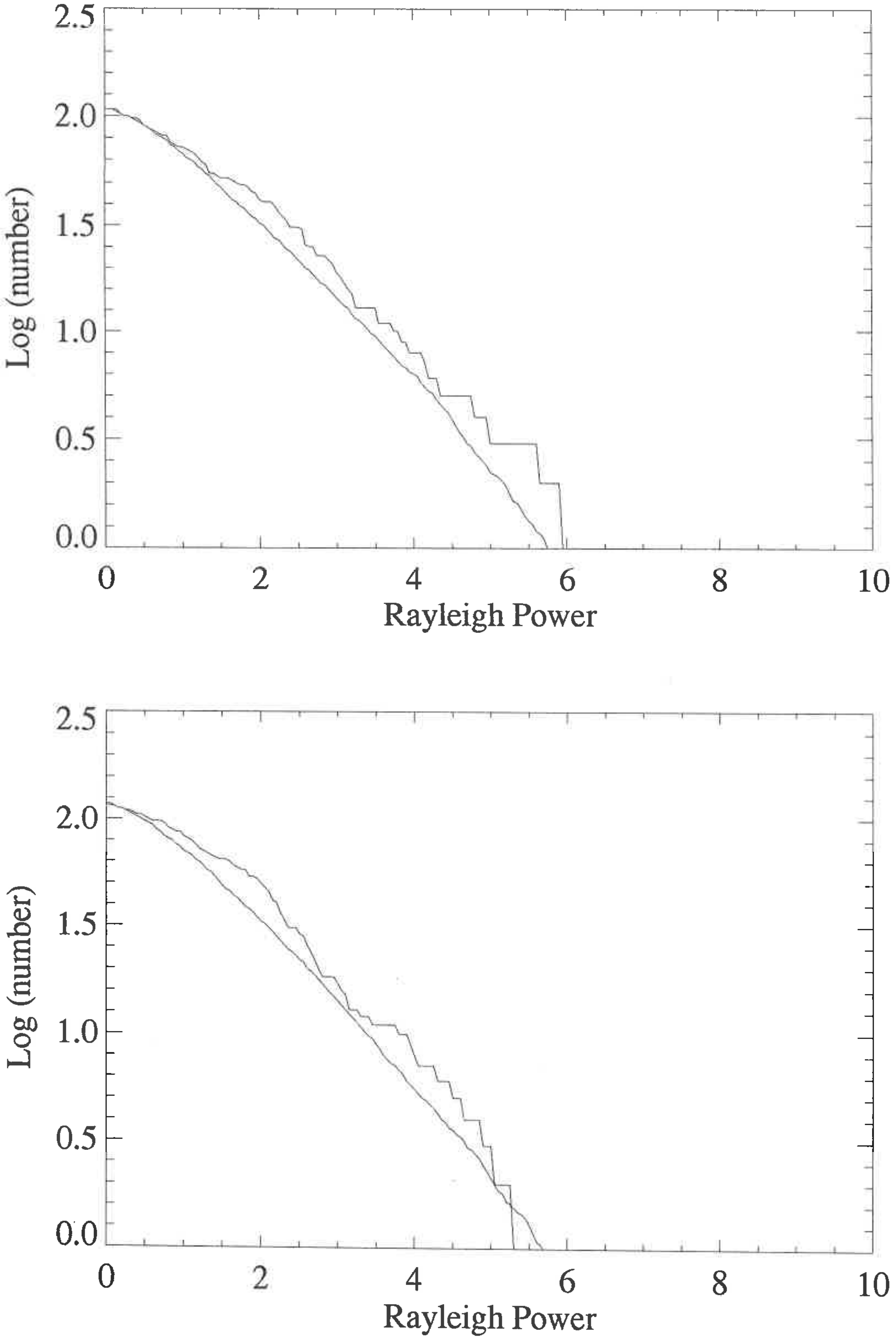

Figure 6.14: Distribution of Rayleigh powers for 1993 eclipse egress files. The bottom graph shows the distribution before pulse profile cuts and the top shows the distribution after cuts.

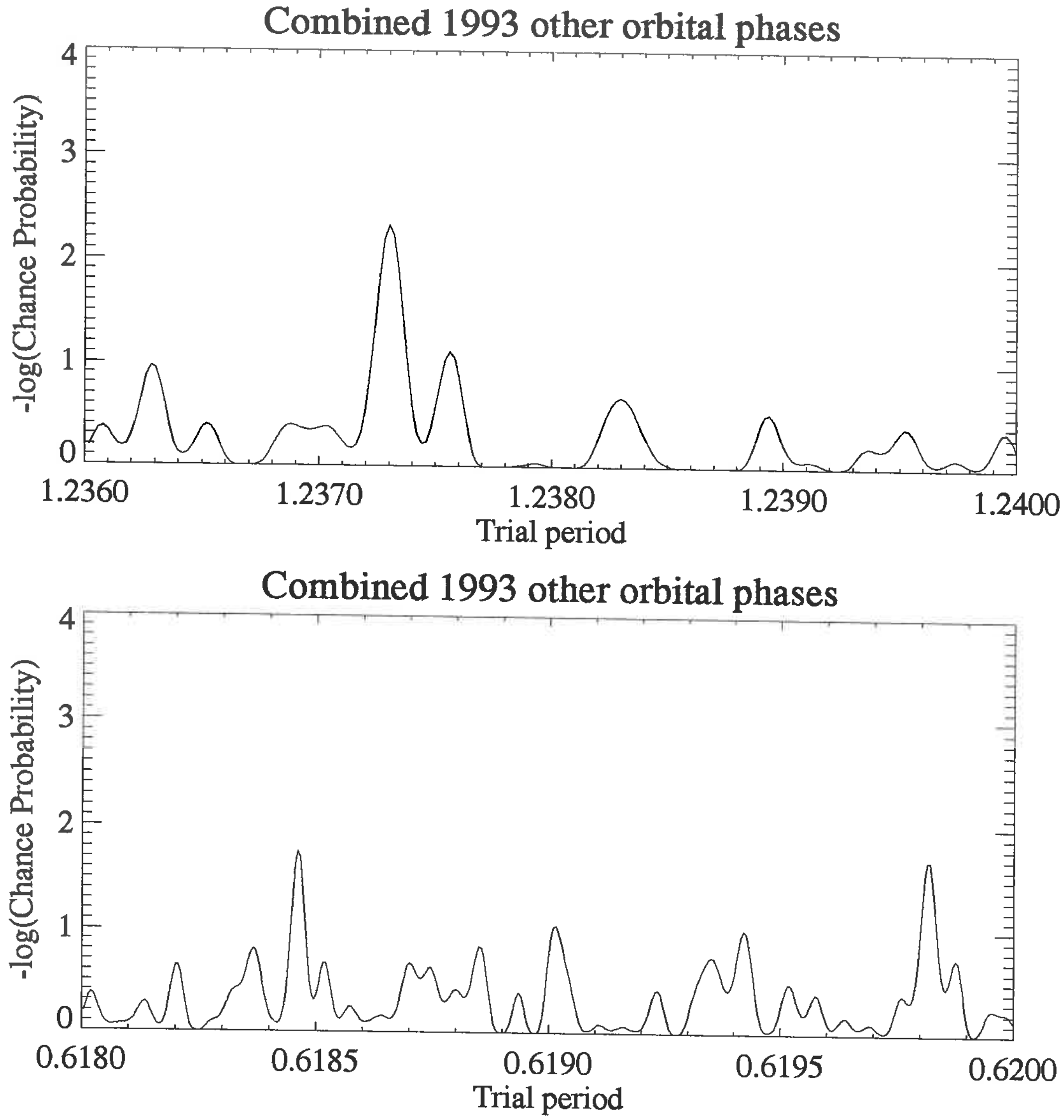

Figure 6.15: Nominal chance probability versus period for files not at egress or ingress. The probabilities from both first and second harmonics have been added incoherently.

when only those events that were selected to be "gamma-ray" like were analyzed. The amount of signal enhancement was consistent with Monte Carlo predictions.

One of the difficulties in assessing these results is the peculiarities in the apparent nature of the emission. The three ingress files all show signals blue-shifted from the pulsar period of Her X-1. The only file with complete orbital phase coverage around eclipse showed that the signal strength peaked ~ 10 minutes after the onset of eclipse (see figure 6.5). The amount of blue-shifting is consistent with other reported detections, which include observations by the Whipple group during

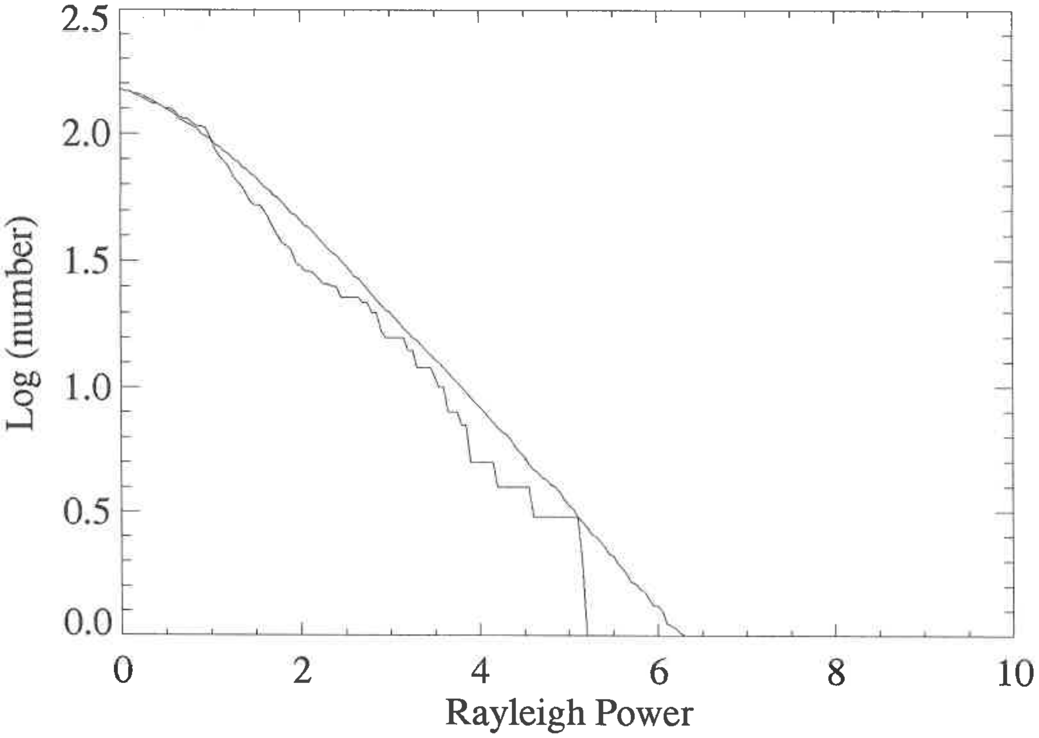

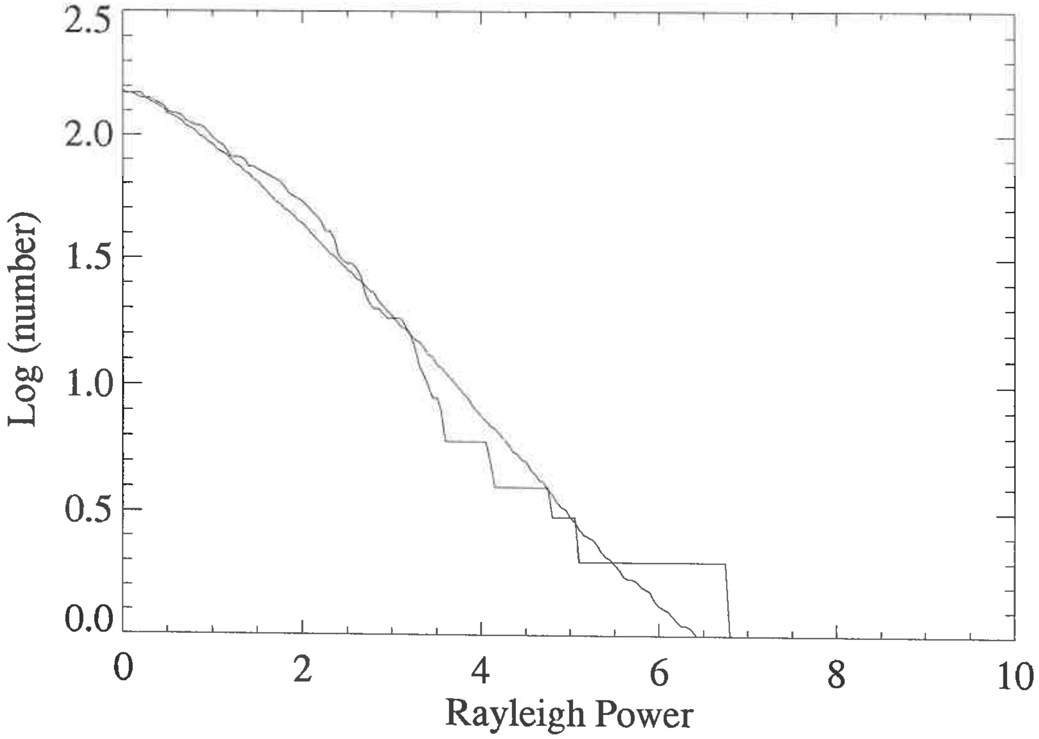

Figure 6.16: Distribution of Rayleigh powers for 1993 files not taken at eclipse ingress or egress. The bottom graph shows the distribution before pulse profile cuts and the top shows the distribution after cuts.

the eclipse of Her X-1 (see section 1.5.2).

Gorham and Learned (GL) have proposed a beam steering model where protons generated at the neutron star produce observable gamma-rays during eclipse by being bent onto the limb of the companion star (see section 1.5.4). I have written a program to simulate this model using the parameters suggested by GL (including a 0.1G surface field for HZ-Her). This model shows that 200TeV protons would produce observable ~20TeV gamma-rays some 20 minutes after the onset of eclipse. Protons of higher energy would produce observable gamma-rays sooner after the onset of eclipse. This is compatible with the orbital phase of peak signal strength in the Woomera observations but does not explain the apparent signal prior to eclipse ingress. The fact that observations of eclipse egress, taken during the same period as the ingress observations, show no signal is consistent with the model of GL because ingress and egress do not provide equivalent conditions for beam steering. The model of GL does not provide a mechanism for the blue-shifting of the gamma-ray signal.

In section 1.5.3 three models were discussed that attempted to explain the blue-shifting of the gamma-ray signal from Her X-1. The models of Aharonian and Atoyan (AA) and Slane and Fry (SF) do not seem to be consistent with the Woomera observations. These observations showed blue-shifting at the same period in data taken over 34 days. The AA and SF models would not seem to be able to produce blue-shifted emission at the same period for this length of time. The model of Cheng and Ruderman (CR) proposes that a low density bubble traveling down the accretion disk provides a target for gamma-ray production. Presumably, if the accretion rate were constant, it would be possible to maintain a particular blue-shifted period for some time. If the CR model is correct then the amount of blue-shifting would be dependent upon the rate of inflow of accreting material. It may be possible, therefore, to correlate measurements related to the inflow rate (such as x-ray luminosity) with the values of reported VHE blue-shifts. The model of CR could provide visible gamma-rays for a period after the onset of eclipse, but only if the orientation of the accretion disk were favorable.

Another problem with claiming gamma-ray emission from Her X-1 is that it was not seen by northern hemisphere observatories around the time that these observations were made. This may be because the energy threshold of BIGRAT when viewing Her X-1 is between the energies where northern hemisphere arrays and air Čerenkov experiments are sensitive.

No significant emission was seen from Her X- 1 by the Woomera group during 1993. It is hoped that further observations, and perhaps new observing techniques, will shed light on the signals reported in this chapter.

Chapter 7

Conclusions and Suggestions for Further Work

This thesis has described a technique for enhancing the gamma-ray sensitivity of an atmospheric Čerenkov telescope. The technique relies on the identification of gamma-ray initiated EAS on the basis of the temporal distribution of Čerenkov photons. Monte Carlo simulations performed by the author have shown that the measurement of simple pulse parameters can be used to reject a large number of background cosmic ray events. It has been shown that the pulse profile measurement technique can provide sensitivity enhancement for observations made at all zenith angles. Simulations show that by using a mixture of pulse rise-time and full width half maximum measurements, around 95% of the cosmic ray background can be rejected while retaining almost half of the gamma-rays. The quality factor attainable by the pulse measurement technique (~ 2) is comparable to that expected for a camera system installed on the Woomera telescope.

A pulse profile measurement system has been described in this thesis. This system has been installed on the Woomera air Čerenkov telescope and has been used for observations of the x-ray binary system Hercules X-1 during 1992 and 1993. Her X-1 culminates at $\sim 65°$ from zenith when viewed from Woomera, which corresponds to a gamma-ray energy threshold of $\sim$ 20TeV.

Analysis of the Her X-1 data has shown the possible detection of gamma-rays for data taken during 1992. The signal was found in events selected by the pulse measurement system to be gamma-ray like. The signal was pulsed at a period blue-shifted from the x-ray period of Her X-1 by 0.05% and appeared in all three observations taken around eclipse ingress. The one file containing continuous observation either side of eclipse ingress showed the strongest signal shortly after the onset of eclipse. Both blue-shifting of gamma-ray signals and emission after the onset of eclipse have been reported from previous observations of Her X-1. Flux levels calculated from the three ingress files all show a flux above 27TeV of around 4×10^{-12} gamma-rays s^{-1} cm^{-2}. If isotropic gamma-ray emission is assumed, this corresponds to a gamma-ray luminosity of $\sim 10^{36}$ erg/s. The combined statistical significance for the ingress files was calculated to be 1.34×10^{-4}. Period analysis of data taken at other orbital phases during 1992 showed no statistically significant evidence for emission at or near the x-ray period of Her X-1.

During 1993 Her X-1 was observed extensively, including 5 observations encompassing eclipse ingress. Period analysis of the 1993 data set showed no evidence for gamma-ray emission at or near the x-ray period of Her X-1.

7.1 Further Work

The pulse profile measurement technique described in this thesis leaves much room for further work. In particular, the combination of camera image cuts and pulse profile cuts could be used to improve the sensitivity of gamma-ray observations. Monte Carlo simulations would be needed to determine which cuts should be used, and how they should be applied over a range of zenith angles.

Section 5.7 discussed the effect of the cosmic ray composition on the pulse parameter distributions. It is possible that careful observations, combined with Monte Carlo simulations, could provide an estimate of cosmic ray compositions for energies from $\sim$ 1TeV to over a PeV.

References

Aharonian, F. A. & Atoyan, A. M. (1991), *Ap. J.* **381**, 220.

Aharonian, F. A., Kanevsky, B. L. & Sahakian, V. A. (1991), *J. Phys. G:Nucl. Phys* **17**, 1909.

Akerlof, C. W., Cawley, M. F., Fegan, D. J., Hillas, A. M. et al. (1990), *Nucl, Phys. B (Proc. Suppl.)* **14A**, 237.

Alexandreas, D. E., Allen, G., Berley, D. et al. (1993), *Ap. J.* **405**, 353.

Alexeenko, V. V. et al. (1990), *Proc. Int. Workshop on VHE Gamma-ray Astr. (Crimea)* p. 187.

Allan, H. R. (1971), *Prog. Elem. Part. and Cosmic Ray Physics* **10**, 170.

Austin, R., Camerini, U., Finley, J. et al. (1990), *Proc. 21st ICRC (Adelaide)* **2**, 110.

Baillon, P., Behr, L., Danagoulian, S., Dudelzak, B. et al. (1991), *Proc. 22nd ICRC (Dublin)* **1**, 220.

Baltrusaitis, R. M., Cassidy, G. L., Cooper, R. et al. (1985), *Ap. J. Lett.* **293**, L69.

Battistoni, G. et al. (1985), *Phys. Lett* **155B**, 465.

Bevington, P. R. (1969), *Data Reduction in the Physical Sciences (New York:McGraw-Hill).*

Bignami, G. F., Maraschi, L. & Treves, A. (1977), *Astron. Astrophys.* **55**, 155.

Bird, D. J. & Clay, R. W. (1990), *Proc. 21st I.C.R.C. (Adelaide)* **3**, 139.

Blackett, P. M. S. (1948), *in Rep. Conf. Gassiot Comm. of the Physical Society, London on "Emission Spectra of the Night Sky and Aurora"* p. 34.

Bloomer, S. D., Idenden, D. W., Lambert, A. et al. (1990), *Proc. 21st ICRC (Adelaide)* **2**, 334.

Borione, A., Catanese, M., Covault, C. E. et al. (1993), *Proc. 23rd ICRC (Calgary)* **1**, 385.

Bosia, G., Castagnoli, C., Marangoni, G. et al. (1972), *Il Nuovo Cimento* **9**(2), 177.

Brazier, K. T. S., Carraminana, A., Chadwick, P. M., Dipper, N. et al. (1990), 21^{st} *ICRC (Adelaide)* **4**, 270.

Brink, C., Cheng, K. S., de Jager, O. C. et al. (1990), *Proc.* 21^{st} *ICRC (Adelaide)* **2**, 283.

Cawley, M. F. (1988), *Nucl. Inst. and Meth.* **A264**, 64.

Cawley, M. F., Fegan, D. J., Harris, K., Hillas, A. M. et al. (1990), 21^{st} *ICRC (Adelaide)* **4**, 224.

Chadwick, P. M., Dipper, N. A., Dowthwaite, J. C. et al. (1985), *Nature* **318**, 642.

Chadwick, P. M., Dipper, N. A., Kirkman, I. W. et al. (1987), *Proc. NATO Workshop on VHE Gamma-ray Astr. (Durham)* p. 121.

Chanmugam, G. & Brecher, K. (1985), *Nature* **313**, 767.

Châtelet, E., Procureur, J., Stamenov, J. N. & Ushev, S. Z. (1990), *J. Phys. G:Nucl. Phys.* **16**, 317.

Cheng, K. S. & Ruderman, M. (1989), *Ap. J.* **337**, L77.

Cheng, K. S., Ho, C. & Ruderman, M. (1986a), *Ap. J.* **300**, 500.

Cheng, K. S., Ho, C. & Ruderman, M. (1986b), *Ap. J.* **300**, 522.

Cheung, T. & MacKeown, P. K. (1988), *Il Nuovo Cimento* **11C**, 193.

Clay, R. W., Corani, C. L., Patterson, J. R., Dawson, B. R., Edwards, P. G., Gregory, A. G., Prescott, J. R., Elton, S. D. & Ciampa, D. (1985), *Proc.* 19^{th} *ICRC (La Jolla)* **3**, 414.

Clay, R. W., Gerhardy, P. R. & Liebing, D. F. (1984), *Aust. J. Phys.* **37**, 91.

Clay, R. W., Giles, D. H., Gregory, A. G., Patterson, J. R., Prescott, J. R. et al. (1989), *Proc. Astr. Soc. Aust.* **8**, 41.

Clay, R. W., Meyhandan, R., Horton, L., Ulrichs, J. & Winn, M. M. (1992), *Astron. Astrophys.* **255**, 167.

Cocconi, G. (1959), *in:Proc. Moscow Conf. on Cosmic Rays* **2**, 309.

Cronin, J. W., Fick, B. E., Gibbs, K. G. et al. (1992), *Phys. Rev. D.* **45**(12), 4385.

Curtis-Michel, F. (1982), *Rev. Mod. Phys.* **54**, 1.

Dawson, B. R. (1985), PhD thesis, University of Adelaide.

Dawson, B. R., Clay, R. W., Patterson, J. R. & Prescott, J. R. (1989), *J. Phys. G:Nucl. Part. Phys.* **15**, 893.

de Beer, J. F., Holyoak, B., Wdowczyk, J. & Wolfendale, A. W. (1966), *Proc. Phys. Soc. Lond.* **89**, 567.

de Jager, O. C. (1987), *Ph.D. Thesis, University of Potchefstroom for Christian Higher Education.*

Deeter, J. E., Boynton, P. E. & Pravdo, S. H. (1981), *Ap. J.* **247**, 1003.

Dermer, C. D. & Schlickeiser, R. (1992), *Science* **257**, 1642.

Dermer, C. D. & Schlickeiser, R. (1993), *Proc. 23rd ICRC (Calg.)* **1**, 160.

Dermer, C. D., Schlickeiser, R. & Mastichiadis, A. (1992), *Astron. Astrophys.* **256**, L27.

Dingus, B. L., Alexandreas, D. E., Allen, R. C., Burman, R. L., Butterfield, K. B., et al. (1988), *Phys. Rev. Lett.* **61**(17), 1906.

Dowthwaite, J. C., Harrison, A. B., Kirkman, I. W. et al. (1984), *Nature* **309**, L691.

Duke, D. W. & Owens, J. (1982), *Phys. Rev. D* **26**, 1600.

Dumora, D., Procureur, J. & Stamenov, J. N. (1992), *J. Phys. G: Nucl. Part. Phys.* **18**, 1839.

Dzikowski, T., Gawin, J., Grochalska, B., Wasilewski, A. & Wdowczyk, J. (1981), *Proc. 17th ICRC* **1**, 8.

Eadie, W. T., Drijard, D., James, F. E. et al. (1971), *Statistical Methods in Experimental Physics (North-Holland ,Amsterdam).*

Edwards, P. G., Fujii, H., Fujimoto, M., Hara, T. et al. (1993), *Proc. 23rd ICRC (Calgary)* **2**, 426.

Edwards, P. G., Protheroe, R. J. & Rawinski, E. (1985), *J. Phys. G:Nucl. Phys.* **11**, L101.

Eichler, D. & Vestrand, W. T. (1985), *Nature* **318**, L345.

Fegan, D. J. (1992), *Proc. of the first Palaiseau Workshop (Palaiseau)* p. 3.

Fenyves, E. J. (1985), *Techniques in Ultra High Energy Gamma Ray Astronomy,* (University of Adelaide), p. 124.

Fenyves, E. J., Balog, S. N., Davis, N. R., Suson, D. J. & Stanev, T. (1988), *Phys. Rev. D* **37**, 649.

Fichtel, C. E. (1994), *Ap. J. Suppl. (in press).*

Fichtel, C. E., Hartman, R. C., Kniffen, D. A. et al. (1975), *Ap. J.* **198**, 163.

Fisher, R. A. (1958), *Statistical Methods for Research Workers (Oliver and Boyd, Edinburgh and London).*

Forman, W. et al. (1978), *Ap. J. Suppl.* **38**, 357.

Frank, I. M. & Tamm, I. E. (1937), *Dokl. Akad. Nauk. SSSR* **14**, 109.

Gaisser, T. K. (1990), *Cosmic Rays and Particle Physics*, Cambridge University Press.

Gaisser, T. K., Harding, A. K. & Stanev, T. (1987), *Nature* **329**, 314.

Galbraith, W. & Jelley, J. V. (1953), *Nature* **171**, 349.

Gibson, A. I. et al. (1982), *in:Proc. Int. Workshop on Very High Energy Gamma-ray Astronomy P. V. Ramana Murthy and T. C. Weekes eds (Bombay, Tata Inst.)* p. 97.

Goldreich, P. & Julian, W. H. (1969), *Ap. J.* **157**, 869.

Gorham, P. W. & Learned, J. G. (1986), *Nature* **323**, 422.

Gorham, P. W., Cawley, M. F., Fegan, D. J. et al. (1986a), *Ap. J.* **309**, 114.

Gorham, P. W., Cawley, M. F., Fegan, D. J. et al. (1986b), *Ap. J.* **308**, L11.

Gould, R. J. & Schreder, G. (1966), *Phys. Rev. Lett.* **16**, 252.

Greenwood, J. A. & Durrand, D. (1955), *Annals of Mathematical Statistics* **26**, 233.

Gregory, A. G., Patterson, J. R., Roberts, M. D., Smith, N. I. & Thornton, G. J. (1990), *Proc. 21st ICRC (Adelaide)* **2**, 279.

Greisen, K. (1956), *Prog. Cosmic Ray Phys.* **3**, 1.

Greisen, K. (1960), *Ann. Rev. Nucl. Sci* **10**, 63–108.

Grindlay, J. E. (1971), *Ph.D Thesis Harvard University and SAO special report 334.*

Gupta, S. K., Rajeev, M. R., Sreekantan, B. V., Srivatsan, R. & Tonwar, S. C. (1990), *Proc. 21st ICRC (Adelaide)* **2**, 162.

Gupta, S. K., Ramana-Murthy, P. V., Tonwar, S. C. & Vishwanath, P. (1982), *in:Proc. Int. Workshop on Very High Energy Gamma-ray Astronomy P. V. Ramana Murthy and T. C. Weekes eds (Bombay, Tata Inst.)* p. 295.

Hanbury-Brown, R., Davis, J. & Allen, L. R. (1969), *Mon. Not. Roy. Astr. Soc* **16**, 411.

Hara, T. et al. (1993), *Nucl. Inst. Meth. Phys. Res. A (submitted).*

Harding, A. K. & Gaisser, T. K. (1989), *Ap. J. Preprint.*

Hess, V. F. (1912), *Physik Zeitshr.* **13**, 1804.

Hewish, A., Bell, S. J., Pilkington, J. D. H. et al. (1968), *Nature* **217**, 709.

Hill, D. A. & Porter, N. A. (1961), *Nature* **191**, 690.

Hillas, A. M. (1982), *J. Phys. G:Nucl. Phys.* **8**, 1475.

Hillas, A. M. (1985), *Proc. 19th ICRC (La Jolla)* **3**, 445.

Hillas, A. M. (1987), *Proc. 20th ICRC (Moscow)* **2**, 262.

Hillas, A. M. & Patterson, J. R. (1987), *Very High Energy Gamma-Ray Astronomy*, K. E. Turver ed. Dordrecht:D.Reidel, p. 243.

Hillas, A. M. & Patterson, J. R. (1990), *J. Phys. G* **16**, 1271.

Hoffmeister, C. (1941), *Kl. Verein. Beob. Bull.*

Hunter, S. D. (1993a), *GRO workshop, 23rd ICRC (Calgary) (in press).*

Hunter, S. D. (1993b), *Priv. Comm.*

Jackson, J. D. (1962), *Classical Electrodynamics*, John Wiley and Sons (New York).

Jelley, J. V. (1966), *Phys. Rev. Lett.* **16**, 479.

Jelley, J. V. (1967), *Prog. Elem. and Cosmic Ray Physics* **9**, 41.

Jelley, J. V. (1982), *in Proc. Int. Workshop on Very High Energy Gamma-Ray Astronomy P.V. Ramana Murthy, T.C.Weekes eds. (Bombay:Tata Inst.) p3.*

Jones, C. A., Forman, W. & Liller, W. (1973), *Ap. J.* **182**, L109.

Kanbach, G., Bertsch, D. L., Favale, A. et al. (1988), *Space Sci. Rev.* **49**, 69.

Kazanas, D. & Ellison, D. C. (1986), *Nature* **319**, 380.

Khristiansen, G. B., Kalmykov, N. N., Kulikov, G. V., Silaev, A. A., Solovieva, V. I. et al. (1990), *Proc. 21st ICRC (Adelaide)* **2**, 362.

Kifune, T., Nishimura, K., Hara, T., Hatano, Y., Hayashida, N. et al. (1986), *Astrophys. J* **301**, 230.

Kifune, T., Tsukagoshi, T., Fujii, H., Fujimoto, M. et al. (1993), *Proc. 23rd ICRC (Calgary)* **2**, 592.

Kiraly, P. & Meszaros, P. (1988), *Ap. J.* **333**, 719.

Kniffen, D. A., Fichtel, C. E., Hartman, R. C. et al. (1977), *Proc. 12th ESLAB Symp. Recent Adv. in Gamma-ray Astron.* p. 45.

Kovacs, F. (1990), *Nucl. Phys. B (proc. Suppl.)* **14A**, 330.

Krys, A., Krys, E. & Wasilewski, A. (1991), *J. Phys. G: Nucl. Phys.* **17**, 1261.

Lamb, R. C., Cawley, M. F., Gibbs, D. J. et al. (1988), *Ap. J.* **328**, L13.

Lewis, D. A. (1990), *Nucl. Phys. B. (Proc. Suppl.)* **14A**, 299.

Lloyd-Evans, J., Coy, R. N., Lambert, A., Lapikens, J., Patel, M. et al. (1983), *Nature* **305**, 784.

Lovelace, R. V. E. (1976), *Nature* **262**, 649.

Marshak, M. L. et al. (1985a), *Phys. Rev. Lett.* **54**, 2079.

Marshak, M. L. et al. (1985b), *Phys. Rev. Lett.* **55**, 1965.

Meyhandan, R., Dawson, B. R., Clay, R. W., Horton, L., Ulrichs, J. & Winn, M. M. (1992), *Ap. J* **391**, 236.

Mihara, T., Ohashi, T., Makishima, K. et al. (1991), *Publ. Astron. Soc. Japan* **43**, 501.

Nagle, D. E., Gaisser, T. K. & Protheroe, R. J. (1988), *Ann. Rev. Nucl. Part. Sci.* **38**, 609.

Nishimura, J. & Kamata, K. (1951), *Prog. Theor. Phys.* **6**, 628.

Ögelman, H. (1987), *Astron. Astrophys.* **172**, 79.

Ogio, S., Kifune, T., Tanimori, T. et al. (1993), *Proc.* 23rd *ICRC (Calgary)* **1**, 392.

Orford, K. J. & Turver, K. E. (1981), 17th *ICRC (Paris)* **6**, 130.

Paccini, F. (1968), *Nature* **219**, 145.

Patterson, J. R. & Hillas, A. M. (1989), *Nucl. Inst. and Meth.* **A278**, 553.

Petterson, J. A., Rothschild, R. E. & Gruber, D. E. (1991), *Ap. J.* **378**, 696.

Porter, N. A. & Long, C. D. (1963), *in British Conf. on Nuclear interactions at Ultra-high Energies.*

Protheroe, R. J. (1985), *Astron. Express* **1**, 137.

Protheroe, R. J. (1986), *Mon. Not. R. Astr. Soc.* **221**, 769.

Protheroe, R. J. (1993), *Ap. J Suppl. (in press).*

Protheroe, R. J. & Clay, R. W. (1985), *Nature* **315**, 205.

Protheroe, R. J., Clay, R. W. & Gerhardy, P. R. (1984), *Astrophys. J. Lett.* **280**, L47.

Punch, M., Akerlof, C. W., Cawley, M. F., Chantell, M. et al. (1992), *Nature* **358**, 477.

Punch, M., Akerlof, C. W., Cawley, M. F., Fegan, D. J. et al. (1991), *Proc.* 22nd *ICRC (Dublin)* **1**, 464.

Quenby, J. J. & Lieu, R. (1987), *Proc* 20th *ICRC (Moscow)* **1**, 252.

Rao, M. V. S. & Sinha, S. (1988), *J. Phys. G:Nucl. Phys.* **14**, 811.

Rawat, H. S., Rannot, R. C., Sapru, M. L. et al. (1990), *Proc. 21st ICRC (Adelaide)* **2**, 104.

Rayleigh, L. (1894), *Theory of Sound (London: McMillian and co.)* **1**, 35.

Rees, M. J. (1984), *Ann. Rev. Astron. Astrophys.* **22**, 471.

Resvanis, L., Learned, J., Stenger, V. et al. (1988), *Ap. J.* **328**, L9.

Reynolds, P. T., Akerlof, C. W., Cawley, M. F. et al. (1993), *Ap. J.* **404**, 206–218.

Reynolds, P. T., Cawley, M. F., Fegan, D. J. et al. (1991), *Ap. J.* **382**, 640.

Rossi, B. (1952), *High Energy Particles*, Prentice-Hall,Inc.

Rossi, B. (1964), *Cosmic Rays*, McGraw-Hill.

Rossi, B. & Greisen, K. (1941), *Rev. Mod. Phys.* **13**, 240.

Samorski, M. & Stamm, W. (1983), *Astrophys. J. Lett* **268**, L17.

Shapiro, S. L. & Teukolsky, S. A. (1983), *"Black Holes, White Dwarfs and Neutron Stars" (New York:John Wiley and sons).*

Sikora, M., Begelman, M. C. & Rees, M. (1993), *in Proc. of the Compton Symposium (eds N. Gehrels and M. Friedlander) in press.*

Slane, P. & Fry, W. F. (1989), *Ap. J.* **342**, 1129.

Sommers, P. & Elbert, J. W. (1987), *J. Phys. G:Nucl. Phys.* **13**, 553.

Standish, E. M. (1982), *Astron. Astrophys.* **114**, 297.

Suga, K., Toyoda, Y., Kamata, K., Murakami, K., LaPointe, M. et al. (1985), *Techniques in Ultra High Energy Gamma Ray Astronomy*, (University of Adelaide), p. 48.

Swannenberg, B. N., Bennett, K., Bignami, G. F. et al. (1981), *Ap. J.* **243**, L69.

Thompson, D. J., Bertsch, D. L., Hartman, R. C. & Hunter, S. D. (1983), *Astron. Astrophys* **127**, 220.

Thornton, G. J. & Clay, R. W. (1979), *Phys. Rev. Lett. (erratum Phy. Rev. Lett.,(1981),* **45**, *1463)* **43**, 1622.

Thornton, G. J. & Clay, R. W. (1981), *Phys. Rev. D* **23**, 2090.

Tonwar, S. C., Gopalakrishnan, N. V., Rajeev, M. R. & Sreekantan, B. V. (1988), *Astrophys. J. Lett.* **330**, L107.

Tornabene, H. S. & Cusimano, F. J. (1968), *Canad. Journ. Phys.* **46**, 581.

Trümper, J., Kahabka, P., Ögelman, H. et al. (1986), *Ap. J.* **300**, L63.

Tümer, O. T., O'Neil, T. J., Zych, A. D. & White, R. S. (1990), *Proc.* 21st *ICRC (Adelaide)* **4**, 238.

Turver, K. E. & Weekes, T. C. (1978), *Il Nuovo Cimento* **45B**(1), 99.

Vacanti, G., Cawley, M. F., Colombo, E., Fegan, D. J. et al. (1991), *Ap. J.* **377**, 467.

van der Walt, D. J., Raubenheimer, B. C., de Jager, O. C., North, A. R., van Urk, G. & deValliers, E. J. (1987), *Proc* 20th *ICRC (Moscow)* **1**, 303.

Weekes, T. C. (1976), *Il Nuovo Cimento* **35b**, 95.

Weekes, T. C. (1988), *Physics Reports* **160**, 1.

Weekes, T. C. (1991), *Priv. Comm.*

Weekes, T. C. (1992), *Space Science Reviews* **59**, 315–364.

Weekes, T. C., Cawley, M. F., Fegan, D. et al. (1989), *Ap. J* **342**, 379–395.

Weeks, D. D. (1989), *Proc. Fourth Workshop on Elementary-particle picture of the Universe (eds Hikasa et al.)* p. 255.

Westfall, G. D., Wilson, L. W., Lindstrom, P. J., Crawford, H. J., Greiner, D. E. & Heckman, H. H. (1979), *Phys. Rev. C* **19**(4), 1309.

Zatsepin, V. I. (1965), *Soviet Physics JETP* **20**, 459.

Zyskin, Y., Vladimirskii, B. M., Neshpor, Y. I. et al. (1987), *Astron. Circ. Bur. Astron. Inf. USSR Acad. of Sci* **1508**, 1.

ERRATA

Corrections are identified by chapter , page number and line number (L and B indicate the number of lines from the top and bottom of the page respectively)

Typographical and grammatical corrections

Summary Page v B4 - remove “in these files”
  Page v B2 - replace “significance” with “probability of chance occurence”
Chapter 1 Page 1 B6 - replace “discreet” with “discrete”
  Page 3 L10 - replace “remainder of this chapter will discuss” with “in the remainder of the chapter I will discuss”
  Page 3 L14 - replace “this section will contain” with “this section contains”
  Page 10 B2 - replace “and will detect gamma-rays” with “and can detect gamma-rays”
  Page 14 B8 - replace “gauss” with its symbol “G”
  Page 29 L10 - replace “Babha” with “Bhabha”
  Page 30 L4 - replace “The amount of blue-shifting is significantly different from” with “The periods reported are blue-shifted significantly from”
Chapter 2 Page 42 B9 - delete one of the “as the”
Chapter 3 Page 53 B3 - replace “whose particle flux is attenuated” with “where the particle flux is attenuated”.
  Page 65 L17 - replace “single three inch photomultipliers” with “single three-inch photomultipliers”
  Page 65 B6 - replace “accuracy of less than a milli-second” with “accuracy better than one milli-second”
  Page 65 L19 - replace “inner 30 camera pixels” with “30 of the camera pixels”
Chapter 4 Page 78 B13 - replace “angular size of gamma-ray image” with “angular size of the gamma-ray image”
  Page 87 L6 - replace “To further enhance” with “To enhance further”
Chapter 5 Pages 97, 98 - replace y-axis Emission Depth units “gcm” with “gcm^{-2}”

General Corrections, clarification and discussion

Chapter 1 Page 25 - The binary system Her X-1 is described as a low mass system. In fact it is an intermediate case and could be described as either a high or a low mass X-ray binary.

Chapter 3 Page 66 Fig. 3.11 - The figure caption for the lower part of fig 3.11 refers to a single on-axis tube for the outer mirrors. The other two tubes shown are part of an off-axis monitor system.

Page 68 Fig. 3.13 - This diagram was produced with a gamma-ray energy spectrum described by a power law with index of -1.65.

Chapter 5 Page 92 L6 - The "stray bits" are elements of the diode array in the 7912 digitizer that register accidentally during the recording of a pulse. They are easily identified and removed for pulse analysis.

Chapter 5 Table 5.1 - The quality factor, q, does not include the effects of the pulse height cut on the data (the pulse height cut rejects approximately 50% of the data). The exact effect of the pulse height cut on the quality factor will depend upon the source spectrum of the gamma-ray signal. When observing at large zenith angles it is usual to observe hard spectrum gamma-ray sources. This implies that a pulse height cut will not drastically reduce the quality factors quoted in table 5.1 .

Chapter 6 Page 123 - equation 6.6 should be

$$Pr(\geq \mathrm{N}\bar{\mathrm{R}}^2|\mathrm{H}_0) = \exp(-\mathrm{N}\bar{\mathrm{R}}^2) \tag{6.6}$$

Chapter 6 Page 135 - Footnote about Analysis of Hercules X-1 data.

While analyzing the data care has been taken to avoid accidentally "optimizing" the signal by not accounting for trials used during analysis. Both the pulsar period and orbital period ranges of the search were determined a-priori from previous observations made by the Woomera group or previously published results from other groups. The pulse cuts used were derived a-priori from Monte Carlo analysis and were not altered to increase the significance of the signal.

The search for a signal in the second harmonic was not performed to optimize the apparent signal strength due to the shape of the light curve of the signal. A search of the second harmonic is fully justified by the results of x-ray observations. These observations show that at x-ray wavelengths the light curve switches regularly between being single and double peaked. It is acknowledged that the penalty paid for searching into the second harmonic (penalty of 2) was insufficient. This factor should be changed to 8 to allow for all possible combinations of first and second harmonic analysis for the three nights observation. This increases the final chance probability from 1.34×10^{-4} to 5.36×10^{-4}.